2017

Enhancement of Antenna Array Performance Using Reconfigurable Slot-Ring Antennas and Integrated Filter/Antennas

Tianjiao Li
University of Central Florida

STARS Citation

Li, Tianjiao, "Enhancement of Antenna Array Performance Using Reconfigurable Slot-Ring Antennas and Integrated Filter/Antennas" (2017). *Electronic Theses and Dissertations, 2004-2019*. 5744.
https://stars.library.ucf.edu/etd/5744

ENHANCEMENT OF ANTENNA ARRAY PERFORMANCE USING RECONFIGURABLE SLOT-RING ANTENNAS AND INTEGRATED FILTER/ANTENNAS

by

TIANJIAO LI

B.S. University of Science and Technology of China, 2011
M.S. University of Central Florida, U.S.A, 2013

A dissertation submitted in partial fulfillment of the requirements
for the degree of Doctor of Philosophy
in the Department of Electrical and Computer Engineering
in the College of Engineering & Computer Science
at the University of Central Florida
Orlando, Florida

Spring Term
2017

Major Professor: Xun Gong

ABSTRACT

As modern communication system technology develops, the demand for devices with smaller size, higher efficiency, and more functionality has increased dramatically. In addition, highly integrated RF-front-end modules with a reduced footprint and less transition loss between cascaded devices are desirable in most advanced wireless communication systems. Antenna arrays are widely used in wireless communication systems due to their high directivity and beam steering capability. Moreover, antenna arrays are preferred in mobile communication systems for diversity reception to reduce signal fading effects. In order to meet the various requirements of rapidly developing wireless communication systems, low cost, compact, multifunctional integrated antenna arrays are in high demand.

Reconfigurable antennas that can flexibly adapt to different applications by dynamically changing their frequency and radiation properties have attracted a lot of attention. Frequency, radiation pattern, polarization, or a combination of two or more of these parameters in the reconfiguration of antennas was studied and presented in recent years. A single reconfigurable antenna is able to replace multiple traditional antennas and accomplish different tasks. Thus, the complexity of wireless communication systems can be greatly reduced with a smaller device size. On the other hand, the integration of antennas with other devices in wireless communication systems that can improve the efficiency and shrink the device size is a growing trend in antenna technology. Compact and highly efficient integrated filters and antennas were studied previously; the studies show that by seamlessly co-designing filters with patch antennas, the fractional bandwidth (FBW) of the antennas can be enhanced as compared to stand-alone antennas.

However, the advantages of both the reconfigurable antenna and integrated filter/antenna technology have not been fully applied to antenna array applications. Therefore, this dissertation explores how to maximize the antenna array performance using reconfigurable antennas and integrated filter/antennas. A continuously frequency reconfigurable slot-ring antenna/array with switches and varactors is presented first. By changing the state of the loaded switches, the reconfigurable slot-ring antenna/array is able to operate as an L-band slot-ring antenna or a 2×2 S-band slot-ring antenna array. In each frequency band, the operation frequency of the antenna/array can be continuously tuned with the loaded varactors. To further enhance the functionality of the reconfigurable slot-ring antenna array, a dual-polarized fractal-shaped reconfigurable slot-ring antenna/array is developed with a reduced number of switches and an increased FBW. Additionally, ground plane solutions are explored to achieve single-sided radiation. The benefits of filter/antenna integration are also investigated in both linearly polarized patch phased arrays and circularly polarized patch antenna arrays. Finally, a preliminary study of a tunable integrated evanescent mode filter/antenna is conducted to validate the concept of combining reconfigurable antennas and integrated filter/antennas.

Dedicated to my lovely family for all your love and support.

ACKNOWLEDGMENTS

I would like to express my appreciation to my advisor, Prof. Xun Gong for his great support, an abundant amount of advice and encouragement throughout my Ph.D. study. Also, I would like to thank the members of my dissertation committee, Prof. Parveen Wahid, Prof. Jiann-Shiun Yuan, Prof. Reza Abdolvand, and Prof. Stephen Kuebler for taking the time to review this work and provide valuable comments. I would also like to thank my friends, Dr. Haitao Cheng and Dr. Justin Luther for their advice and hands-on teaching at the beginning of my Ph.D. study. In addition, I would like to thank the funding support from the National Science Foundation Faculty Early CAREER Award under Grant 0846672 and DARPA ACT Program under Grant HR0011-14-1-0003.

I would like to thank Mr. Ricardo Lovato for his collaboration and help on the writing. I also appreciate the help from Mr. Michael E. Trampler on antenna measurement and 3-D printing. In addition, I benefitted a lot during the discussions with Dr. Yazid Yusuf, Dr. Xinhua Ren, Dr. Ya Shen and Dr. Kalyan Karnati. Moreover, I would like to thank Mr. Wei Ouyang, and Mr. Junyi Huang for their constant friendship and support.

Lastly, I want to give my special thanks to my husband, Guobin Chen, and my family members, Faren Li, Suzhen Huang, Jifei Li, Wenying Zhao and Tianyu Li for their everlasting love and continued support.

TABLE OF CONTENTS

LIST OF FIGURES xii

LIST OF TABLES xix

CHAPTER 1 INTRODUCTION 1

1.1 Motivation 1

1.1.1 Critical Roles of Antenna Arrays 2

1.1.2 Challenges of Modern Antenna Arrays 3

1.2 Overview of Reconfigurable Antenna Techniques 5

1.2.1 Mechanisms of Reconfigurable Antennas 6

1.2.2 Reconfigurable Antenna Arrays 9

1.3 Overview of Integrated Antenna Techniques 13

1.4 Dissertation Outline 15

CHAPTER 2 *L/S*-BAND RECONFIGURABLE SLOT-RING ANTENNAS/ARRAYS 16

2.1 Introduction of the Reconfigurable Slot-Ring Antenna/Array 16

2.2 *S*-Band Continuously Tunable Slot-Ring Antenna 18

2.3 *L/S*-Band Reconfigurable Slot-Ring Antenna/Array 22

2.4 Effects of the Ground Plane Size on Radiation Pattern of Reconfigurable Slot-Ring Antennas 24

2.5 Conclusion 28

CHAPTER 3 SINGLE-SIDED RADIATION OF FRACTAL-SHAPED RECONFIGURABLE SLOT-RING ANTENNA/ARRAYS 29

3.1 Introduction of the Fractal-Shaped Reconfigurable Slot-Ring Antenna/Array 29

3.1.1 Fabrication of the Fractal-Shaped Reconfigurable Slot-Ring Antenna/Array 32

3.1.2 Measurement of the Reconfigurable Slot-Ring Antenna/Array at S band 33

3.1.3 Measurement of the Reconfigurable Slot-Ring Antenna/Array at C band 37

3.2 Single-Sided Radiation of the Fractal-Shaped Reconfigurable Slot-Ring Antenna using Metal Planes 42

3.2.1 Design and Fabrication of the Metal-Backed Fractal-Shaped Reconfigurable Slot-Ring Antenna/Array 42

3.2.2 S-band Measurement of the Metal-Backed Fractal-Shaped Reconfigurable Slot-Ring Antenna/Array 44

3.2.3 C-Band Measurement of the Metal-Backed Fractal-Shaped Reconfigurable Slot-Ring Antenna/Array 48

3.2.4 Gain Improvement of the Metal-Backed Fractal-Shaped Reconfigurable Slot-Ring Antenna/Array 51

3.3 Single-Sided Radiation of the Fractal-Shaped Reconfigurable Slot-Ring Antenna/Array using Electromagnetic Band-Gap Surfaces 55

3.3.1 Design and Fabrication of the EBG-Backed Fractal-Shaped Reconfigurable Slot-Ring Antenna/Array 55

3.3.2 S-band Measurement of the EBG-backed Fractal-Shaped Reconfigurable Slot-Ring Antenna/Array ... 59

3.3.3 C-band Measurement of the EBG-Backed Fractal-Shaped Reconfigurable Slot-Ring Antenna/Array ... 63

3.4 Conclusion ... 67

CHAPTER 4 USING INTEGRATED FILTER/PATCH ANTENNAS TO ACHIEVE WIDE-SCAN-ANGLE PHASED ARRAYS WITH ENHANCED BANDWIDTH ... 68

4.1 Introduction of Patch Antenna Phased Arrays ... 68

4.2 Bandwidth Comparison between Filter/Patch and Coax-Fed Patch Antennas on Different Substrates ... 70

4.3 Fabrication and Measurement Results ... 72

4.4 Floquet Analysis ... 74

4.5 Conclusion ... 76

CHAPTER 5 INTEGRATED CIRCULARLY POLARIZED FILTER/PATCH ANTENNA ARRAYS 77

5.1 Introduction of the Integrated CP Filter/Patch Antenna/Array ... 78

5.2 Integration of High-Q Filters with Singly-Fed Circularly Polarized Patch Antennas ... 79

5.2.1 Modeling of the Probe-Fed Corner Truncated CP Patch Antenna ... 83

5.2.2 External Coupling Q_{ext1} ... 88

5.2.3 Internal Coupling between the First and Second Cavity Resonator k_{12} ... 89

5.2.4 Internal Coupling between the Second Cavity and CP Corner Truncated Patch Antenna k_{23} 90

5.2.5 CP Filter/Patch Design 91

5.2.6 Fabrication and Measurement Results 92

5.3 Sequentially Rotated 2×2 Circularly Polarized Filter/Patch Array 95

5.3.1 CP Filter/Patch Array Configuration 96

5.3.2 Feeding Network for the CP Filter/Patch Array 97

5.3.3 Fabrication and Measurement Results 98

5.4 Conclusion 101

CHAPTER 6 TUNABLE INTEGRATED FILTER/ANTENNAS 102

6.1 Introduction of the Tunable Filter Integrated with Slot Antenna 102

6.2 Design of Integrated Evanescent-Mode Filter/Antenna 104

6.3 Simulation Results of the Tunable Filter/Antenna 105

6.4 Fabrication and Measurement Results of the Tunable Filter/Antenna 106

6.5 Conclusion 110

CHAPTER 7 SUMMARY AND FUTURE WORK 111

7.1 Summary 111

7.2 Future Work 113

7.2.1 Large Fractal-Shaped Reconfigurable Slot-Ring Antenna Array 113

7.2.2 Tri-band Fractal-Shaped Reconfigurable Slot-Ring Antenna Array 113

7.2.3 Electrically Tunable Integrated Filter/Antenna 114

7.2.4 Reconfigurable Integrated Filter/Antenna Array 114

LIST OF REFERENCES 115

LIST OF FIGURES

Figure 1.1: A block diagram of a typical wireless communication system [1]. 2

Figure 1.2: A single reconfigurable pixel patch antenna with MEMS actuators [47]. 10

Figure 1.3: Reconfigurable ultra-wideband array with tunable band-rejection [52]. 11

Figure 1.4: Shared-Aperture Dual-Band Planar Array [59]... 11

Figure 1.5 Proposed pixel slot-ring antenna array covering S-, C-, X-band, respectively. 12

Figure 2.1: A schematic of a reconfigurable antenna array operating at *S*-band and *L*-band using slot-ring antennas. 18

Figure 2.2: *S*-band tunable slot-ring antenna loaded with varactors (a) simulated model; (b) fabricated one. 20

Figure 2.3: Simulated and measured S_{11} with different DC voltages. 20

Figure 2.4: Simulated and measured gain vs frequency. 21

Figure 2.5: Simulated and measured radiation patterns of the tunable slot-ring antenna at 3.17 GHz in (a) E-plane, (b) H-plane. 21

Figure 2.6: (a) Reconfigurable *L/S*-band slot-ring antenna /array. (b) *L*-band slot-ring antenna. (c) 2×2 *S*-band slot-ring antenna array. 23

Figure 2.7: Simulated return loss of (a) Continuously tunable *L*-band slot-ring antenna; (b) *S*-band 2×2 slot-ring antenna array. 24

Figure 2.8: (a) Slot-ring antenna operating at 6.27 GHz; (b): E-plane radiation patterns of the slot-ring antenna for different ground plane sizes. 26

Figure 2.9: (a) Slot-ring antenna operating at 6.27 GHz; (b): E-plane radiation patterns of the slot-ring antenna for different ground plane sizes. 27

Figure 3.1: A schematic of a fractal-shaped reconfigurable slot-ring antenna array covering *S* and *C* bands.. 31

Figure 3.2: An extended fractal-shaped reconfigurable slot-ring antenna array covering *S*, *C* and *X* bands. 31

Figure 3.3: Fabricated double-sided fractal-shaped slot-ring antenna. (a) Top view; (b) Switches under a microscope; (c) Bottom view. 32

Figure 3.4: Simulated and measured return losses. (a) H-pol. (b) V-pol. 33

Figure 3.5: Simulated and measured isolation between different ports. (a) Antenna port numbering. (b) Isolation between the horizontal and vertical polarizations at *S* band; (c) Isolation between the adjacent S-band and *C*-band feeding lines. 34

Figure 3.6: Simulated and measured gain when the antenna is in *S*-band operating mode. 35

Figure 3.7: Radiation pattern at 1.8 GHz a) E-plane; b) H-plane 36

Figure 3.8: Radiation pattern at 2.7 GHz a) E-plane; b) H-plane. 36

Figure 3.9: Radiation pattern at 3.5 GHz a) E-plane; b) H-plane. 37

Figure 3.10: Simulated and measured return loss in *C*-band operation mode. (a) H-pol. (b) V-pol. 38

Figure 3.11: Simulated and measured isolation between different ports. (a) Isolation between the horizontal and vertical polarizations at C-band. (b) Isolation between the adjacent S-band C-band feeding lines. 38

Figure 3.12: Power divider and180^0 hybrids. 39

Figure 3.13: Simulated and measured gain vs frequency in C-band operation mode. 40

Figure 3.14: Radiation pattern at (a) 4.5 GHz; (b) 6.3 GHz; (c) 8 GHz 41

Figure 3.15: (a) Finite conductor; (b) Reflection phase of the finite conductor; (c) Antenna backed with the finite conductor with a distance; (d) Total Reflection phase at *d* =15 mm.................... 43

Figure 3.16: Fabricated fractal-shaped reconfigurable slot-ring antenna backed with metal plane: (a) Top view; (b) Side view. 44

Figure 3.17: Measured and simulated return loss of (a) vertical polarization; (b) horizontal polarization; Isolation between (a) Ports 1 and 2; (b) Ports 1 and 3... 45

Figure 3.18: Measured and simulated gain vs frequency. 46

Figure 3.19: Radiation pattern at 3 GHz (a) E-plane pattern; (b) H-plane pattern. 47

Figure 3.20: Radiation pattern at (a) 1.9 GHz (b) 2.7 GHz 47

Figure 3.21: Measured and simulated return loss of (a) vertical polarization; (b) horizontal polarization; Isolation between (c) Ports 3 and 8; (d) Ports 1 and 3... 49

Figure 3.22: (a) Measurement setup of the EBG-backed fractal antenna at *C* band; (b) Measured and simulated gain vs. frequency.. 50

Figure 3.23: Radiation patterns at (a) 4.5 GHz; (b) 6.3 GHz.. 50

Figure 3.24: Reduced size of the substrate of the metal-backed antenna.................................... 52

Figure 3.25: Realized gain of the antenna with different substrate dimensions at *C*-band. 53

Figure 3.26: Realized gain of the antenna with different substrate dimensions at *S*-band. 54

Figure 3.27: Fractal-shaped reconfigurable slot-ring antenna/array on a cut-corner substrate. ... 54

Figure 3.28: (a) Mushroom-like EBG unit cell with periodic boundary conditions; (b) Reflection phase of the EBG unit cell; (c) EBG- backed antenna and (d) Total reflection phase of the EBG-backed antenna.. 56

Figure 3.29: Total reflection phase of the EBG-backed antenna at d = 9 mm 57

Figure 3.30: S_{11} of the EBG-backed reconfigurable dual-band slot-ring antenna at lower and higher bands. 58

Figure 3.31: EBG-backed fractal shaped antenna: (a) top view; (b) side view. 59

Figure 3.32: Measured and simulated return loss of (a) V-pol. and (b) H-pol. 60

Figure 3.33: Isolation between (a) H- and V-pol at *S* band (b) adjacent *S*-band *C*-band feeding lines. 60

Figure 3.34: (a) Measurement setup of the EBG-backed fractal antenna at S band; (b) Measured and simulated gain vs frequency. 61

Figure 3.35: Radiation pattern at (a) 1.9 GHz; (b) 2.7 GHz; (c) 3.5 GHz. 62

Figure 3.36: Measured and simulated return loss of (a) vertical polarization; (b) horizontal. 63

Figure 3.37: Isolation between (c) Ports 3 and 8; (d) Ports 1 and 3. 64

Figure 3.38: (a) Measurement setup of the EBG-backed fractal antenna at C band; (b) Measured and simulated gain vs. frequency. 65

Figure 3.39: Radiation pattern at (a): 4.5 GHz; (b) 6.3 GHz; (c) 8 GHz; 66

Figure 4.1: Exploded view of a 2nd-order filter/antenna comprised of one cavity resonator and one patch antenna. 70

Figure 4.2: Schematics of (a) cavity resonator with coaxial feeding and coupling via; (b) patch antenna and coupling via; (c) backside of the fabricated filter/antenna; (d) front side of the fabricated filter/antenna. (W=12.60, L=17.40, Pc=2.50, Pp=2.05, Dv=0.635, Ds=1.27, c=6.3, Wp=13, Lp=9.3, d=2.85) Dimensions are in mm. 71

Figure 4.3: Simulated and measured results of (a) 2nd-order filter/antenna; (b) patch antennas on 75- and 100-mil-thick substrates, respectively. 73

Figure 4.4: Simulated and measured radiation patterns of the 2nd-order filter/antenna and standalone patch antennas in (a) E plane and (b) H plane at the center frequency...................... 73

Figure 4.5: Active reflection coefficients vs. scan angles in E plane for four types of phased arrays. 75

Figure 4.6: Active reflection coefficients and transmission coefficients of the Floquet TM_{00} mode in E plane for the filter/patch phased array at different scan angles. 76

Figure 5.1: Exploded view of a third-order filter/antenna comprised of two cavities and a single-fed circularly polarized patch antenna. 81

Figure 5.2: Schematics of the CP filter/patch. Top view of (a) First cavity resonator of the CP filter/patch including a SMA connector and a coupling slot; (b) Second cavity resonator of the CP filter/patch with a coupling via and slot and (c) corner-truncated CP patch with coupling vias. (d) Side view of the stacked CP filter/patch antenna. (W_1 = 12.80, L_1 = 16.50, P_s = 3.90, W_{slot} = 0.50, L_{slot} = 6.20, X_s = 0.75, W_2 = 12.80, L_2 = 15.85, P_c = 2.95, L_p = 9.50, a = 1.40, P_p = 2.65, h_1 = 1.58, h_2 = 0.79, all in millimeters. 81

Figure 5.3: Equivalent circuit model of (a) reference filter, (b) integrated filter with LP patch antenna, (c) integrated filter with CP patch antenna 82

Figure 5.4: Corner truncated square patch with a probe feed. (b) Circuit model of the corner truncated CP patch. 84

Figure 5.5: Waveguide coupled corner truncated square patch with coupling via located along (a) one of the diagonal direction to excite only mode #1; (b) the other one of the diagonal direction to excite only mode #2; (c) y-axis to excite both orthogonal modes. 85

Figure 5.6: Input impedance extracted from the equivalent circuit mode compared with the simulated input impedance. 88

Figure 5.7: External coupling to the first resonator changing with P_s. 89

Figure 5.8: Internal coupling between the first and second cavity resonator versus coupling slot position X_s and slot length L_{slot} 90

Figure 5.9: Simulated S_{11} and S_{21} of the reference filter using equivalent circuit model compared to simulated S_{11} and total realized gain of the CP filter/patch antenna shown in Fig. 1. 92

Figure 5.10: (a) Fabricated CP filter/patch antenna. (b) Simulated and measured S_{11} responses. (c) Simulated and measured gain and axial ratio (d) Wide band response of the filter/antenna. 93

Figure 5.11: Simulated and measured ration patterns. 95

Figure 5.12: Exploded view of the 2×2 sequentially rotated CP filter/patch antenna array. 96

Figure 5.13: Feeding network of the 2×2 sequentially rotated CP filter/patch antenna array. 97

Figure 5.14: (a) Fabricated 2×2 CP filter/patch antenna array. (b) Simulated and measured S_{11} responses of each CP filter/patch antenna element. (c) Simulated and measured gain and axial ratio of the CP filter/patch antenna array (d) Wide band response of the CP filter/antenna array. 98

Figure 5.15: Simulated and measured radiation patterns in both XOZ and YOZ plane. 101

Figure 6.1: (a) Two-pole reference evanescent-mode filter (b) evanescent-mode filter integrated with a slot antenna. 103

Figure 6.2: Dimensions of the evanescent-mode filter/antenna H= 5, H_c = 7.5, h_c = 4.7, d_c = 0.87, D_c = 2.73, P_c = 1.8, P_d = 3.18, Gap_1 = 1, Gap_2 = 1.15, L = 14, W_c= 4.6, L_a =11.92, X_a = 9, and W_a = 3 (all dimensions are in mm). 104

Figure 6.3: Simulated results of the evanescent-mode filter and filter/antenna in (a) time domain and (b) frequency domain. 105

Figure 6.4: Simulated results of the tunable filter/antenna. 106

Figure 6.5: Updated 3-D model of the integrated filter/antenna. 107

Figure 6.6: Fabricated reference filter and filter/antenna. 107

Figure 6.7: Frequency-domain measurement of (a) reference filter and (b) integrated filter/antenna.
.... 108

Figure 6.8: Radiation pattern of the integrated filter/antenna at 6.8 GHz. 108

Figure 6.9: Measured tuning range of the evanescent-mode filter/antenna. 109

LIST OF TABLES

Table 1.1: Comparison between different reconfigurable mechanisms... 8

Table 4.1: Comparison of FBW and Gain for Filter/Antenna and Patch Antennas 74

Table 5.1: S_{11}-AR Bandwidth Comparison Among Different Techniques 100

CHAPTER 1 INTRODUCTION

This chapter begins by introducing the challenges of antenna arrays in meeting the requirements of modern wireless communication systems. An overview of two promising techniques that can improve different aspects of antenna array performance is then presented. Finally, an outline of this dissertation is listed.

1.1 Motivation

In the 20th century, the rapid development of wireless communications has changed the way people connect with each other. Without using cables and wires, wireless technologies allow information to be transferred from one point to another through free space; this makes it possible for people to receive information from anywhere at any time. Exponential growth of the wireless communication market has been seen over the last few decades and this growth is expected to continue. Wireless applications such as cellular phones, WiFi, Bluetooth, satellite communications, and wireless local area networks (WLAN) have become part of everyday life. The evolution of wireless technologies has also increased in pace: to take mobile phones as an example, wireless communication systems have quickly evolved from 1G, 2G, 3G to 4G/LTE and very soon we will make the transition to 5G. As more wireless technologies emerge, there is increased demand on the performance of wireless communication systems that require faster data rates, higher capacity and mobility, multi-band operation, and lower power consumption.

1.1.1 Critical Roles of Antenna Arrays

Fig. 1.1 shows the block diagram of a typical wireless communication system [1]. A complete wireless communication system consists of a transmitter, RF propagation channel, and a receiver. On the transmitter side, input signals are first coded and modulated onto intermediate frequency (IF) signal. The IF signal is then converted to an RF signal by heterodyning with a local oscillator signal. A power amplifier is used to increase the power of the converted RF signal. After that, the RF signal goes through a passband filter to suppress any undesired frequencies such as intermodulation products and harmonics. Finally, antennas arrays are used to radiate the passband RF signal to free space. The transmitted RF signal attenuates through the propagation channel due to the free space path loss and fading effects from the surroundings. On the receiver side, the attenuated RF signal is sensed by an antenna array and then filtered and amplified by an RF filter and low-noise-amplifier (LNA). A mixer with an oscillator are used to convert the RF signal down to an IF signal. After filtering and amplifying, the IF signal is demodulated and decoded to extract the original input information.

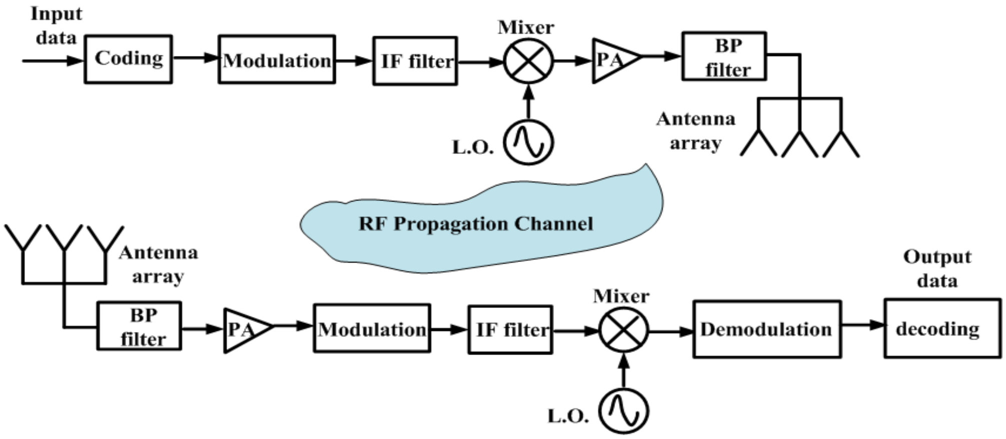

Figure 1.1: A block diagram of a typical wireless communication system [1].

From the above description of a wireless communication system, it can be seen that antenna arrays play a very important role in both the transmitting and receiving sides. Without antennas/arrays, RF signals cannot be transferred from one point to another in free space. On the receiver side, the radiating performance of the antenna array is especially critical for sensing the correct RF signals due to a relatively low power level. For long-distance communications such as satellite and radar communications, the transmitted signal suffers from severe free space loss and as a result, highly directive antenna arrays are required for maximizing the received signal power and achieving a higher signal to noise ratio (SNR) [2]. Moreover, in other applications such as target tracking and object detection, the narrow beam of the antenna array needs to be electrically steered to different directions [3]. In this case, phased array antennas with beam steering capabilities are preferred. Therefore, the design specifications of antenna arrays are customized based on the requirements of various applications.

1.1.2 Challenges of Modern Antenna Arrays

To meet growing market demands for high-speed data rates, lower power consumption, smaller size, lower cost, and a light –weight device, modern wireless communication systems are developing rapidly which require a corresponding evolution of antenna arrays to keep pace. Several key challenges in the design of modern antenna arrays are listed below:

Physical Size: Antenna arrays are a set of antenna elements placed with a certain distance and simultaneously excited with specific amplitudes and phases to form a larger radiating area [4]. The physical size of antenna arrays is related to the geometry of the individual antenna elements, the distance between each element, and the feeding network. Relatively large separating spacing between antenna elements is necessary to reduce mutual coupling effects [5]. In addition, feeding networks of antenna arrays, particularly phased antenna arrays which require phase shifters, are typically bulky. Thus, to fit an antenna array in a wireless communication system, a large volume is required.

Cost: The fabrication and assembly of antenna arrays are prohibitively expensive and time-consuming due to the complexity. Each antenna array element needs to be precisely controlled in order to get desired radiating performance. The antenna array developed for satellite Earth Observing-1(EO-1) costs about US$ 4 million while the Atacama Large Millimeter/Submillimeter Array (ALMA) costs as much as US$ 1.6 billion [6-7]. In addition, since those antenna arrays were designed to meet fixed specifications for their respective purposes, they cannot be adapted to other applications.

Multi-functionality: In traditional wireless communication systems, each antenna array is designed for a single task. However, as the demand in RF functionality increases, the number of antenna arrays has increased dramatically. In cell phones, different antennas are implanted in order to meet the requirements of various applications such as GPS, Bluetooth, and Wifi. The increased number of antennas/arrays not only results in a bulky size but also a more complicated system. In addition, the interference between different antenna arrays may degrade the radiating performance. To address this problem, antenna arrays which can perform multiple functions simultaneously co-located with other antennas are desired in next generation communication systems**.**

Power-consumption: Wireless communication systems are typically packaged and installed inside electronic devices where the batteries are not easy to access [8]. Moreover, in mobile phone systems, approximately 70% of power is consumed by wireless devices [9]. Furthermore, if the consumed power cannot be radiated efficiently, it will become heat and hence degrade the overall performance of the system and cooling systems are expensive and bulky. Therefore, high-efficient wireless communication systems are necessary to increase the operating time of electronic devices and avoid the inconvenience of replacing batteries.

Two promising antenna topologies that can provide solutions for the aforementioned challenges are reconfigurable antennas and integrated antennas and have attracted a lot of attention in recent years. Reconfigurable antennas are flexible in frequency, radiation pattern, polarization, geometry, and can be easily adapted to different applications. Thus, a single reconfigurable antenna is able to replace multiple traditional antennas and accomplish different tasks in a wireless system. In this way, the complexity of the wireless communication system will be greatly reduced while also having a smaller size. On the other hand, the integration of antennas with other devices in wireless communication systems improves the efficiency and shrinks the size. Compact and highly efficient integrated filters and antennas were studied previously. In section 1.2 and 1.3, an overview of both reconfigurable antennas and integrated antennas will be presented, respectively.

1.2 Overview of Reconfigurable Antenna Techniques

Reconfigurable antennas/arrays are achieved by dramatically changing the distribution of surface currents on the antenna’s aperture, the radiation edges, or the physical operating geometry. Reconfigurable antennas/arrays are described by different performance metrics; frequency, radiation characteristics, polarization, or a combination of two or more of these parameters in reconfigurable of antennas was studied and presented [10-45]. In order to realize those reconfigurations, various mechanisms including integrating electronic switches, varactors, micro-electro-mechanical systems (MEMS), tunable materials, and mechanically modifying the structures were investigated.

1.2.1 Mechanisms of Reconfigurable Antennas

PIN diode switches or MEMS switches can be inserted in the radiation apertures of antennas [10-25]. By manipulating the ON/OFF mechanism, the implanted switches act either as a “SHORT” to connect a conducting patch or an “OPEN” to break a conducting patch. Thus, currents on the aperture of antennas can be redistributed and different RF parameters of the antenna are altered. A frequency reconfigurable microstrip slot antenna (MSA) was presented in [10]. With five PIN diode switches placed on the slot, the operating frequency of the MSA was able to be switched between six bands. Moreover, by implanting 18 switches across a circular slot-ring on a microstrip patch antenna, both the frequency and polarization can be changed as shown in [11]. Tri-band and quad-band reconfigurable antennas implanted with PIN diode switches were reported in [12] and [13], respectively. A frequency and pattern reconfigurable inverted-F antenna was presented in [14].

MEMS switches with lower loss, higher linearity, and smaller size were also used in reconfigurable antennas [15-25]. An overview of RF MEMS technologies was reported in [15]. [16]-[20] presented different types of frequency reconfigurable antennas using MEMS switches. Moreover, both frequency and radiation pattern reconfigurable antennas were presented in [21]-[23]. Polarization reconfigurable antennas integrated with MEMS switches were also studied [24-25]. In [25], a square coplanar patch antenna was polarized to right-handed circular polarization, lefthanded circular polarization, or linear polarization based on the status of the integrated RF MEMS switches.

Switches typically provide discrete frequency reconfigurability while varactors can offer a continuous frequency tuning range. [26] reported a slot-ring antenna which can continuously tune from 0.95 to 1.8 GHz with varactors loaded in the slot-ring. A dual band tunable slot antenna using varactors was presented in [27]. Microstrip patch antennas with frequency tunability were reported in [28-30]. In addition, a varactor-tuned patch antenna with frequency and polarization agility was studied in [31]. The radiation pattern can also be dynamically changed without phase shifters but using varactors [32-35]. Parasitic array antennas with beam steering capability was showed in [33-34]. By placing varactors between the driven patch antenna and two parasitic antenna elements, the coupling between the three antenna elements can be tuned by the varactors. Using these varactors, the main beam of the radiation pattern can be swept from -15^o to 15^o. Moreover, by adding varactors on the radiation edges of the patch antennas, a frequency tunable Electrically-Steerable Parasitic Array Radiator (ESPAR) was achieved [35].

Ferrite materials and liquid crystals are able to change the dielectric properties when an electric or magnetic field is applied. The frequency and radiation performance characteristics of antennas designed with ferrite materials can be altered electrically [36-39]. A liquid crystal tunable microstrip patch antenna was reported in [40] while a frequency-tunable patch array using highly anisotropic liquid crystal was presented in [41]. Tunable antennas based on microfuilds were also reported [42].

Beyond the aforementioned electrical mechanisms, mechanically changing the performance of antennas provides the advantages of lower power consumption and smaller loading effects is another way to realize reconfigurable antennas [43-45]. A square ring antenna loaded with a bendable parasitic plate was developed in [43]. By actuating the SMA spring actuators, the parasitic plate is bent to different directions and the radiation patterns of the square ring antenna are reconfigured. In [45], a smartly mechanically actuated microstrip antenna with reconfigurability in frequency, bandwidth, and antenna gain was presented.

The various mechanisms to achieve antenna reconfigurability have been explored. Each mechanism has their own advantages and shortages. To summarize, a comparison between the above tuning mechanisms is listed in Table 1.1 [46].

Table 1.1: Comparison between different reconfigurable mechanisms.

Reconfigurable Mechanisms	Advantages	Disadvantages
Switches	Small loading effects Low loss Fast tuning speed Commercial available	Discrete tuning
Varactors	Continuously tuning Fast tuning speed Commercial available	Relatively large loading effect Non-linear behavior High loss
Tunable Materials	Continuously tuning Simple bias network Good reliability	High voltage control High loss Slow tuning speed
Mechanical actuators	Low power consumption Good linearly	Discrete tuning Bulky size Slow tuning speed

1.2.2 Reconfigurable Antenna Arrays

A lot of research effort has been done in applying the above reconfiguration mechanisms to antenna array applications. Several approaches for achieving antenna arrays with multiple reconfigurability to include frequency, polarization, and radiation pattern are presented in this section.

Reconfigurable pixel patch antenna arrays with the ability to tune frequency, polarization and radiation pattern were studied by many researchers [47-49]. Fig. 1.2 shows a single reconfigurable pixel patch antenna [47]. MEMS actuators are used to connect the adjacent patches and by turning the MEMS actuators up/down, the adjacent pixels are connected/disconnected. In this way, the pixel patch can be formed into different geometries. When the size of the antenna changes, frequency reconfigurability is achieved. By connecting the pixels in only the X- or Y- directions, horizontal or vertical polarization is obtained, respectively. The concept of the reconfigurable pixel patch antenna array was presented in [47] while the initial simulation studies were shown in [48-49]. The drawback associated with this technique is the need of numerous switches. The bias network to control a large number of switches will be extremely complicated. In addition, when applying this reconfigurable pixel patch antenna to applications, other issues can arise such as mutual couplings between each element and grating lobes.

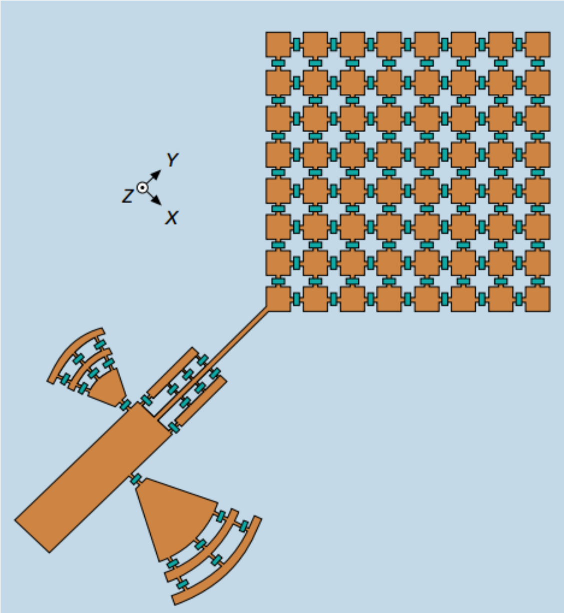

Figure 1.2: A single reconfigurable pixel patch antenna with MEMS actuators [47].

Alternatively, reconfigurable antenna arrays can be achieved by using an ultra-wideband antenna array with tunable band rejections [50-52]. The tunable band-rejection can be realized by either using tunable bandstop filters [50] or tunable lumped element baluns [51]. Fig. 1.3 shows a tight-coupled dipole array (TCDA) with reconfigurable band rejection system [52]. The tight-coupled dipole array ultra-wideband antenna array operates from 0.6 to 4 GHz with a VSWR smaller than 3.9. The frequency reconfigurability is achieved by using balun feeds loaded with tunable capacitors in the short stub. In addition, when placing two sets of TCDAs perpendicularly to each other, dual-polarization is obtained [53]. This reconfigurable antenna array approach gets rid of grating lobe issues due to the tight-coupled topology but it suffers from high noise and expensive T/R modules if used in wireless communication systems.

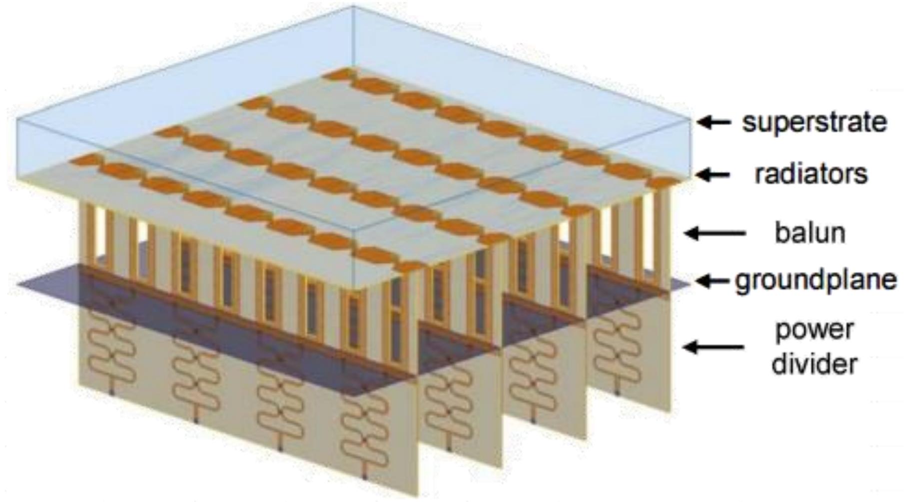

Figure 1.3: Reconfigurable ultra-wideband array with tunable band-rejection [52].

Using a shared aperture is another option to get multi-band and multi-task antenna arrays [54-59]. For a shared aperture antenna array, sub-arrays with different frequencies and polarizations are placed in one physical aperture. [54] presented a tri-band phased array covering C-, X- and Ku-band while a dual band shared aperture folded dipole antenna array was shown in [59]. The array configuration is displayed in Fig 1.4. However, in order to fit all the sub-arrays in one aperture, there are limitations in operation frequency and element spacing.

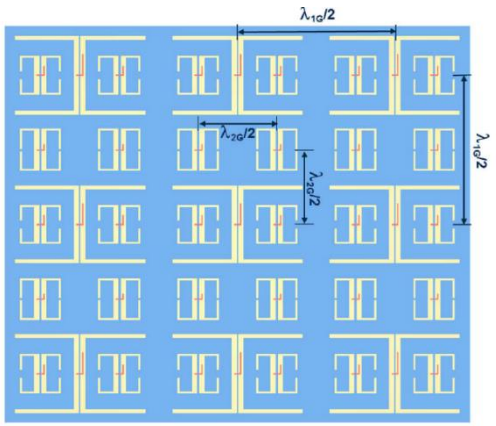

Figure 1.4: Shared-Aperture Dual-Band Planar Array [59].

Currently existing reconfigurable antenna arrays have limitations in different aspects. In order to obtain a new reconfigurable antenna array with flexibility in frequency, polarization, and radiation pattern at the same time we propose a pixel slot-ring antenna array in this dissertation as shown in Fig. 1.5. The antenna array consists of three sets of slot-ring antennas with different sizes which can cover three frequency bands. Each band has two perpendicular microstrip lines on the backside as feeding lines that allow the polarization of the antenna array to be easily changed. The frequency reconfigurability is achieved by varactors and switches located at different positions in the slots. By applying phase differences to the array elements, the main beam can be steered to different directions. The design details of the proposed reconfigurable slot-ring antenna array will be presented in Chapter 2 and Chapter 3.

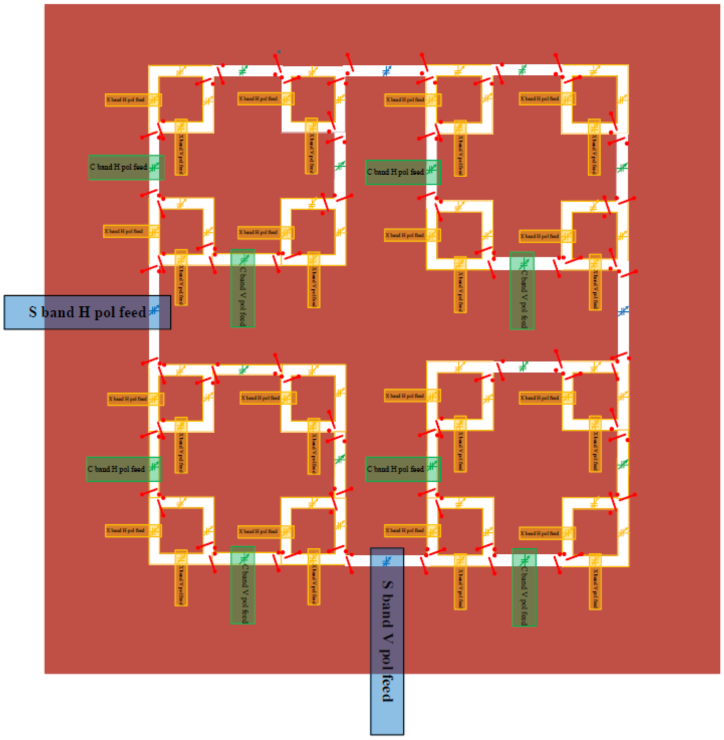

Figure 1.5 Proposed pixel slot-ring antenna array covering S-, C-, X-band, respectively.

1.3 Overview of Integrated Antenna Techniques

By replacing the traditional antenna arrays with reconfigurable antenna arrays, the number of antenna arrays needed in wireless communication systems can be reduced while simultaneously reducing complexity. On the other hand, in order to improve the efficiency and shrink the size, integration between antennas and other cascaded devices in wireless communication systems has been studied [60-77]. In [60], a dipole antenna co-designed with a low noise amplifier (LNA) for 60 GHz wireless communication systems was presented. By integrating the antenna with LNA, maximum power transfer between the two devices was achieved without additional matching components. The integration between power amplifiers (PA) and patch antennas was reported in [61]. Patch antennas were designed as both load and radiator.

Band pass filters always follow antennas in both the transmitting and receiving chain to reject out-of-band signals and suppress harmonics. Therefore, the integration between filters and antennas has attracted a lot of attention. Microstrip resonator filters co-designed with patch antennas were presented in [62-66]. In [62], a coplanar waveguide (CPW)-fed patch antenna was connected with two open-circuited half-wavelength microstrip resonators by metallic vias; the CPW-fed patch antenna was used as the last pole of the filter. As a result, a 3rd-order filtering response was achieved in [62]. An inverted L antenna integrated with a coupled line microstrip filter was reported in [67]. In addition, circularly polarized (CP) microstrip filtering antennas were demonstrated in [68-69]. However, since the microstrip resonator filters typically have low Q-factors, the applications of integrated antennas with microstrip filters are limited.

In order to obtain a lower insertion loss, high-Q substrate integrated waveguide (SIW) filter/antennas were studied in [70-77]. Based on the fractional bandwidth (FBW) of the antenna, there are two approaches to co-design filters and antennas together. If the antenna's bandwidth is wider than the filter's bandwidth, as is the case with slot antennas, [74-76] the antenna can be treated as an equivalent load to the filter. By directly coupling the antenna to the filter, the standard 50-ohm ports connecting the filter and antenna are eliminated; both the size and the overall efficiency are improved by this integration and efficiencies as high as 100% were achieved in [74] using a slot antenna. To further reduce the footprint, vertically integrated filters with slot antennas were presented in [75-76]. If the antenna's bandwidth is narrower than the filter's bandwidth, such as with patch antennas, the antenna can be designed as an additional resonator of the filter [77]. This results in a higher order filtering response that can be achieved by a reduced number of resonators when using the antenna as a contributing resonance. A third-order filtering response was achieved by two cavities resonators and one patch antenna in [77]. In addition, since the cavity resonators behave as an optimized broadband feeding network for the patch antenna, the integrated filter/patch has an enhanced FBW compared with a standalone probe-fed patch antenna.

Note that the aforementioned high-Q filters are mainly integrated with single antennas, the benefits of the integration technique in antenna array applications have not bee studied. Hence, in this dissertation, an integrated filter/patch antenna used in a phased antenna array will be investigated. Moreover, the previously studied integrated filter/antennas are linearly polarized (LP) but in many applications, CP antennas are preferred over LP antennas due to their reduction of multipath effects. Therefore, a high-Q SIW filter integrated with a CP patch antenna as well as a 2×2 integrated CP filter/patch antenna array will be explored in this dissertation.

1.4 Dissertation Outline

This dissertation explores the advantages of applying both reconfigurable antenna and integrated filter/antenna techniques to antenna array applications. Seven sections will be presented here. Chapter 1 introduces the state-of-art research in both reconfigurable antennas and integrated filters and it also talks about the motivation and challenges of developing modern antenna arrays. Chapter 2 presents an *L/S*-band reconfigurable slot-ring antenna/array loaded with varactors and switches. Chapter 3 shows a dual-polarized fractal-shaped reconfigurable slot-ring antenna/array which is developed with a reduced number of switches and an increased FBW. Single-sided radiation solutions of the fractal slot-ring antenna/array are also discussed in this Chapter. An approach to achieve a wide scan angle and enhanced FBW phased antenna array using integrated filter/patch antennas is demonstrated in Chapter 4. In Chapter 5, the design details of a 2×2 CP filter/patch antenna array with enhanced S_{11}-axial ratio bandwidth is presented. Chapter 6 talks about our preliminary study of a tunable integrated evanescent mode filter/antenna to validate the concept of combining reconfigurable antennas and integrated filter/antennas. Finally, a summary is presented in Chapter 7 as well as some future work based on this research.

CHAPTER 2 *L/S*-BAND RECONFIGURABLE SLOT-RING ANTENNAS/ARRAYS

This chapter begins by presenting a continuously-tunable single-polarized slot-ring antenna operating at S band. The frequency tuning is achieved by loading the slot-ring antenna with varactors and by properly designing the feeding network and biasing circuits, the slot-ring antenna is able to cover a frequency range of 2-4 GHz. A prototype antenna was fabricated and measured and the measurement results are presented. The measured return loss is better than 9 dB from 2.66 to 4.09 GHz and the antenna gain and radiation pattern are very close to simulation results. This tunable slot-ring antenna is extended for a reconfigurable antenna array to cover both L band and S band by strategically placing switches and varactors inside the slots of the antenna; this novel antenna array is able to change its frequency, polarization and radiation pattern. The effect of the ground plane size on the reconfigurable slot-ring antenna array is also investigated.

2.1 Introduction of the Reconfigurable Slot-Ring Antenna/Array

In many advanced communication systems, antenna arrays are highly desirable due to their high directivity and beam steering capability. However, the development of antenna arrays is relatively time consuming and expensive. In addition, antenna arrays are often designed for certain applications which means that the technology developed for one project cannot be adopted for another one. Therefore, reconfigurable antenna arrays which have the capability of electrically changing their RF communication parameters such as center frequency, polarization and radiation pattern have attracted significant attention in recent years. Much of the previous work in reconfigurable antennas has demonstrated the tuning of one or two RF parameters for a single antenna [78]; there is little work on reconfigurable antenna arrays with the degree of freedom provided by being able to tune the previously listed RF parameters.

In this work, a novel reconfigurable antenna array structure is presented and is tunable in frequency, polarization, and the radiation pattern. As shown in Fig. 2.1, a tunable L-band slot-ring antenna is loaded with four smaller S-band slot-ring antennas. The PIN diodes inside the slot of the antenna are used to switch between the operational frequency bands. By turning switches *A* ON (OFF) and switches *B* OFF (ON), the antenna can work as a 2×2 *S*-band antenna array (a single *L*-band antenna). The varactors are able to continuously tune the center frequency of the slot-ring antenna within each respective frequency band. By applying different phases for each antenna element, the radiation pattern of the 2×2 *S*-band antenna array can be reconfigured. The same structure can be further extended to achieve beam-steering at *L* band. It is noted that the antenna array shown in Fig. 2.1 in addition also has a dual polarization capability which can be fed through the microstrip lines in either the vertical or horizontal direction. In [26], a dual-polarized slot-ring antenna was demonstrated with frequency reconfigurability at *L* band. In this paper, we extended the operation frequency to *S* band with continuous frequency tuning and single polarization. In addition, we plan to develop the aforementioned reconfigurable antenna array based on the antenna presented here.

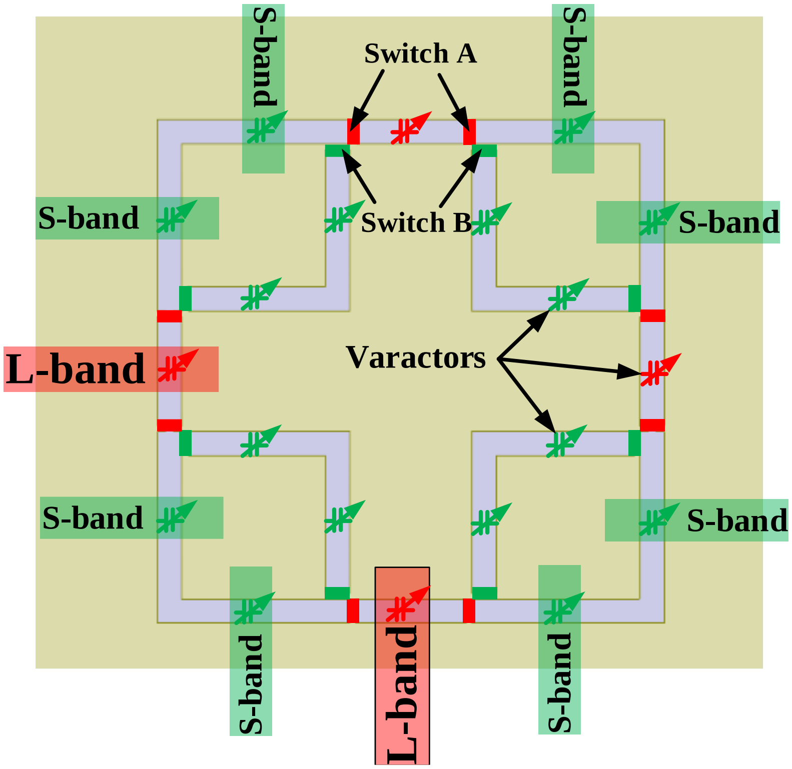

Figure 2.1: A schematic of a reconfigurable antenna array operating at *S*-band and *L*-band using slot-ring antennas.

2.2 *S*-Band Continuously Tunable Slot-Ring Antenna

Fig. 2.2 shows the structure of the *S*-band tunable slot-ring antenna. The slot-ring antenna is printed on a 60×60×0.787mm3 RT/Duroid 5880 (ε_r = 2.2; tanδ = 0.0009) substrate and loaded with two varactors (M/A-Com MA46580, 0.14–2.1 pF from 0–20 V) [79]. The antenna is fed by an open-ended microstrip line. A DC bias-T is used to supply the DC voltage to the varactors through a 100-kΩ resistor and a via hole [26]. By changing the capacitance of the varactors from 0.2 to 1.6

pF, the center frequency of the slot-ring antenna can be continuously tuned from 1.97 to 3.97 GHz with a return loss better than 10 dB in ANSYS High Frequency Structure Simulator (HFSS).

The return losses of the S-band continuously-tunable slot-ring antenna are measured using an Agilent N5230A PNA. When applying a DC voltage from 1 to 12 V, the measured center frequency ranges from 1.97 to 4.09 GHz as shown in Fig. 3. The return loss is better than 9 dB between 2.66 and 4.09 GHz and it is noted that the bandwidth is wider when the center frequency is higher, corresponding to a smaller varactor capacitance. The radiation patterns and gain of the antenna are measured in an anechoic chamber. Both the measured and simulated gain are plotted versus frequency in Fig. 4. The measurement results match the simulations very well above 2.7 GHz. The discrepancy is larger below 2.7 GHz mainly due to impedance mismatches as shown in Fig. 3. In addition, the losses from the varactors may not be accurately modeled in HFSS simulations. Fig. 5(a) and (b) show the measured and simulated radiation patterns at 3.17 GHz. The measured co-pol patterns in both E- and H-planes agree well with simulated patterns. The simulated cross-pol levels in both E-plane and H-plane are below -30 dB (they are not shown in Fig. 4 due to the scale). The measured cross-pol levels are higher which is most likely due to the scattering from the RF cables and mounting structures. The measured radiation patterns maintain similar shapes throughout the entire frequency band.

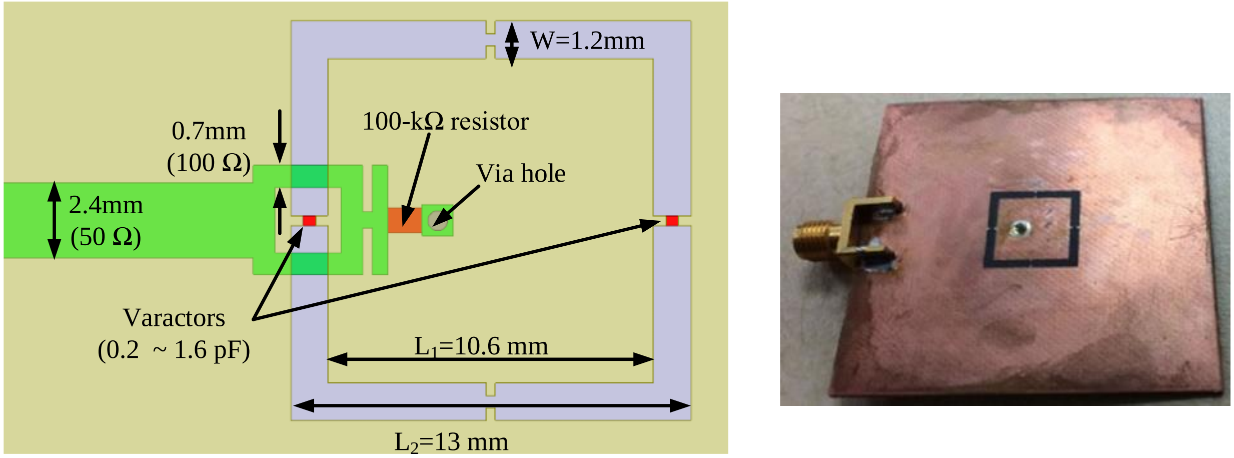

(a) (b)

Figure 2.2: *S*-band tunable slot-ring antenna loaded with varactors (a) simulated model; (b) fabricated one.

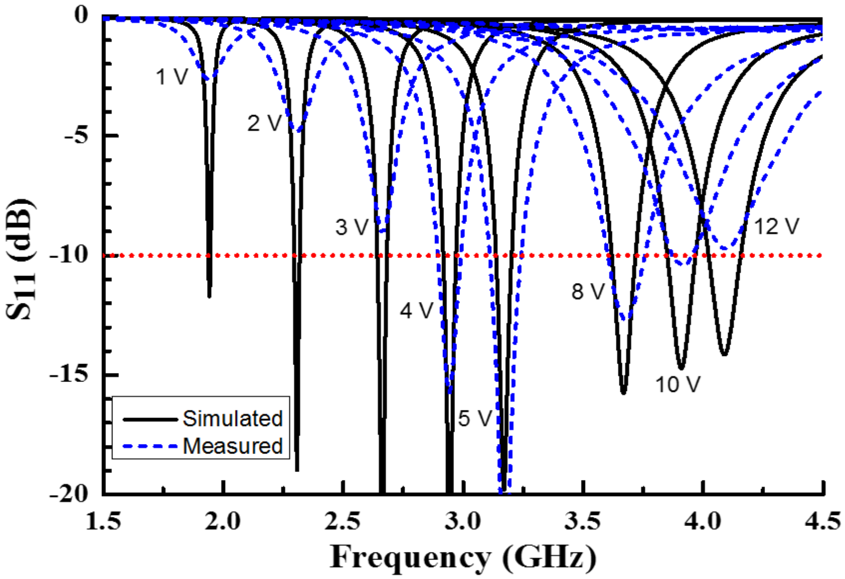

Figure 2.3: Simulated and measured S_{11} with different DC voltages.

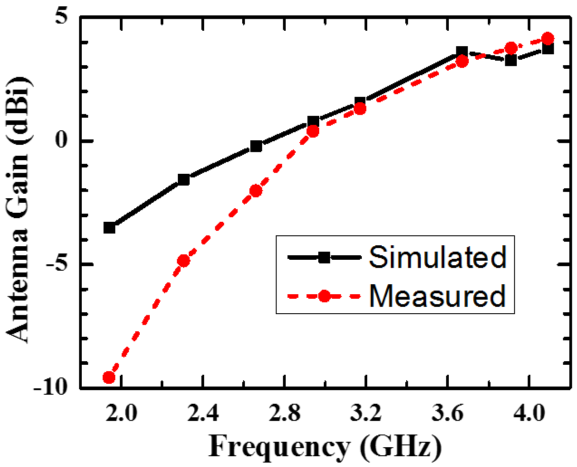

Figure 2.4: Simulated and measured gain vs frequency.

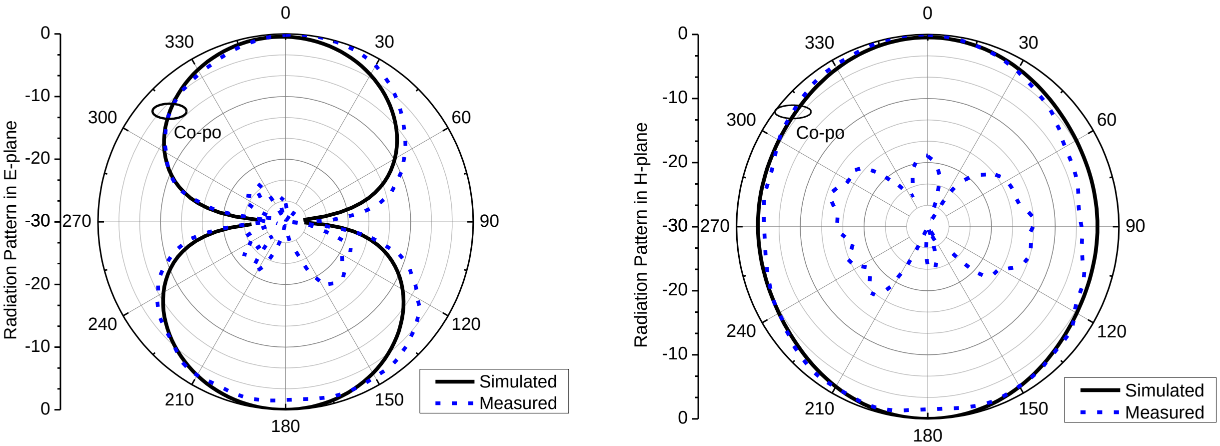

(a)

(b)

Figure 2.5: Simulated and measured radiation patterns of the tunable slot-ring antenna at 3.17 GHz in (a) E-plane, (b) H-plane.

2.3 *L/S*-Band Reconfigurable Slot-Ring Antenna/Array

An *L/S*-band reconfigurable antenna/array using the aforementioned tunable *S*-band slot-ring antenna as the elements of the antenna array is simulated in HFSS. 16 switches and 10 varactors are strategically placed at different locations of the slot-ring to enable band selection and continuous frequency tuning as shown in Fig. 2.6. The switches are controlled by two sets of DC voltages: switches *A* (red color) and switches *B* (green color). When switches *A* are "OFF" and switches *B* are "ON", this particular switching state allows only the larger square slot-ring in the inset of Figure 2.6 (b) to function as an *L*-band antenna. The varactors outlined in red can tune the center frequency in an octave bandwidth covering the *L*-band. If switches *A* are "ON" and switches *B* are "OFF", the larger square slot-ring is separated to form for small slot-rings. Thus, a 2×2 *S*-band slot-ring antenna array is realized. The varactors in blue can tune the center frequency in an octave bandwidth covering *S*-band. Microstrip lines on the backside of the antenna substrate are used to feed the signals into the antenna. Moreover, since the structure is symmetric, dual-polarization can be achieved by using two set of microstrip feeding lines perpendicular to each other.

Fig. 2.7 shows the simulated results of the *L/S* reconfigurable antenna array. The switches are modeled by lumped elements [80]; when the switch is in an "ON" state, it is modeled by an inductor series with a resistor. An inductor in series with a parallel resistor and capacitor is used to represent the switch when it is in an "OFF" state. The lumped elements values are extracted from the manufacturer data sheet [81] and the loaded varactors are modeled by capacitors with different capacitances. When the switches are activated in *L*-band operation mode and the values of the red varactors are tuned from 0.14 to 2 pF, the center frequency of the slot-ring antenna at *L* band moves from 1.6 GHz to 1.0 GHz as show in Fig. 2.7 (a). In the *S*-band slot-ring antenna array operation mode, if the varactors’ capacitance is tuned from 0.2 to 1.4 pF, the center frequency of the slot-ring antenna array is tuned from 4 to 2 GHz, covering the whole *S*-band as shown in Fig. 2.7 (b). To conclude, the presented reconfigurable slot-ring antenna/array can adapt to different configurations of both frequency and bandwidth.

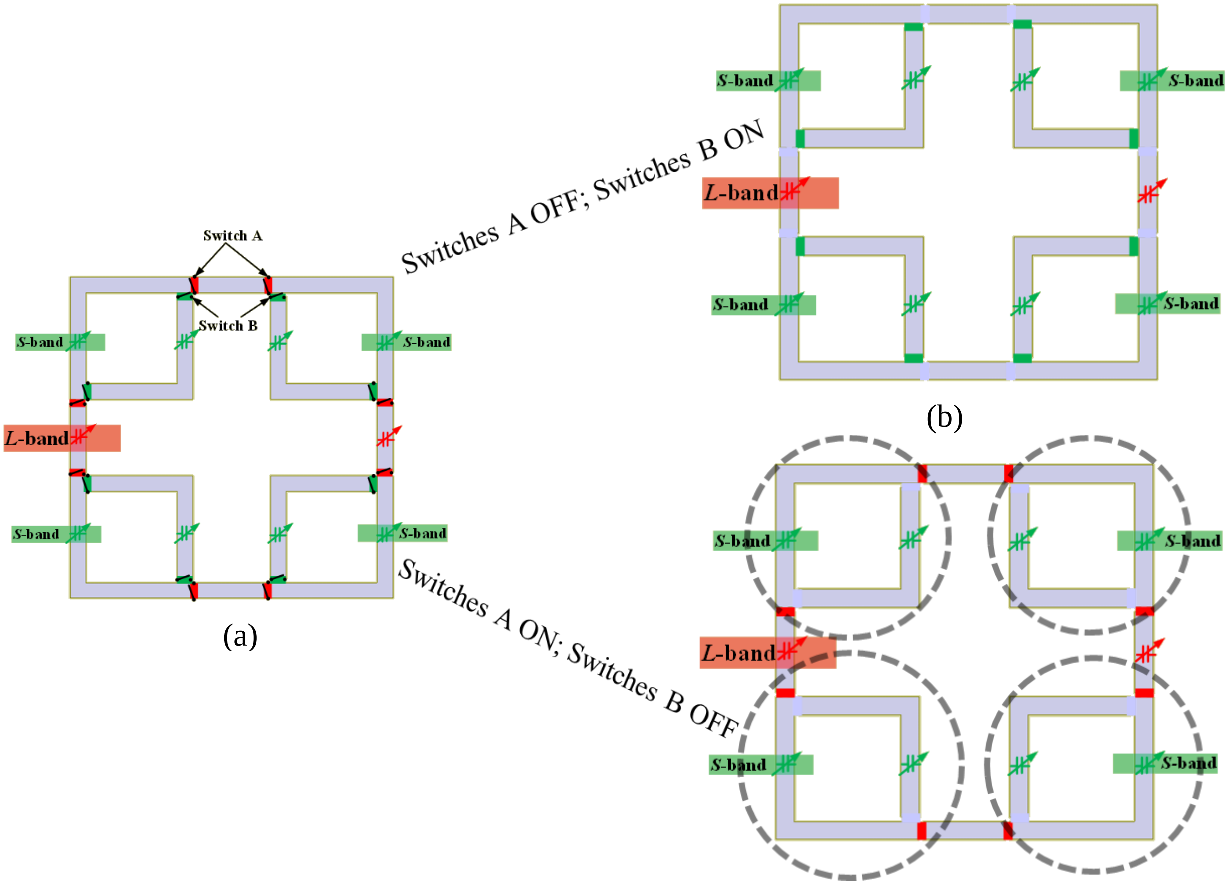

(a)

(b)

(c)

Figure 2.6: (a) Reconfigurable *L/S*-band slot-ring antenna /array. (b) *L*-band slot-ring antenna. (c) 2×2 *S*-band slot-ring antenna array.

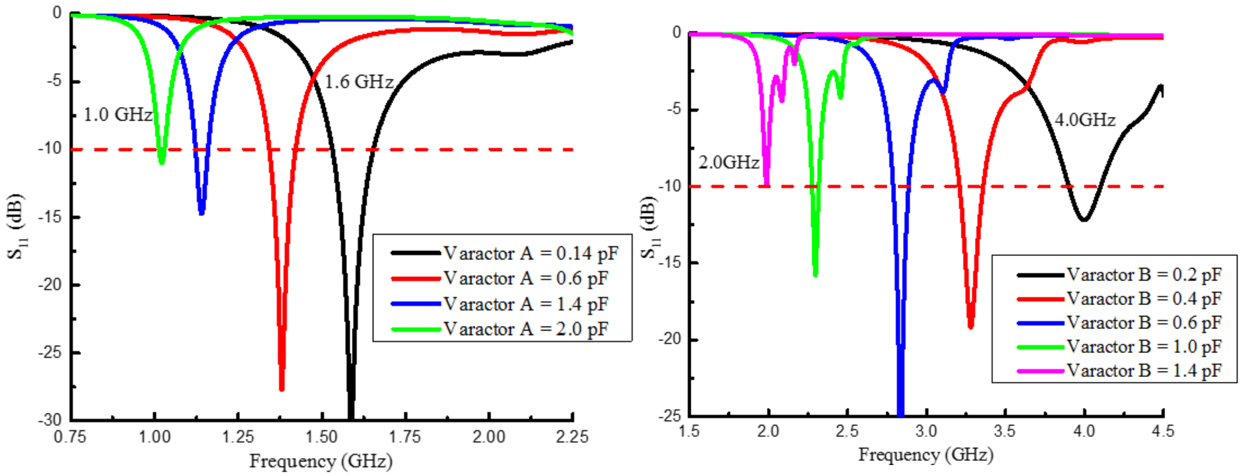

(a)

(b)

Figure 2.7: Simulated return loss of (a) Continuously tunable *L*-band slot-ring antenna; (b) *S*-band 2×2 slot-ring antenna array.

2.4 Effects of the Ground Plane Size on Radiation Pattern of Reconfigurable Slot-Ring Antennas

The effects of the ground plane size on the reconfigurable slot-ring antenna are explored in this section to predict the radiation performance of a large reconfigurable slot-ring antenna array. Both the physical structure and the electric-field distribution of different frequency bands (L, S, and C) are similar for the reconfigurable slot-ring antenna. As a result, only the relationship between the ground plane size and the radiation pattern at the C band is investigated and presented. The radiation pattern of a 5×5 slot-ring antenna array is also shown in this section.

Fig. 2.8(a) shows the structure of the slot-ring antenna operating at the upper frequency band of the reconfigurable slot-ring antenna. The slot-ring antenna is designed on a RT/Duroid 5880 (ε_r = 2.2; tanδ = 0.0009; h=0.7874 mm) substrate and fed by an open-ended microstrip line. The distance between the side of the slot-ring antenna and the edge of the ground plane is marked as d. In order to study the ground plane size effects, *d* is changed from $0.41\lambda_0$ to $1.53\lambda_0$. During the change, the center frequency of the slot-ring antenna is maintained at 6.27 GHz. However, the radiation pattern of the slot-ring antenna varies with different ground plane sizes as shown in Fig. 2.8 (b). It can be seen that as the ground plane size increases, the radiation pattern becomes more and more undulating. This phenomenon is caused by diffraction at the edge of the ground plane which was studied in [82]. For a slot-ring antenna with a finite ground plane, the electric-field distribution becomes discontinuous at the edges. This E-field discontinuity will result in reflected waves which will interfere with the direct wave from the slot-ring antenna and affect the radiation pattern of the antenna. The magnitude of the reflected wave decreases as d increases. If the slot-ring antenna is located at the center of the ground plane, the positions of the maximums and minimums in the pattern can be predicted by:

$$\theta = \arcsin(\frac{n\lambda_0}{2d}) \tag{2.1}$$

where λ_0 is the free space wavelength [82]. In this case, for a reconfigurable slot-ring antenna with a certain ground plane size, the positions of the maximums and minimums are different based on equation (2.1) since the electrical size of the ground plane for the lower band and the upper band are different. Thus, different radiation patterns of the reconfigurable slot-ring antenna at upper and lower frequency bands are observed. Particularly for the reconfigurable slot-ring antenna shown in Fig. 2.6 (a), the radiation pattern at the upper frequency band is tilted because the smaller slot-ring is located off center of the ground plane.

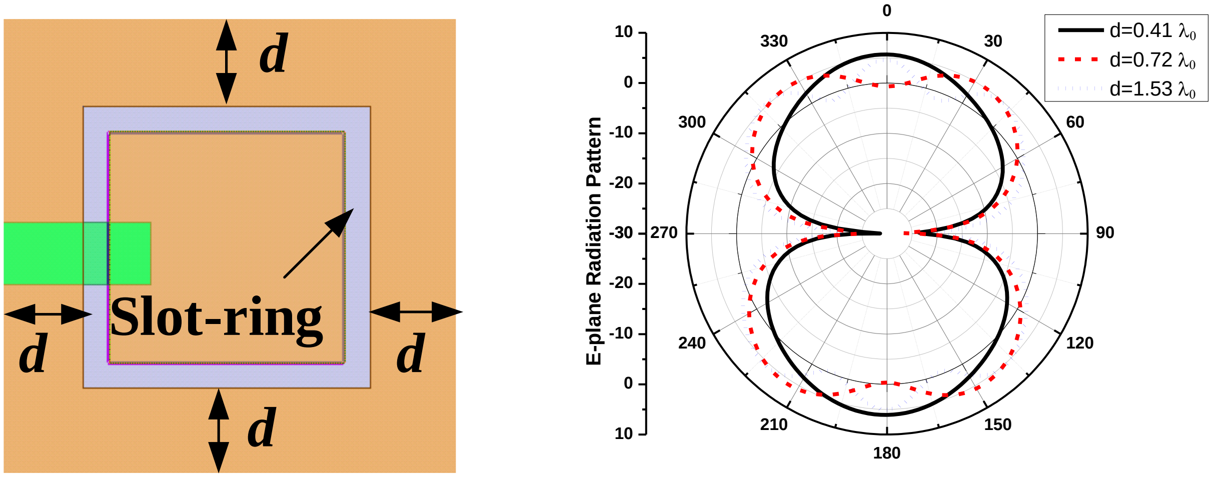

(a)

(b)

Figure 2.8: (a) Slot-ring antenna operating at 6.27 GHz; (b): E-plane radiation patterns of the slot-ring antenna for different ground plane sizes.

To further explore the effects of ground plane edge diffraction on the radiation pattern of the slot-ring antenna array, the radiation pattern of a 5×5 slot-ring antenna array is investigated. The radiation pattern of the antenna array is realized by two methods: directly simulating the entire array in ANSYS High Frequency Structure Simulator (HFSS), and simulating a unit cell by applying periodic boundary conditions.

Fig. 2.9 (a) shows a slot-ring antenna unit cell with periodic boundary conditions in HFSS. Perfect Matching Layers (PML) boundary conditions are defined at the top and bottom of the air box to simulate the radiation performance. Two pairs of master and slave boundaries are applied to four sides of the entire structure, including the airbox and the PML, to realize a periodic boundary condition [83-84]. By multiplying the array factor and the radiation pattern of the unit cell antenna with periodic boundary conditions, the radiation pattern of the 5×5 antenna array is acquired [4].

Fig. 2.9 (b) compares the radiation pattern obtained by simulating the entire 5×5 array with that achieved by multiplying the array factor with the radiation pattern of the unit cell with periodic boundary conditions. The two methods match well with each other and a broadside pattern without any ripples is observed. This illustrates that the radiation pattern of the slot-ring antenna array is not influenced by edge diffraction. For the reconfigurable slot-ring antenna, the ground-plane-size-dependent radiation pattern should not be a problem for reconfigurable slot-antenna array applications.

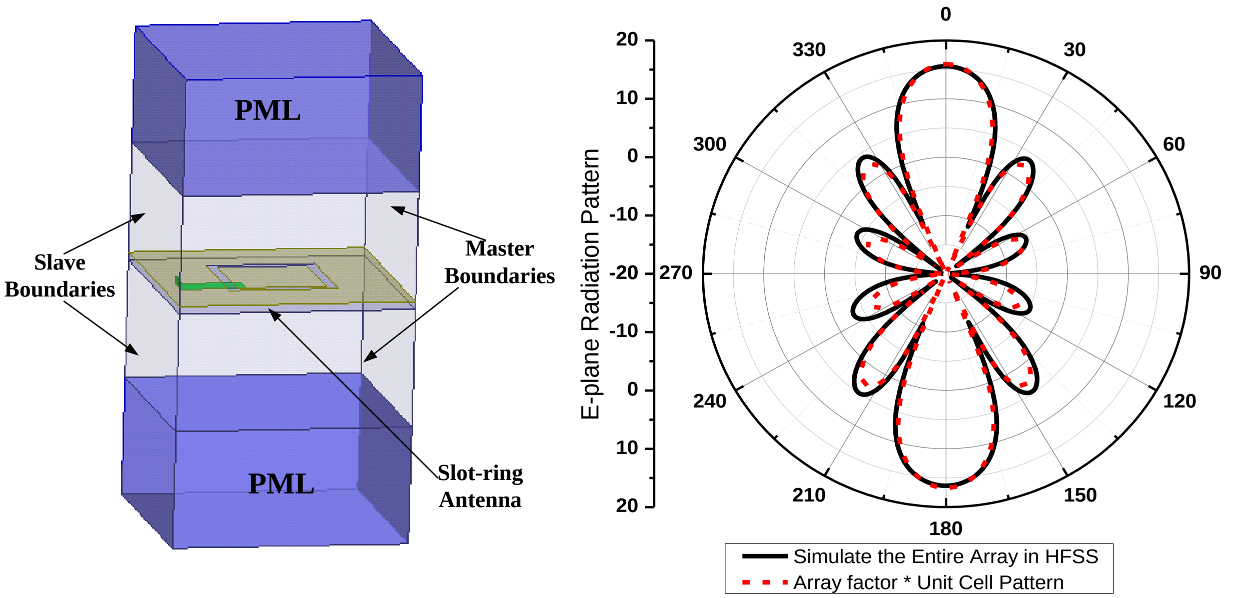

Figure 2.9: (a) Slot-ring antenna operating at 6.27 GHz; (b): E-plane radiation patterns of the slot-ring antenna for different ground plane sizes.

2.5 Conclusion

An *S*-band continuously-tunable slot-ring antenna has been successfully designed, fabricated and measured and the antenna gain and patterns are very close to simulations. The return loss of the antenna can be further improved by incorporating more accurate varactor models in future designs. This S-band reconfigurable antenna is extended to realize a reconfigurable antenna array which covers a frequency range of 1-4 GHz.

The effect of the ground plane size on the radiation pattern of the slot-ring antenna is also studied. It was found that the radiation pattern of a single slot-ring antenna is dependent on the size of the ground plane. Although the single slot-ring antenna is used as the unit cell in the larger slot-ring antenna array, it has been verified by two full-wave methods that this problem will not exist in the full array.

CHAPTER 3 SINGLE-SIDED RADIATION OF FRACTAL-SHAPED RECONFIGURABLE SLOT-RING ANTENNA/ARRAYS

The reconfigurable slot-ring antenna with switches and varactors presented in Chapter 2 can tune continuously over a frequency range from 1 to 4 GHz. However, the bandwidth of the reconfigurable slot-ring antenna array is narrow and the DC bias networks to control the switches and varactors are complicated. In order to simplify the bias network and increase the bandwidth of the reconfigurable slot-ring antenna array, fractal stubs and wide slot-rings are introduced in this chapter. The fractal-shaped reconfigurable slot-ring antenna array can cover from 2 to 8 GHz with a reduced number of switches and no varactors. By turning the switches 'ON' or 'OFF', the fractal-shaped reconfigurable slot-ring antenna can operate either in S-band or C-band. Furthermore, ground plane solutions to reduce the back-side radiation of the fractal-shaped slot-ring antenna/array are provided in this chapter. Both the simulation and measurement results of the fractal-shaped reconfigurable slot-ring antenna with single-sided radiation are presented in this chapter.

3.1 Introduction of the Fractal-Shaped Reconfigurable Slot-Ring Antenna/Array

Slot-ring antennas are considered to be good candidates in reconfigurable communication systems because their resonant frequency can be easily tuned by varactors or switches. In addition, polarization flexibility of the slot-ring antenna can be achieved by using two orthogonal feeding lines [26]. A novel reconfigurable slot-ring antenna array using PIN diode switches and varactors was presented in chapter 2. The pixelated slot-ring antenna can achieve tuning in frequency, polarization, and radiation pattern but with narrow bandwidth. In order to enhance the bandwidth and maintain the tunability of the aforementioned RF parameters, a fractal-shaped reconfigurable slot-ring antenna array is presented in Fig. 3.1. The antenna array is formed by four smaller dual-feed fractal slot-ring antennas. The PIN diode switches bridging the slots of the antenna are used to realize the frequency reconfigurability. By turning the switches ON or OFF, the antenna can work as either a 2×2 *C*-band antenna array or a single *S*-band antenna; the fractal shapes of the antenna can enhance the fractional bandwidth. Therefore, the fractal-shaped reconfigurable slot-ring antenna is able to cover almost the entire *C* or *S* band. The radiation pattern of the 2×2 *C*-band antenna array is able to be reconfigured if different phases are applied to each antenna element. In addition, by feeding the antenna with a microstrip line from either vertical or horizontal direction, the polarization of the antenna can be controlled. Moreover, compared with the reconfigurable slot-ring antenna designed in Chapter 2, this fractal-shaped reconfigurable slot-ring antenna reduces the number of switches from 16 to 8. Since the fractal-shaped slot-ring antenna has an enhanced bandwidth, varactors are not necessary to fully cover the 2 to 8 GHz frequency range. Additionally, since the structure of the fractal-shaped antenna array is self-similar, it can be easily extended to a larger reconfigurable antenna array covering from 2 to 12 GHz as shown in Fig. 3.2.

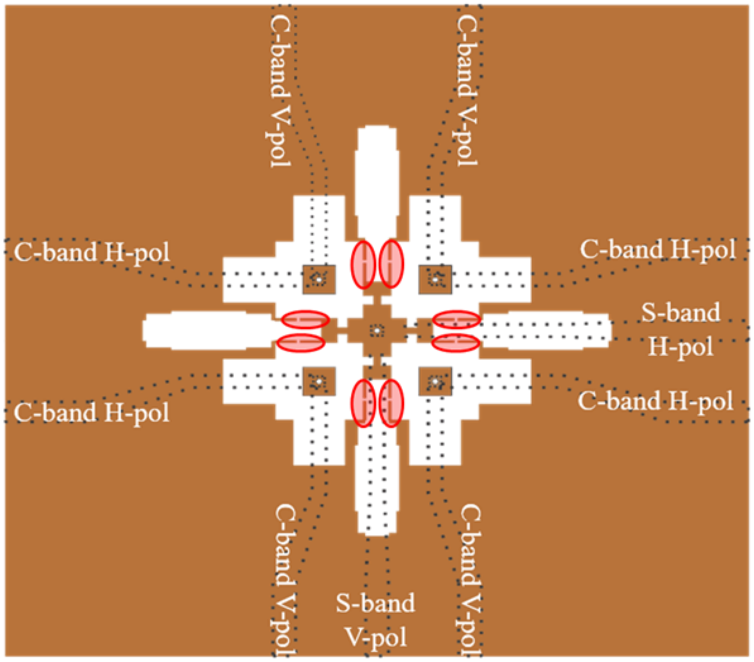

Figure 3.1: A schematic of a fractal-shaped reconfigurable slot-ring antenna array covering *S* and *C* bands.

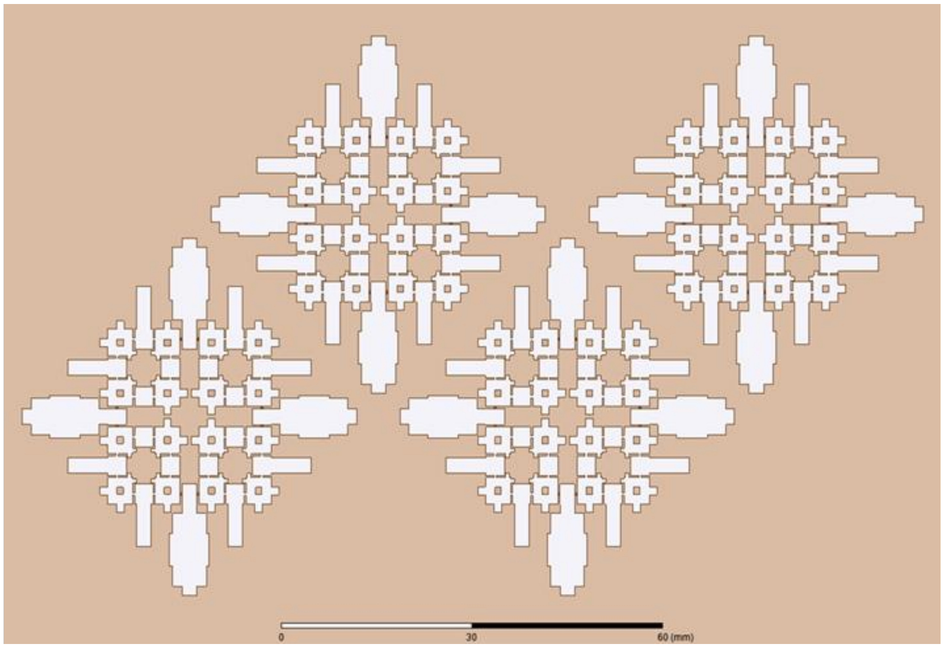

Figure 3.2: An extended fractal-shaped reconfigurable slot-ring antenna array covering *S*, *C* and *X* bands.

3.1.1 Fabrication of the Fractal-Shaped Reconfigurable Slot-Ring Antenna/Array

Fig. 3.3 shows the fabricated fractal-shaped reconfigurable slot-ring antenna array. 8 PIN diode switches from Skyworks (DSM8100) are mounted on the top surface as shown in Fig. 3.3(b). A copper wire is soldered through a via-hole located at the center of the antenna. The DC bias wire is placed perpendicular to the substrate in order to reduce its effects on the radiation performance of the antenna as shown in Fig. 3.3(c). When all the PIN diode switches are OFF, the fractal-shaped slot-ring antenna operates at *S* band. Similarly, when all the PIN diode switches are turned ON, the fractal-shaped antenna works as a 2×2 *C*-band antenna array.

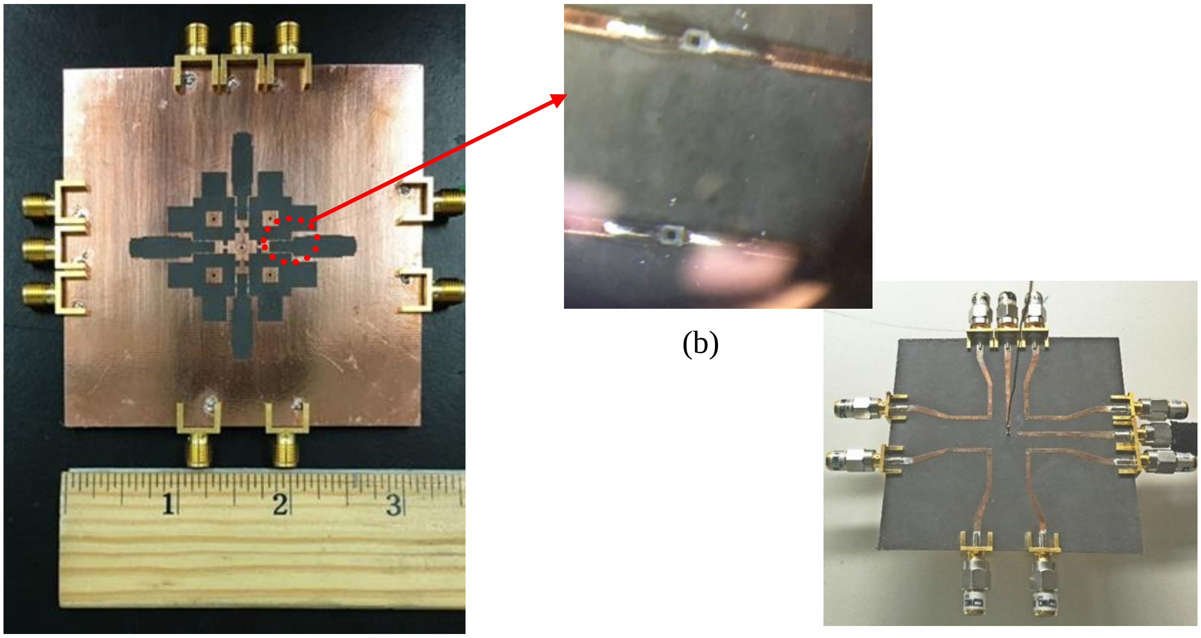

(b)

(a)

(c)

Figure 3.3: Fabricated double-sided fractal-shaped slot-ring antenna. (a) Top view; (b) Switches under a microscope; (c) Bottom view.

3.1.2 Measurement of the Reconfigurable Slot-Ring Antenna/Array at S band

In this section, the measured and simulated return loss, isolation, gain, and pattern of the double-sided fractal-shaped slot-ring antenna operating at *S* band are presented.

The measured return losses of both H- and V-pol at *S* band are shown in Fig. 3.4 (a) and (b). The symmetry between two polarization states is apparent. When the switches are turned off, the antenna is in *S*-band operation mode. When the switches are turned on, the antenna is operating in *C*-band mode. As can be seen in Fig. 3.4(a), when the switches are off, the measured return loss is more than 7.5 dB from 1.8 to 3.6 GHz (octave bandwidth); the simulated return loss is better than 9.5 dB in this band. We believe that the return loss can be further optimized to be above 10dB in our next design. When the switches are on, the return loss is below 2dB from 1.8 to 3.6 GHz, which means that most energy will be reflected back to the feeding port.

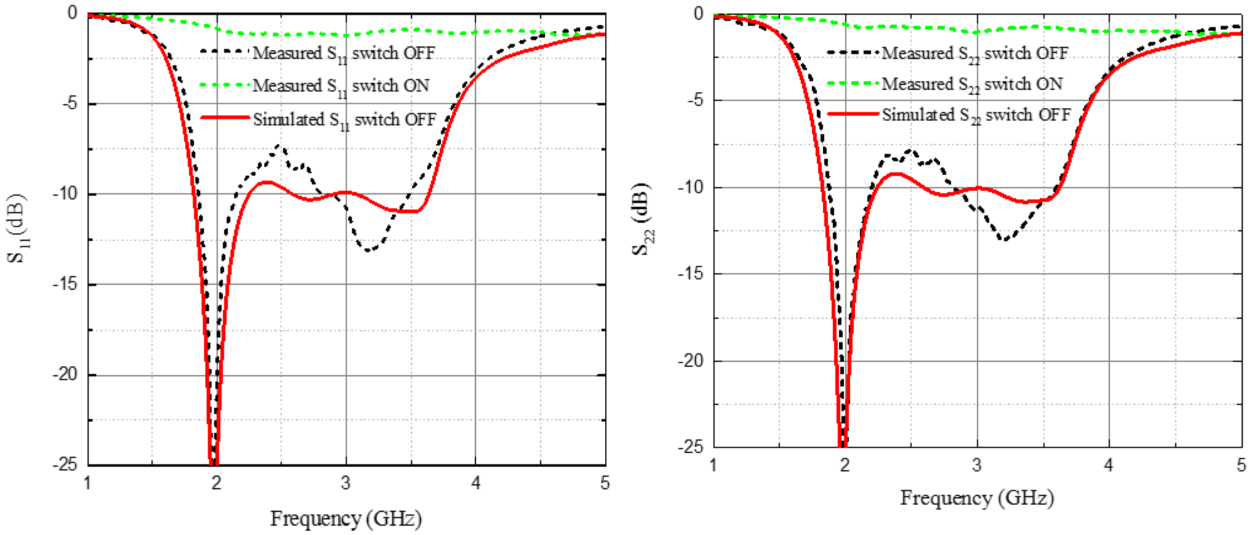

(a) (b)

Figure 3.4: Simulated and measured return losses. (a) H-pol. (b) V-pol.

Fig. 3.5 shows the simulated and measured isolation between different ports which are labeled in Fig. 3.5 (a). Though the isolation between all 10 ports was measured, we only present the two most important ones since they are much larger than the others. It is shown in Fig. 3.5 (b) that the isolation between Ports 1 and 2 is higher than 6dB. The measured isolation between Ports 1 and 3 is greater than 7.5dB. The limited level of isolation reduces the gain of the antenna since a certain amount of energy is coupled to these ports instead of being radiated. In our next design, we will improve the isolation performance by either (1) further separating the feeding lines or (2) using open-ended port terminations.

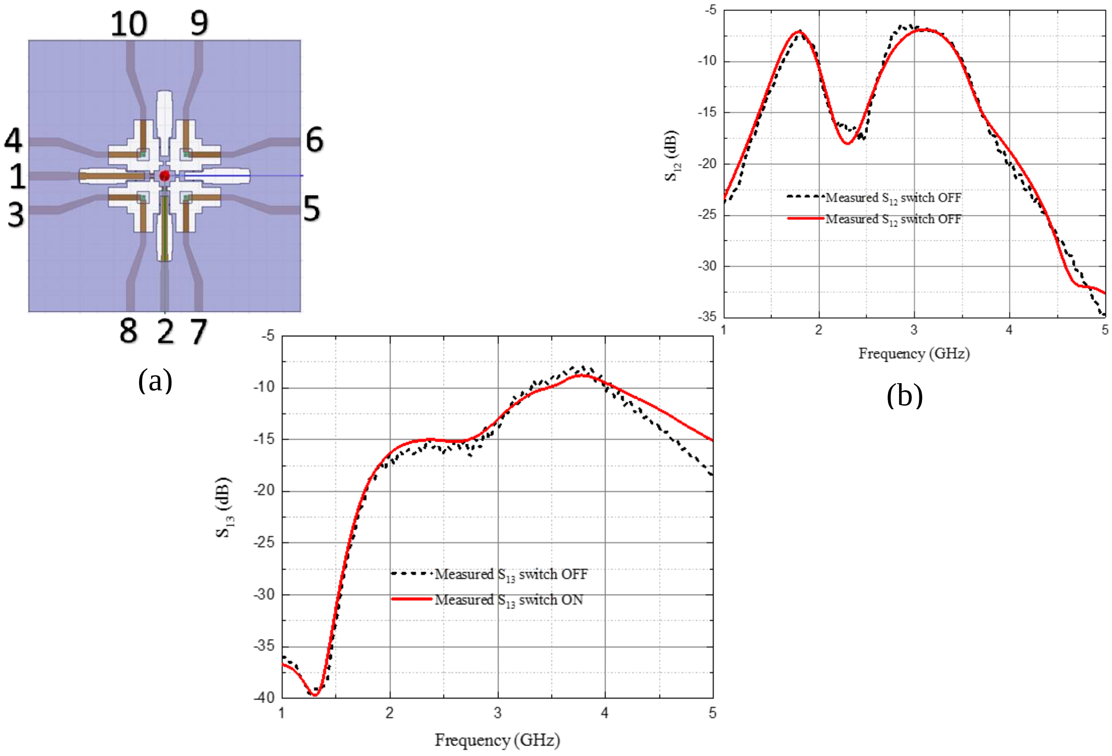

(a)

(b)

(c)

Figure 3.5: Simulated and measured isolation between different ports. (a) Antenna port numbering. (b) Isolation between the horizontal and vertical polarizations at *S* band; (c) Isolation between the adjacent S-band and *C*-band feeding lines.

Fig. 3.6 shows the simulated realized gain compared to the measured gain of the double-sided fractal-shaped slot-ring antenna in *S*-band operation mode. Measured gain versus frequency has a trend similar to the simulated gain. Both the measured and simulated gain increase with frequency below 2.5 GHz. Then the gain decreases between 3 and 3.6 GHz, which is due to the increased coupling between Port 1 and other ports. Above 3.6 GHz, the gain decreases because the return loss goes up as shown in Fig. 3.4 (a). At 2.2 GHz, the measured gain is about 2 dB higher than the simulated gain, which is due to the higher directivity.

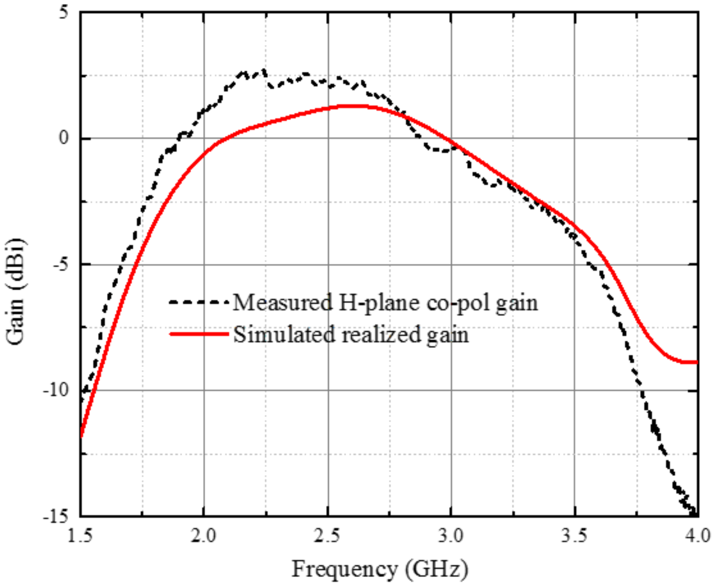

Figure 3.6: Simulated and measured gain when the antenna is in *S*-band operating mode.

Co-pol and X-pol measured radiation patterns in E- and H-planes are compared to the simulations in Fig. 3.7-3.9 at three different frequency points and good agreement between the simulated and measured radiation patterns in the E-plane is observed. The measured H-plane pattern is narrower than the simulated one at 1.8 GHz which results in a higher measured gain. At 2.7 and 3.5 GHz, the measured H-plane patterns are similar to the simulations. The cross-polarization level is about -9 dB, which will decrease significantly when the antenna is used in an array.

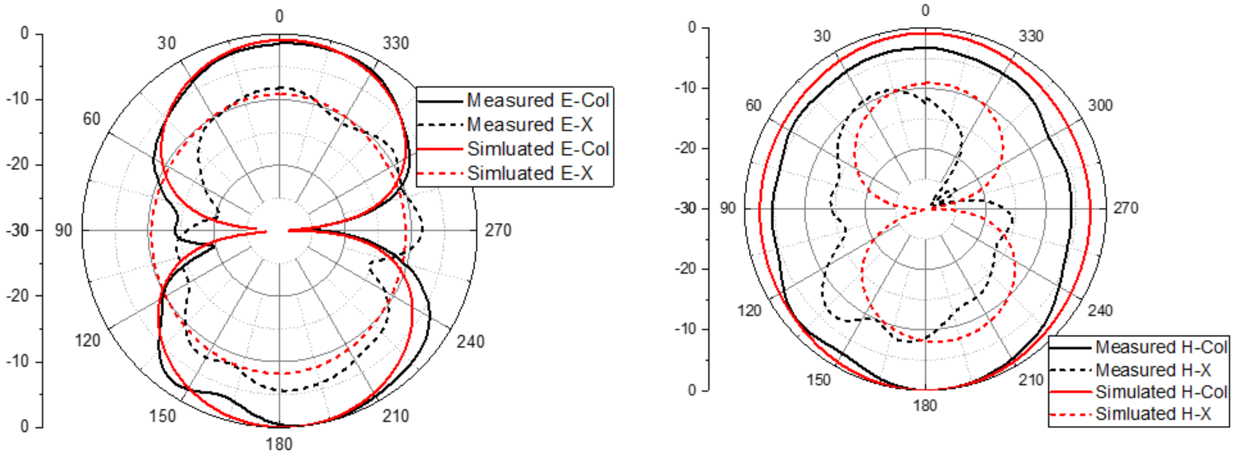

(a) (b)

Figure 3.7: Radiation pattern at 1.8 GHz a) E-plane; b) H-plane

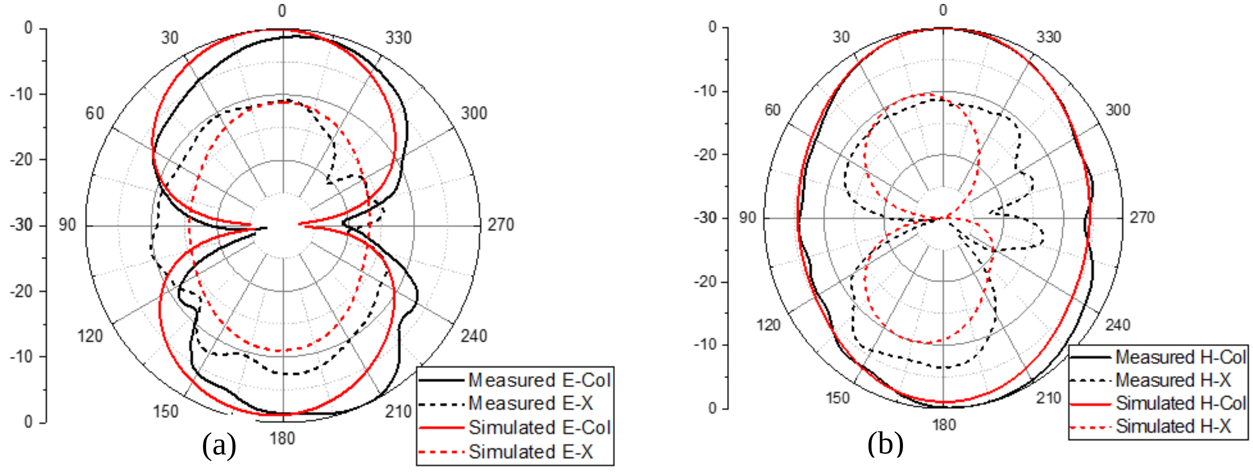

(a) (b)

Figure 3.8: Radiation pattern at 2.7 GHz a) E-plane; b) H-plane.

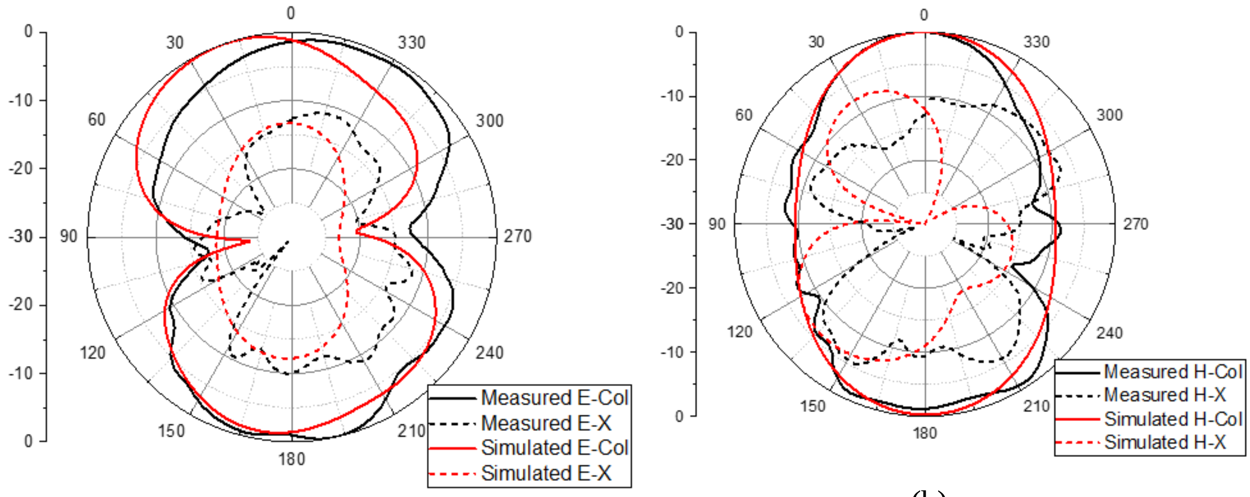

(a)

(b)

Figure 3.9: Radiation pattern at 3.5 GHz a) E-plane; b) H-plane.

3.1.3 Measurement of the Reconfigurable Slot-Ring Antenna/Array at C band

In this section, we are going to study the return loss, isolation, gain, and pattern measurements of the double-sided fractal-shaped slot-ring antenna operating at C band.

The measured return losses of both H- and V-polarization of the fractal-shaped slot-ring antenna at *C* band are shown in Fig. 3.10(a) and (b) and symmetry between two polarization states is observed. When the switches are turned on, the antenna is in *C*-band operation mode and it can be seen in Fig. 3.10(a) that the measured return loss is better than 10 dB from 5.1 to 8 GHz. We have to mention that the active-S1 bandwidth is wider than the S_{11} bandwidth. In the array application, active-S1 bandwidth is more important.

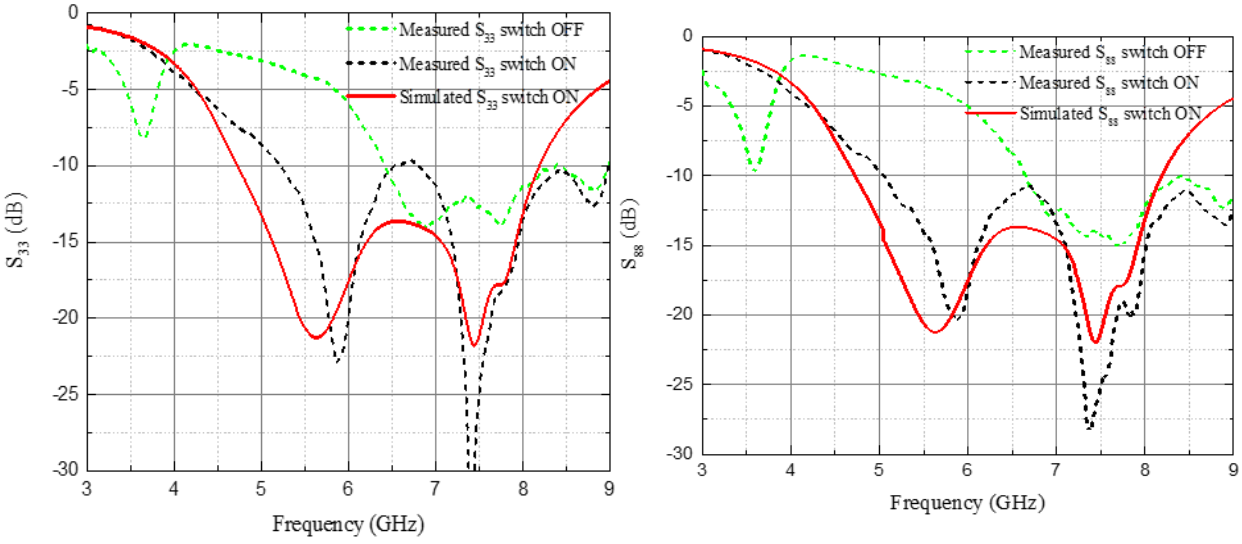

(a) (b)

Figure 3.10: Simulated and measured return loss in *C*-band operation mode. (a) H-pol. (b) V-pol.

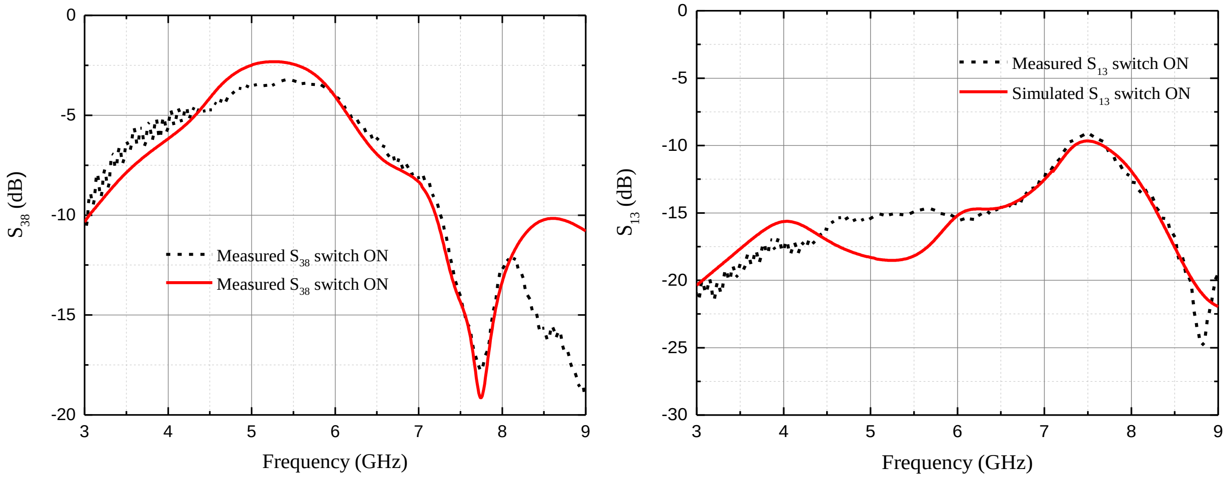

(a)

Figure 3.11: Simulated and measured isolation between different ports. (a) Isolation between the horizontal and vertical polarizations at C-band. (b) Isolation between the adjacent S-band C-band feeding lines.

Fig. 3.11 shows the simulated and measured isolation between different ports that are labeled in Fig. 3(a). It can be seen from Fig. 10 (a) that the isolation between Ports 3 and 8 is higher than 3dB because the two ports are very close to each other physically. The measured isolation between Ports 3 and 1 is greater than 9dB.

In the *C*-band gain and pattern measurements, a commercial wide-band (2-8 GHz) power divider and two wide-band (2-8 GHz) 180° hybrids are used to achieve a 180° phase difference between the upper and lower elements as shown in Fig.3.12.

Fig. 3.13 shows the simulated realized gain compared to the measured gain of the double-sided fractal-shaped slot-ring antenna in *C*-band operation mode. Measured gain matches very well with the simulated gain. From 7 to 8 GHz, the measured gain is less than the simulated gain because in the measured gain, the maximum radiating direction is on the backside as shown in the measured radiation patterns.

Figure 3.12: Power divider and180^0 hybrids.

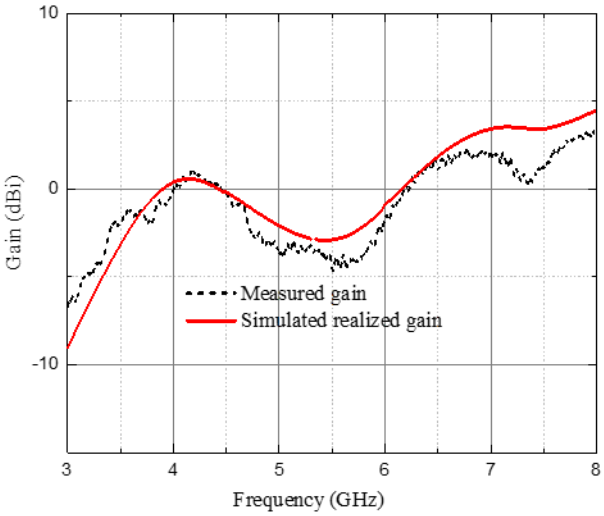

Figure 3.13: Simulated and measured gain vs frequency in C-band operation mode.

Co-pol and X-pol radiation patterns in the E- and H-planes are compared to the simulations in Fig. 12-14 at three different frequency points; the measurement results match the simulations well. The measured cross-polarization level is better than 10 dB. At 8 GHz, the maximum radiation in both the E- and H-planes is towards the back-side, which causes a lower boresight gain in the measurement.

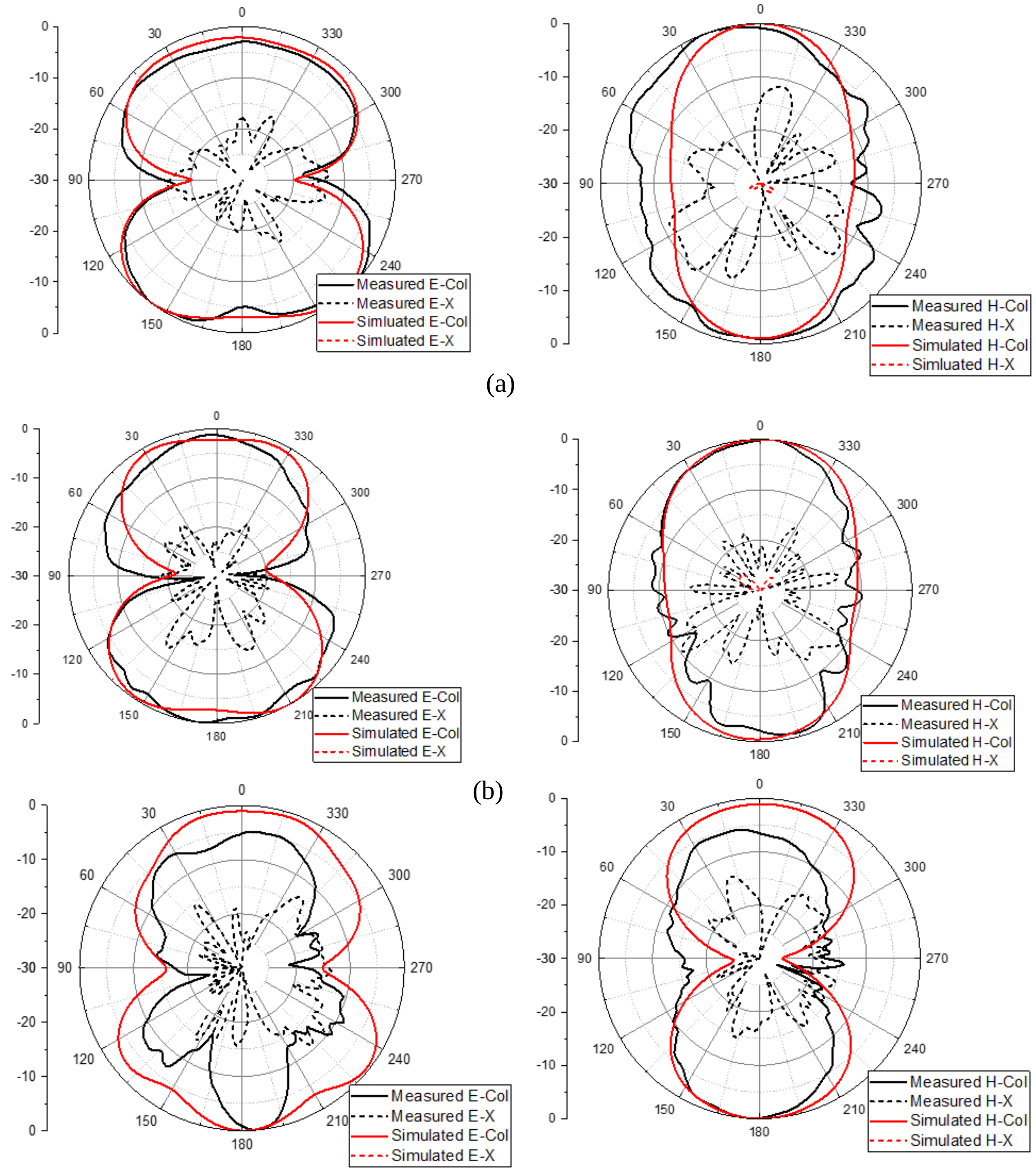

(a)

(b)

(c)

Figure 3.14: Radiation pattern at (a) 4.5 GHz; (b) 6.3 GHz; (c) 8 GHz

3.2 Single-Sided Radiation of the Fractal-Shaped Reconfigurable Slot-Ring Antenna using Metal Planes

From the previously measured results of the fractal-shaped reconfigurable slot-ring antenna array, we can see that the antenna array can be switched between *S* and *C* band by applying different DC voltages. In addition, since the fractal-shaped reconfigurable slot-ring antenna array has both vertical and horizontal feeding networks for each frequency band, dual polarization of the antenna array is achieved. From the measured radiation patterns, it is noted that the reconfigurable dual-band slot-ring antenna exhibits bi-directional radiation. However, in many wireless communication systems, the backside radiation is undesirable. Therefore, a ground plane solution for the fractal-shaped reconfigurable dual-band slot-ring antenna using finite conductors is presented in this section. By using a metal plane underneath the fractal-shaped slot-ring antenna array and optimizing the distance between the antenna and the metal plane, single-sided radiation of the reconfigurable dual-band slot-ring antenna is achieved.

3.2.1 Design and Fabrication of the Metal-Backed Fractal-Shaped Reconfigurable Slot-Ring Antenna/Array

Fig. 3.15(a) shows a metal plane which can be placed below the fractal-shaped reconfigurable slot-ring antenna array. When the metal plane is placed underneath the antenna with a distance *d*, as a first order assumption, there is round-trip phase delay for the wave to go back and forth from the metal surface as shown in Fig. 3.15 (b). The phase delay is a function of the distance *d* and the frequency *f* which can be estimated by:

$$\phi_{delay} = 2 \cdot \frac{2\pi d \cdot f}{c} \tag{3.1}$$

where *c* is the speed of light. In the first order assumption, the total reflection phase of the backside wave is equal to the sum of the reflection phase of the metal surface and the round-trip phase delay, which is a function of *d*. The reflection phase from the metal plane is always to be 180^0 as shown in Fig. 3.15 (c). In order to get a total $\pm 90^0$ in-phase frequency range from 2.0 to 8.0 GHz as shown in Fig. 3.15(d), *d* = 15 mm is selected.

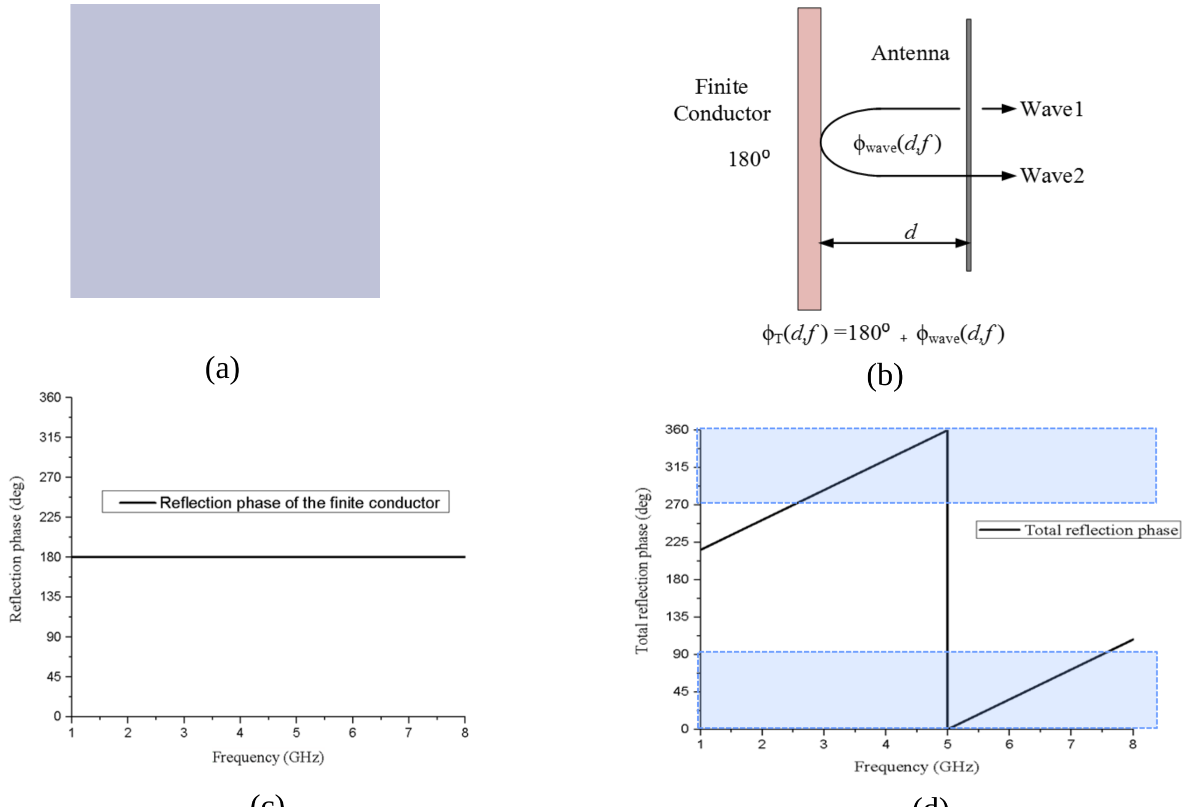

(a)

(b)

(c)

(d)

Figure 3.15: (a) Finite conductor; (b) Reflection phase of the finite conductor; (c) Antenna backed with the finite conductor with a distance; (d) Total Reflection phase at *d* =15 mm.

The fractal-shaped reconfigurable slot-ring antenna backed by a metal plane is fabricated as shown in Fig. 3.16. A 15-mm-thick piece of foam is placed between the metal plane and the slot-ring antenna array for mechanical support. The DC bias wire is placed perpendicular to the substrate to reduce the cross polarization level of the fractal-shaped slot-ring antenna array. When applying different DC voltages to the bias via, the antenna can be switched between *S* and *C* band. Plastic brackets made by a 3D printer are used to mount the antenna.

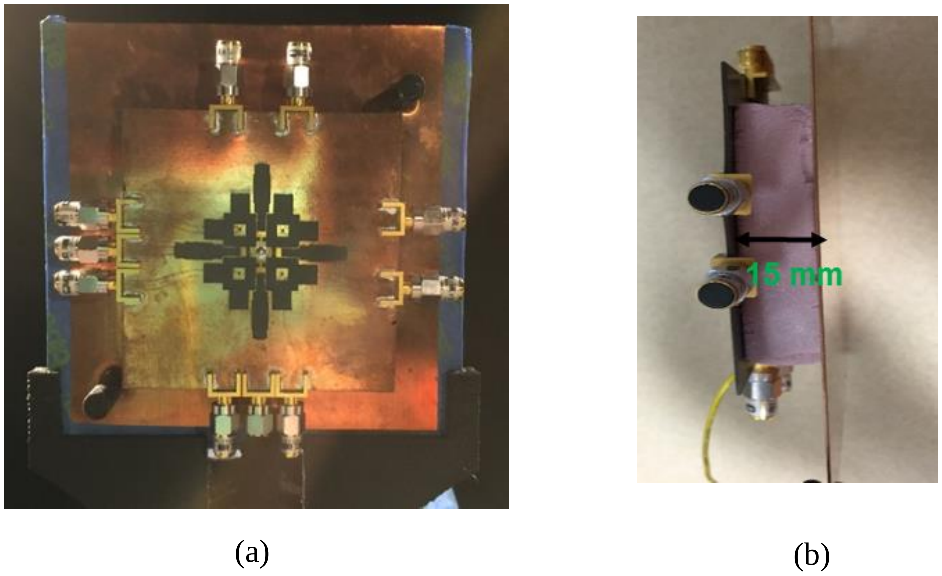

(a) (b)

Figure 3.16: Fabricated fractal-shaped reconfigurable slot-ring antenna backed with metal plane: (a) Top view; (b) Side view.

3.2.2 S-band Measurement of the Metal-Backed Fractal-Shaped Reconfigurable Slot-Ring Antenna/Array

The measured return losses of both H- and V-polarizations are shown in Fig. 3.17 (a)-(b). When the switches are turned off, the return loss of the metal-backed fractal antenna at *S* band is better than 7 dB from 1.9 to 3.6 GHz for both vertical and horizontal polarizations.

The isolation between different ports are also measured as shown in Fig. 3.17 (c)-(d). The isolation between Ports 1 and 2 is better than 6 dB as shown in Fig. 3.17 (c). The isolation between Ports 1 and 3 is better than 7 dB as shown in Fig. 3.17(d).

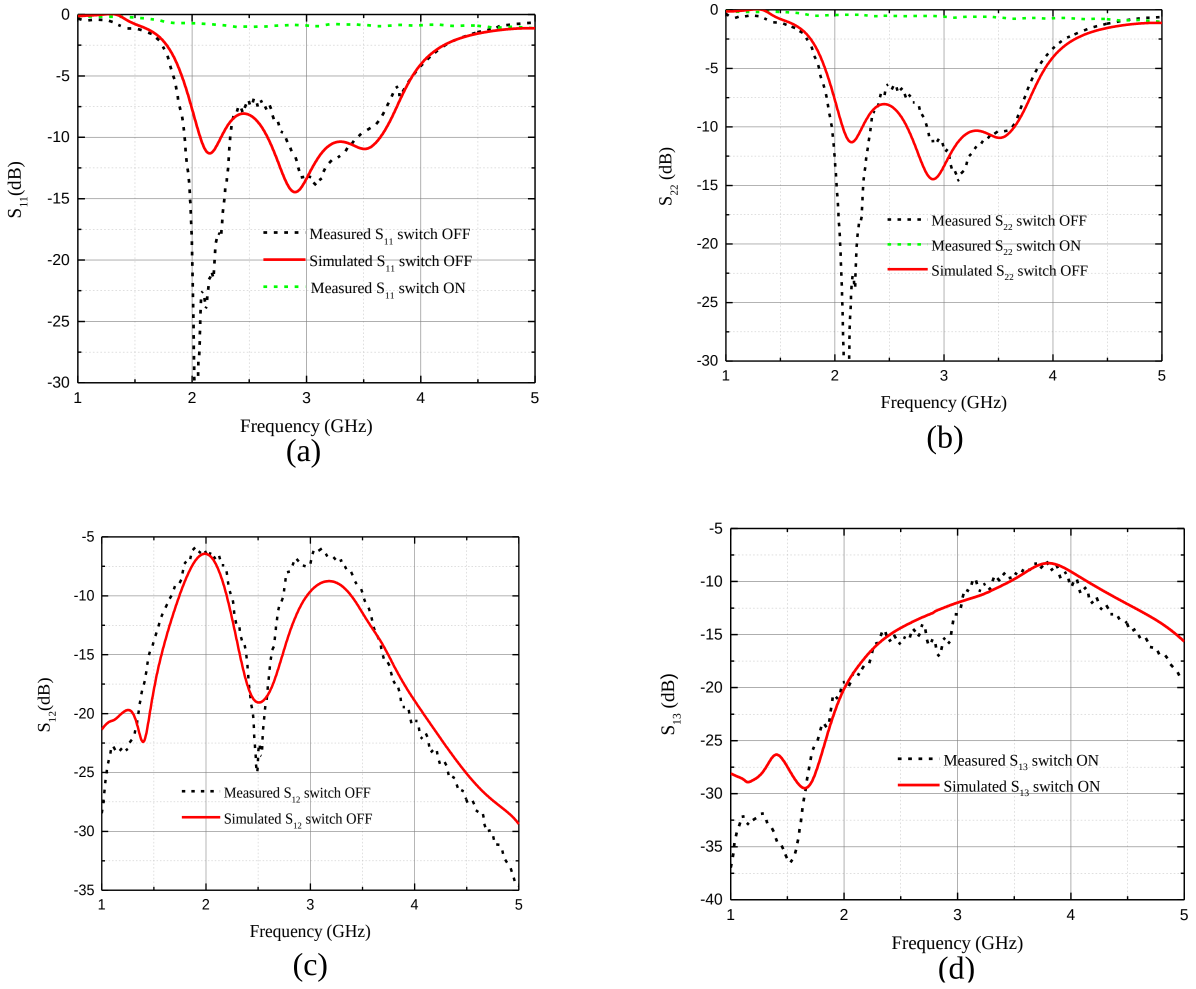

(a)

(b)

(c)

(d)

Figure 3.17: Measured and simulated return loss of (a) vertical polarization; (b) horizontal polarization; Isolation between (a) Ports 1 and 2; (b) Ports 1 and 3.

The gain of the metal-backed fractal-shaped slot-ring antenna at *S* band is also measured. The measured realized gain vs. frequency is shown in Fig. 3.18. In general, the measured gain matches the simulated gain. Around 3 GHz, the measured gain is about 3.5 dB less than the simulation result, which is due to the return loss, isolation, and radiation pattern. From the simulated and measured return loss and isolation between port 1 and other 9 ports, we can calculate that the total measured incident power is about 1.6 dB less than the simulated total incident power. And also from the radiation pattern at 3 GHz, we can see that the measured pattern in the E-plane is broader than the simulated one as shown in Fig. 3.19 (a), while in H-plane, the measured pattern is similar to the simulated one as shown in Fig. 3.19 (b). Therefore, the lower measured gain is due to a lower incident power and a lower measured directivity.

Fig. 3.20 shows the Co-pol. and X-pol. radiation patterns in the E- and H- planes at 1.9, 2.7 and 3.5 GHz, respectively. Good agreement between the simulated and measured radiation patterns is observed. The cross-polarization level is about -6 dB, which will decrease significantly when the antenna is used in an array.

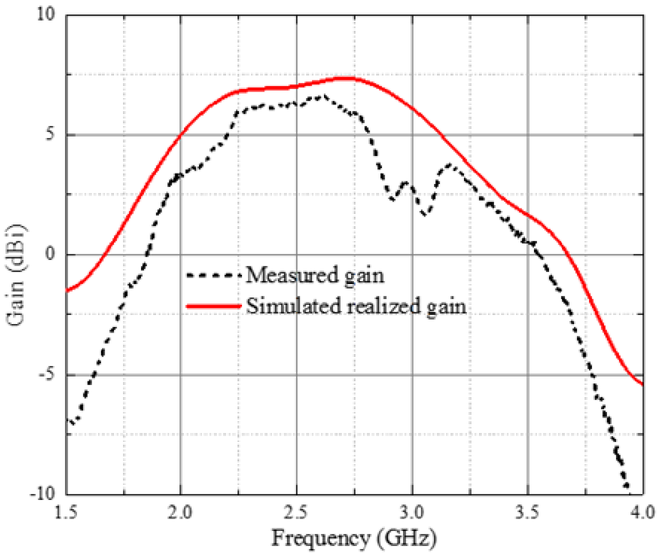

Figure 3.18: Measured and simulated gain vs frequency.

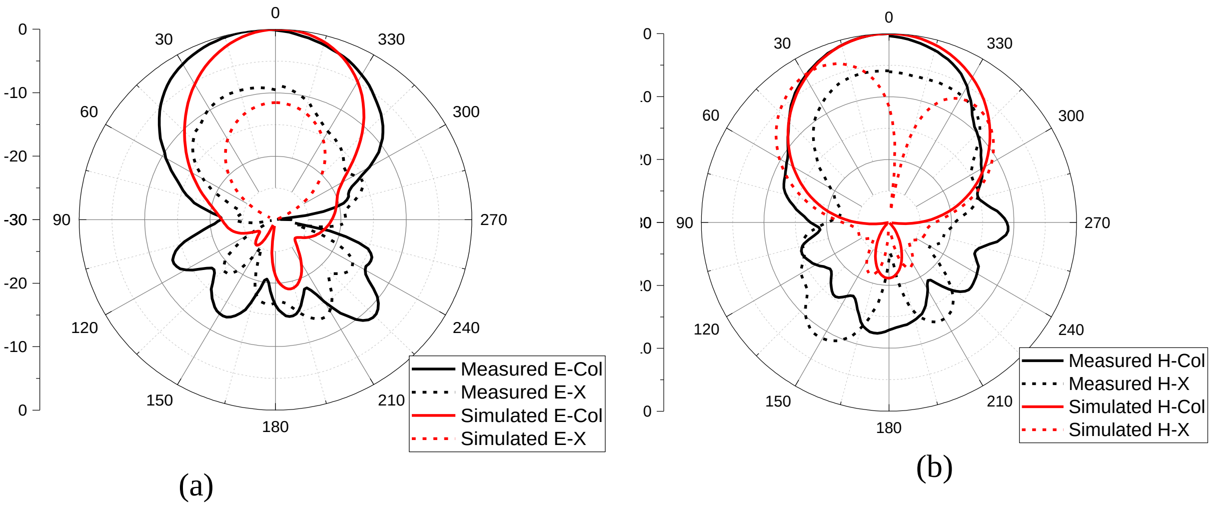

Figure 3.19: Radiation pattern at 3 GHz (a) E-plane pattern; (b) H-plane pattern.

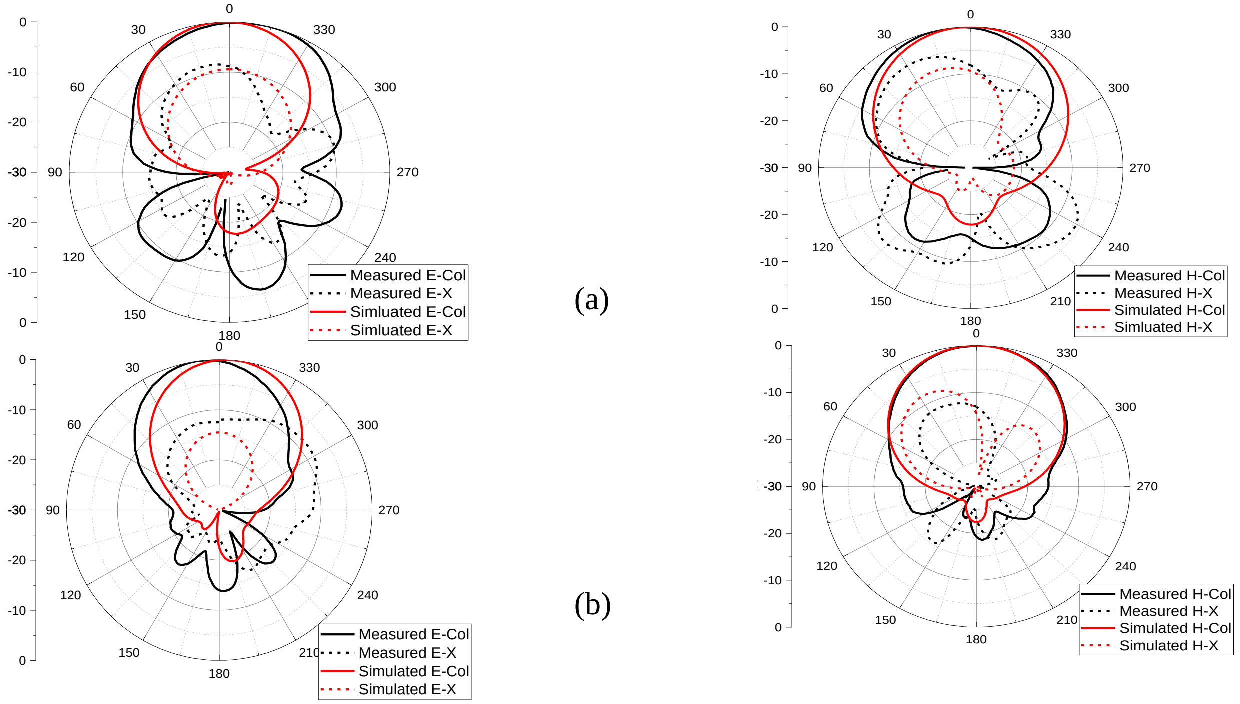

Figure 3.20: Radiation pattern at (a) 1.9 GHz (b) 2.7 GHz

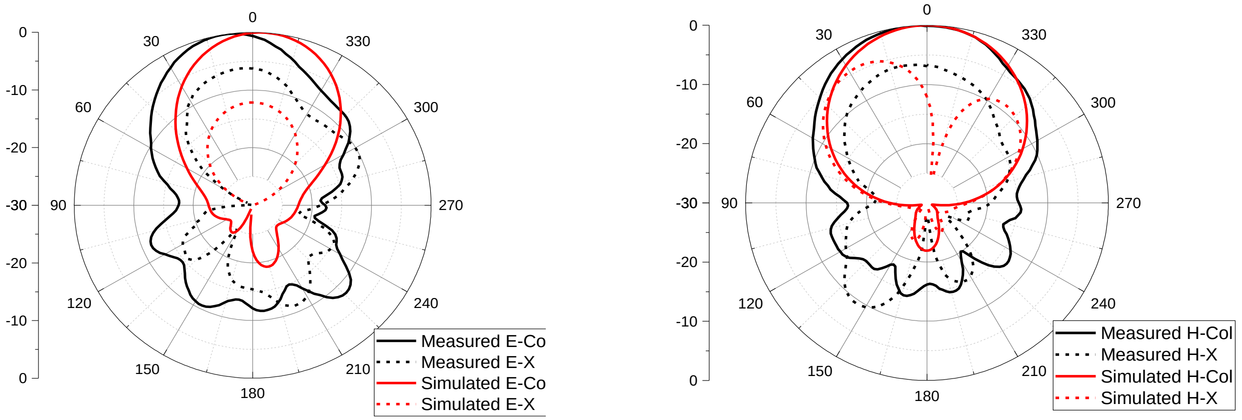

(c)

Figure 3.20(c): Radiation pattern at 3.5 GHz

3.2.3 C-Band Measurement of the Metal-Backed Fractal-Shaped Reconfigurable Slot-Ring Antenna/Array

The measured return losses of both horizontal and vertical polarizations at *C* band are shown in Fig. 3.21 (a)-(b). The measured return loss of the metal-backed fractal antenna at *C* band is better than 10 dB from 5.1 to 8 GHz for both vertical and horizontal polarizations. The isolation between different ports are also measured as shown in Fig. 3.21 (c)-(d). As shown in Fig. 39, the isolation between the H- and V-pol (ports 3 and 8) is only 2.5 dB, which is because the two ports are very close to each other. The isolation between the adjacent S- and C- band feeding lines (port 1 and 3) when the switches are “ON” is better than 9 dB.

The gain of the metal-backed fractal-shaped antenna at *C* band is measured and the measurement setup is shown in Fig. 3.22(a). The measured realized gain versus frequency is shown in Fig. 3.22(b) and has a similar trend as the simulated gain over frequency. However, there is a difference between the simulated and measured gain at boresight, which is due to the discrepancies between simulated and measured radiation pattern shown in Fig. 3.23. Edge diffraction causes the discrepancy between the measured and simulated radiation patterns which results in the difference between the measured and simulated boresight gain.

Fig. 3.23 shows the Co-pol. and X-pol. radiation patterns in the E- and H- planes at 4.5, 6.3 and 8 GHz, respectively. It is noted that at *C* band, the cross-polarization level is lower than 10 dB, but discrepancies between the simulated and measured radiation patterns at *C* band are observed. When absorbers are put on the edge of the antenna, it will slightly improve the radiation pattern but the boresight gain is reduced by about 1 to 2 dB.

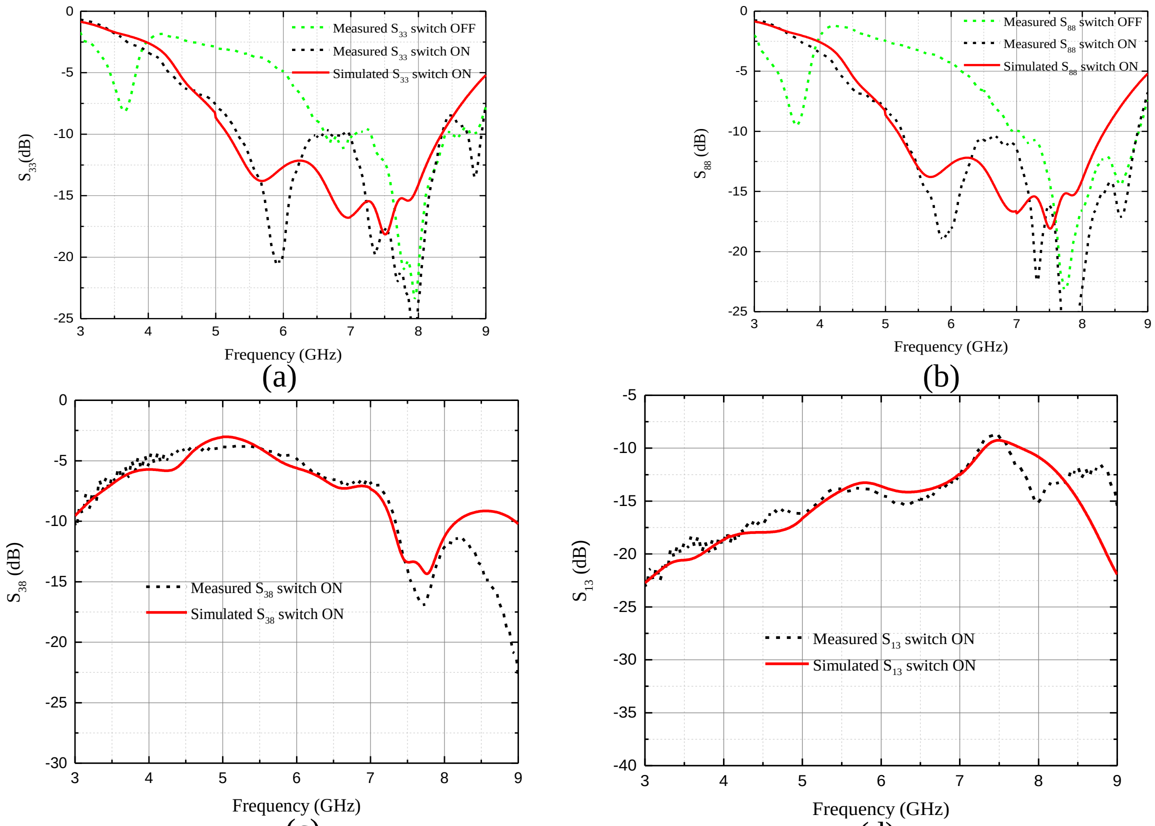

(a) (b)

(c) (d)

Figure 3.21: Measured and simulated return loss of (a) vertical polarization; (b) horizontal polarization; Isolation between (c) Ports 3 and 8; (d) Ports 1 and 3.

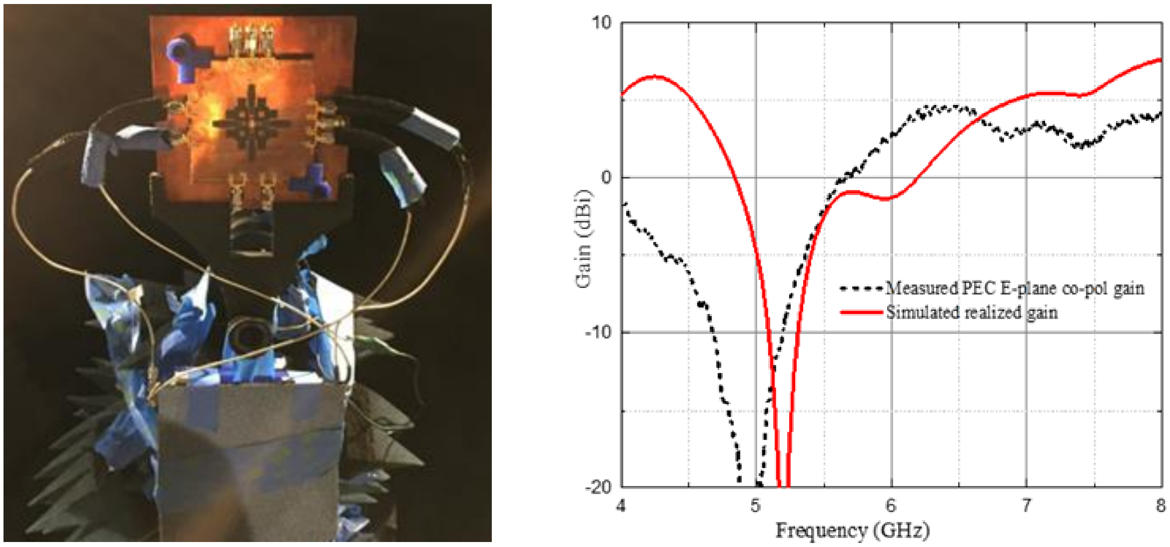

(a) (b)

Figure 3.22: (a) Measurement setup of the EBG-backed fractal antenna at *C* band; (b) Measured and simulated gain vs. frequency.

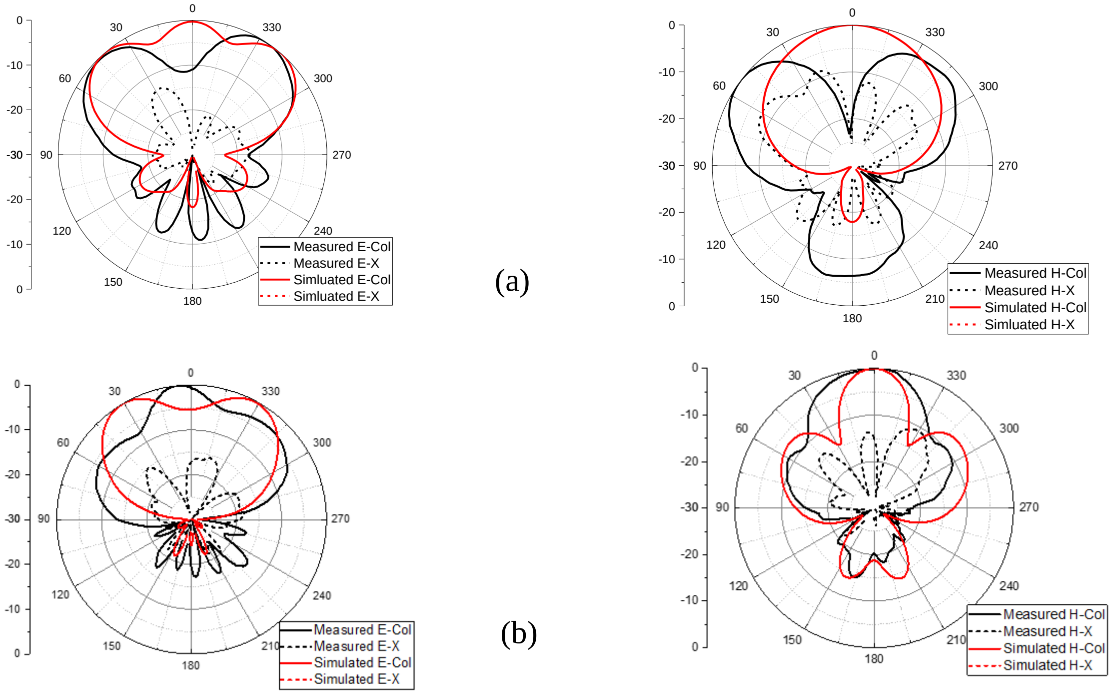

Figure 3.23: Radiation patterns at (a) 4.5 GHz; (b) 6.3 GHz.

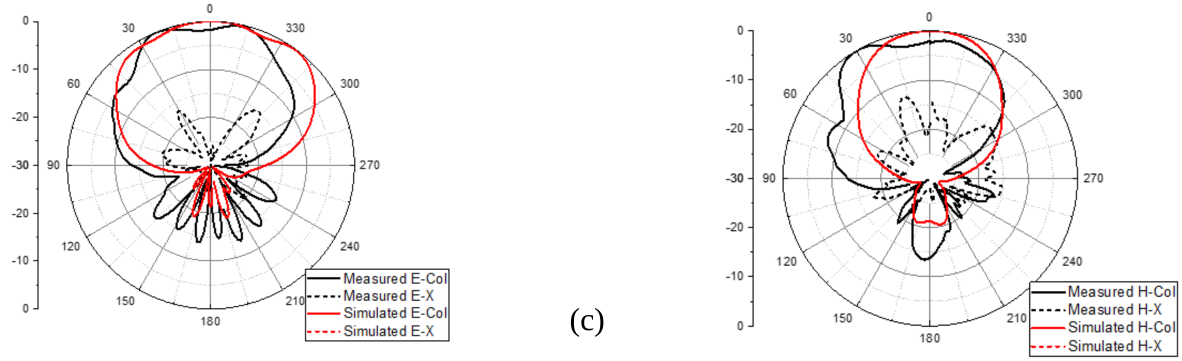

(c)

Figure 3.23 (c): Radiation patterns at 8GHz.

3.2.4 Gain Improvement of the Metal-Backed Fractal-Shaped Reconfigurable Slot-Ring Antenna/Array

From the above measurement results of the metal-backed fractal-shaped slot-ring antenna/array, it can be seen that by placing a metal plane underneath the antenna with an optimized distance, the backside radiation is reduced in both the *S*- and *C*-bands. The bandwidth of the metal-backed fractal-shaped reconfigurable slot-ring antenna/array only decreases slightly compared with the double-sided antenna/array. At *S*-band, the return loss is better than 7 dB from 1.9 to 3.6 GHz for both vertical and horizontal polarizations while at *C*-band, a return loss better than 10 dB from 5.1 to 8 GHz is observed. However, since the measured boresight gain of the antenna is not only related to the return loss but is also associated with port isolation and the radiation pattern, the measured gain of the antenna/array varies with frequency. At *S*-band, the measured gain decreases with frequency from 2.7 to 4 GHz, which is mainly due to the decreased isolation between different ports. When the antenna is operating in *C*-band, there is a null in the measured gain at 5.2 GHz because of the split radiation patterns. In this section several studies are presented in order to improve the realized gain of the antenna/array vs. frequency at both the *S*- and *C*-bands.

First, in order to remove the null at 5.2 GHz of the *C*-band metal backed antenna, the size of the substrate has been reduced as shown in Fig. 3.24 while the shape of the antenna remains the same. The realized gain of the antenna on the smaller substrate compared with the original design is shown in Fig. 3.25 and it can be seen that the null in the gain vs. frequency at 5.2 GHz disappears. The lowest realized gain happens at 6.8 GHz. Further study shows that the decreased realized gain at 6.8 GHz is due to the dip of the radiation pattern at boresight. Therefore, by reducing the size of the substrate and the metal plane, the realized gain vs. frequency at *C*-band is improved.

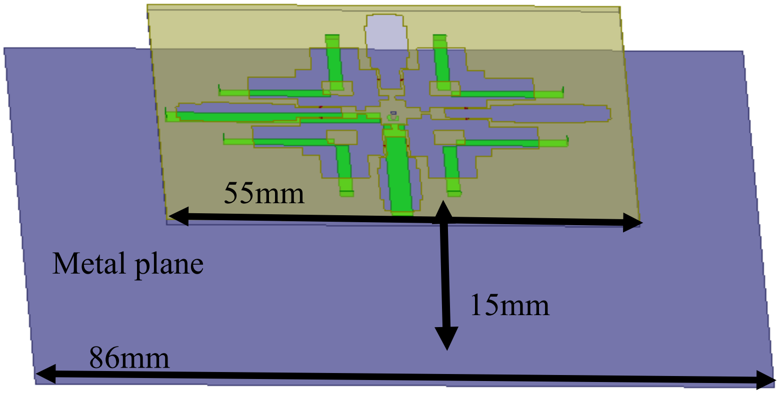

Figure 3.24: Reduced size of the substrate of the metal-backed antenna.

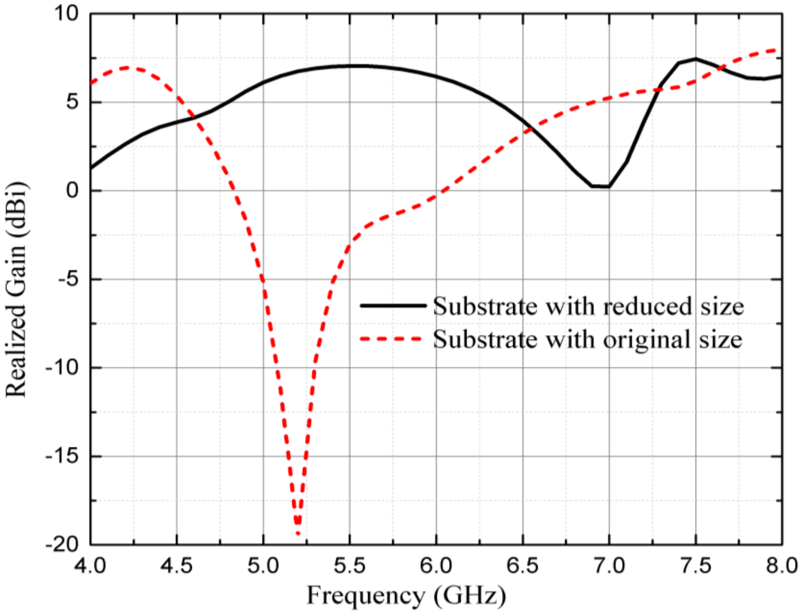

Figure 3.25: Realized gain of the antenna with different substrate dimensions at *C*-band.

With a substrate of the same size, the antenna at *S*-band is also simulated. The realized gain vs. frequency at *S*-band is shown in Fig. 3.26. At *S*-band, by reducing the size of the substrate, the realized gain above 2.9 GHz is higher than that of the original design. To further increase the realized gain of the antenna above 3 GHz, the fractal-shaped reconfigurable slot-ring antenna/array with a cut-corner substrate is investigated as shown in Fig. 3.27. It's shown that as the size of the cut-corner increases, the realized gain from 3 to 3.5 GHz increases, but the realized gain below 3 GHz decreases. Thus, the realized gain of the antenna/array is flatter during *S*-band when L = 15.5 mm.

To conclude, the realized gain of the fractal-shaped slot-ring antenna array at both *S* and *C* bands can be improved by shrinking the size and cutting corners of the antenna substrate.

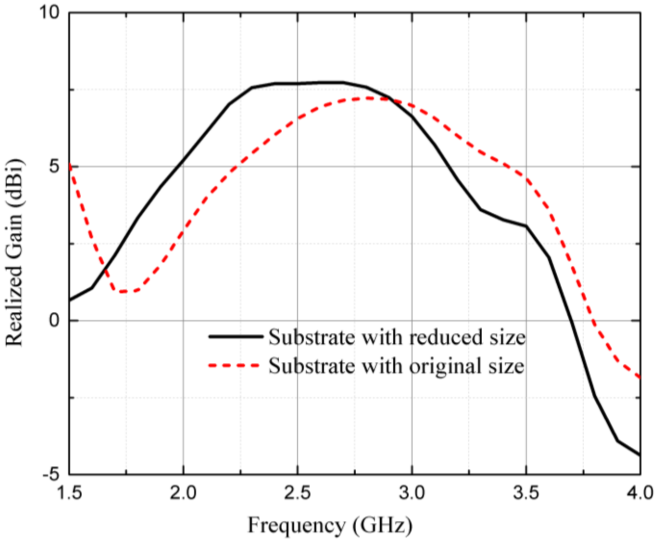

Figure 3.26: Realized gain of the antenna with different substrate dimensions at *S*-band.

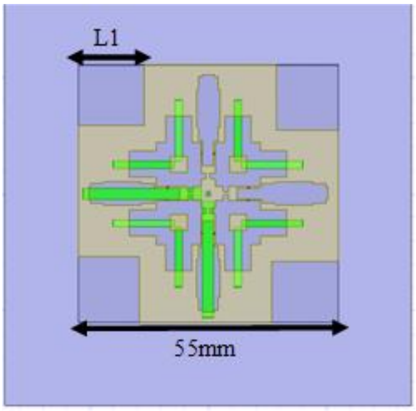

Figure 3.27: Fractal-shaped reconfigurable slot-ring antenna/array on a cut-corner substrate.

3.3 Single-Sided Radiation of the Fractal-Shaped Reconfigurable Slot-Ring Antenna/Array using Electromagnetic Band-Gap Surfaces

In section 3.2, metal planes are placed below the fractal-shaped reconfigurable slot-ring antenna/array to reduce the back-side radiation for both *S*- and *C*-band. The distance between the metal plane and the antenna/array is optimized in order to get a total in-phase ($\pm 90^{o}$) frequency range from 2.0 to 8.0 GHz. However, since the reflection phase from the metal plane is 180^{o} at different frequencies, the distance between the metal plane and the antenna/array is the only parameter which can be adjusted to meet the in-phase requirement. This limited the application of the metal plane to wider frequency bands. For the proposed tri-band reconfigurable slot-ring antenna/array shown in Fig. 3.2 which can cover from 2 to 12 GHz, metal planes cannot effectively reduce the back-side radiation over the entire frequency range. Therefore, an electromagnetic band-gap (EBG) surface which can potentially enable single-side radiation of the tri-band reconfigurable slot-ring antenna/array from 2 to 12 GHz is introduced here.

3.3.1 Design and Fabrication of the EBG-Backed Fractal-Shaped Reconfigurable Slot-Ring Antenna/Array

Fig. 3.29 (a) shows a mushroom-like EBG unit cell with periodic boundary conditions in ANSYS High Frequency Structure Simulator (HFSS). The EBG is designed on a RT/Duroid 5880 ($\varepsilon_r = 2.2$; $\tan\delta = 0.0009$; $h=12$ mm) substrate. The design parameters of the mushroom EBG are the width of the patch *W*, the gap between adjacent patches *g*, the substrate thickness *h*, and the radius of the vias *r* [85]. As *W* increases, the center frequency and the in-phase bandwidth decreases. The gap g has the opposite effect compared with *W*. When g is increased, both the center frequency and bandwidth increase. Also, it is noted that increasing the substrate thickness h will decrease the center frequency but increase the in-phase bandwidth. The radius r has little effect on the center frequency and bandwidth. Here, *W* = 12 mm, *g* =1 mm, *h* = 12 mm, and *r* = 0.3 mm are selected. The mushroom-like EBG unit cell is simulated in HFSS using Floquet analysis and the reflection phase of the EBG structure is shown in Fig. 3.29(b). It is observed that the in-phase frequency range of the EBG structure is from 1.7 to 3.0 GHz.

.

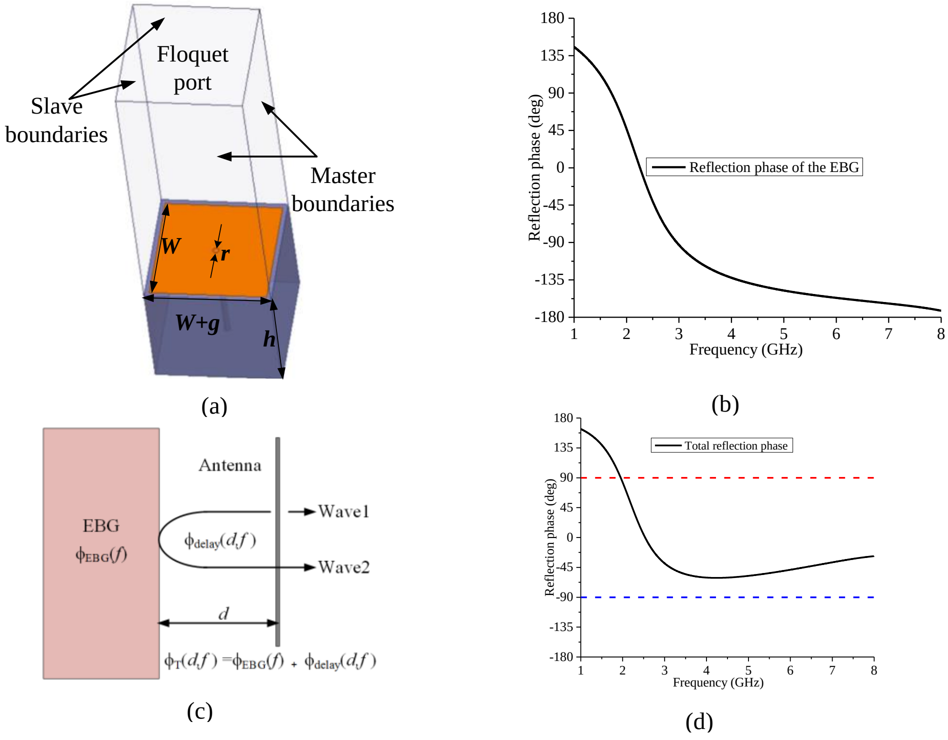

(a)

(b)

(c)

(d)

Figure 3.28: (a) Mushroom-like EBG unit cell with periodic boundary conditions; (b) Reflection phase of the EBG unit cell; (c) EBG- backed antenna and (d) Total reflection phase of the EBG-backed antenna.

When the EBG is placed underneath the antenna with a distance *d*, as a first order assumption, there is round-trip phase delay for the wave to go back and forth from the EBG surface as shown in Fig. 3.29(c). The phase delay is a function of the distance *d* and the frequency *f*, which can be estimated by equation 3.1. In the first order assumption, the total reflection phase of the backside wave is equal to the sum of the reflection phase of the EBG surface and the round-trip phase delay. Therefore, by placing the EBG surface below the antenna, the total reflection phase can not only be adjusted by the distance *d*, but also by the dimensions of the EBG surface. In order to reduce the back-side radiation of the dual-band fractal-shaped reconfigurable slot-ring antenna/array shown in Fig. 3.1, a total in-phase frequency range from 2.0 to 8.0 GHz is achieved as shown in Fig. 2(d) with *d* = 7. 5 mm. By further modifying the distance *d* and the dimensions of the EBG unit cell, a total in-phase frequency range from 2.0 to 12.0 GHz can be realized, which is presented in Fig. 3.30.

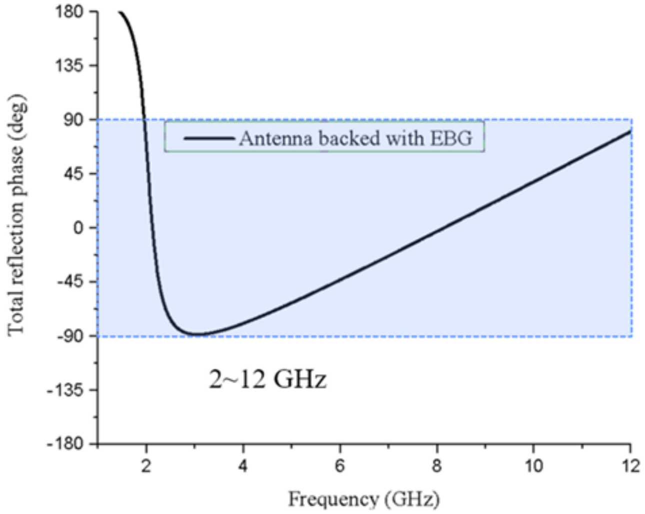

Figure 3.29: Total reflection phase of the EBG-backed antenna at d = 9 mm

The EBG-backed reconfigurable dual-band slot-ring antenna is simulated in HFSS; when the switches loaded on the antenna are turned ON or OFF, two frequency bands are achieved as shown in Fig. 3.31. The lower band can cover from 2.0 to 3.7 GHz with a return loss better than 7.2 dB while the higher band covers from 4.9 to 8.4 GHz with a return loss better than 7.4 dB. When the EBG structure is placed underneath the reconfigurable dual-band slot-ring antenna, the bandwidth is slightly reduced. At the lower band, the bandwidth reduction is relatively small while at the higher band, this bandwidth reduction is about 1.0 GHz.

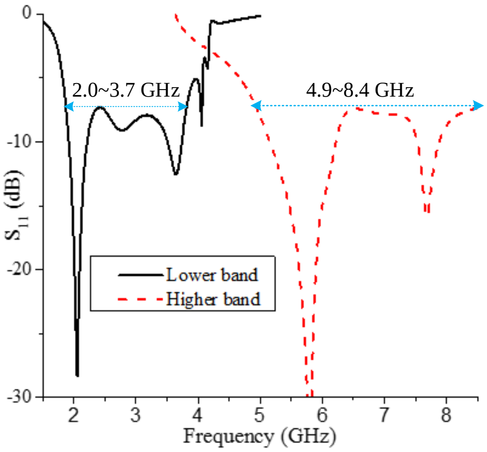

Figure 3.30: S_{11} of the EBG-backed reconfigurable dual-band slot-ring antenna at lower and higher bands.

Fig. 3.32(a) shows a top view of the fabricated EBG-backed fractal-shaped antenna and Fig. 3.32(b) shows a side view of the EBG-backed antenna. As shown in the figures, the fractal-shaped antenna is placed 7.5mm above the EBG surface. The EBG structure is fabricated on a 13-mm-thick Rogers 5880 substrate; four 125-mil-thick Rogers 5880 substrates are bonded together to achieve this thickness. The measured results of the EBG-backed antenna/array are presented in section 3.3.2 and 3.3.3.

(a) (b)

Figure 3.31: EBG-backed fractal shaped antenna: (a) top view; (b) side view.

3.3.2 S-band Measurement of the EBG-backed Fractal-Shaped Reconfigurable Slot-Ring Antenna/Array

The measured return losses of both H- and V-polarizations are shown in Fig. 3.33(a)-(b). The isolation between different ports is also measured as shown in Fig. 3.34(a)-(b). Both the measured return loss and isolation match well the simulated results. As shown in Fig. 3.33(a)-(b), when the switches are turned off, the return loss of the EBG-backed fractal antenna at S band is better than 5 dB from 1.8 to 3.6 GHz for both vertical and horizontal polarizations. At 2.5 GHz, S11 jumps up by about 2 dB due to the DC bias wire. The isolation between the horizontal and vertical polarizations (port 1 and port 2) at *S* band is better than 5dB as shown in Fig. 3.34(a). The isolation between the adjacent *S*-band and *C*-band ports (ports 1 and 3) when the switches are “OFF” is better than 10 dB as shown in Fig. 3.35(b).

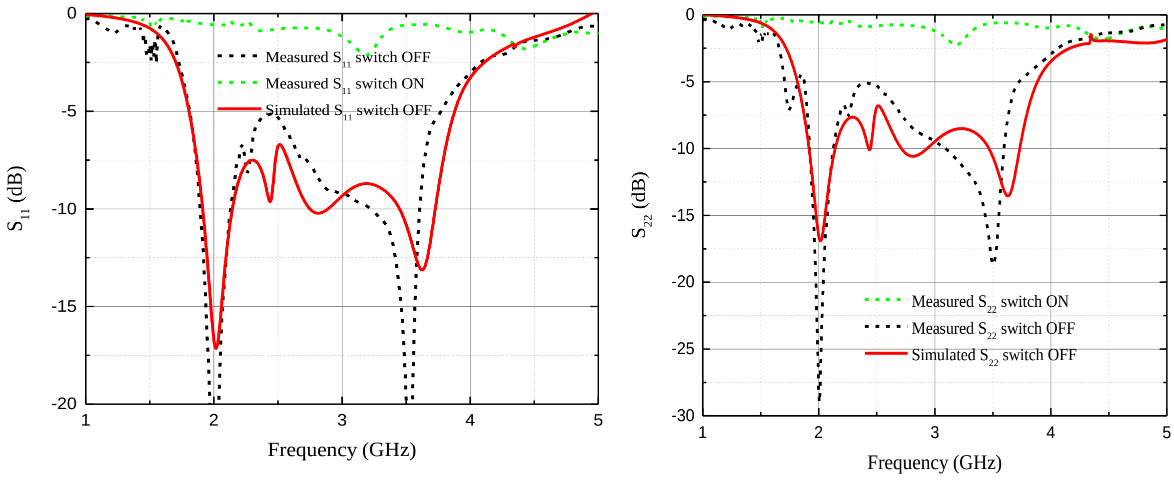

(a) (b)

Figure 3.32: Measured and simulated return loss of (a) V-pol. and (b) H-pol.

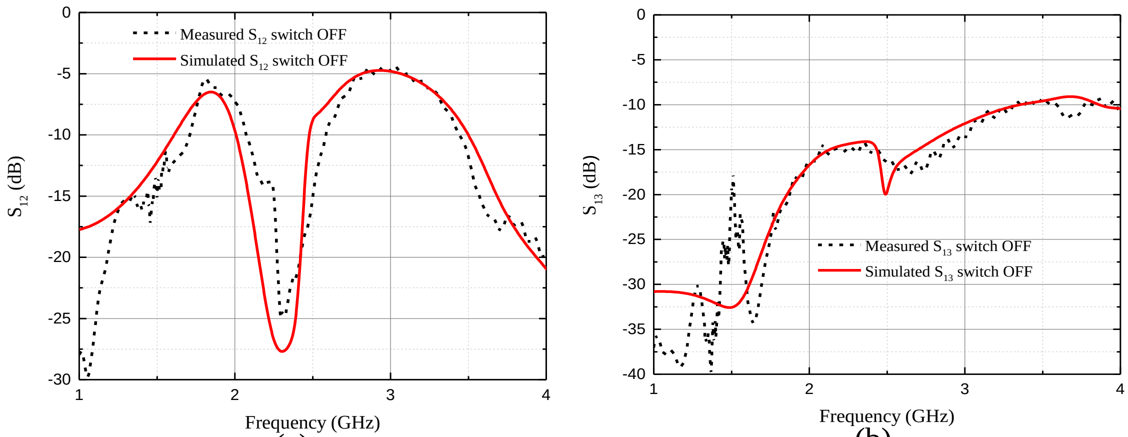

(a) (b)

Figure 3.33: Isolation between (a) H- and V-pol at *S* band (b) adjacent *S*-band *C*-band feeding lines.

The gain of the EBG-backed fractal-shaped antenna at *S* band is also measured. The measurement setup is shown in Fig. 3.35(a). The measured realized gain vs. frequency is shown in Fig. 3.35(b). The measured gain is about 2 dB less than the simulated gain from 2.0 to 2.5 GHz, which is due to the return loss, isolation, and radiation pattern. First, the simulated and measured return loss and isolation between port 1 and the other ports are compared. It is noted that the simulated total incident power to port 1 is about 0.53 dB higher than what the measurements show. In addition, the measured radiation pattern in the H-plane is broader than the simulated radiation pattern from 2.0 to 2.5 GHz while in the E-plane, the measured pattern is similar to the simulated pattern. The lower measured gain is due to a lower incident power and a lower measured directivity. A dip in the gain at 3.2 GHz in both simulation and measurements is observed. Further study shows that the dip is due to the splitting of the radiation pattern at 3.2 GHz. The gain at boresight is much less than the maximum gain at a tilted angle.

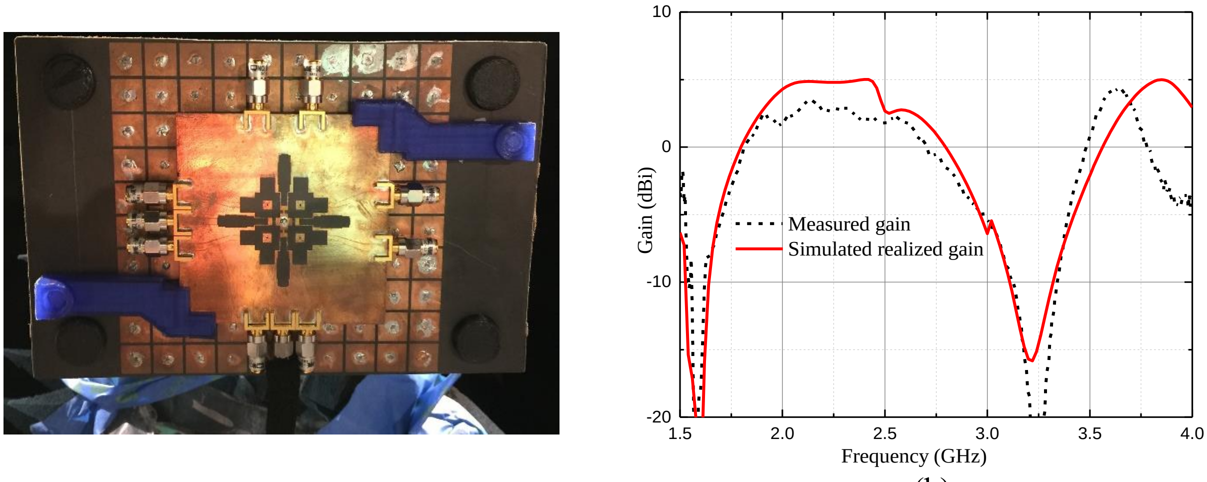

(a)

(b)

Figure 3.34: (a) Measurement setup of the EBG-backed fractal antenna at S band; (b) Measured and simulated gain vs frequency.

Measured Co-pol and X-pol radiation patterns in the E- and H-planes are compared to the simulations at three different frequency points in Fig. 3.36. Good agreement between the simulated and measured radiation patterns in the E-plane is observed. The measured H-plane pattern is broader than the simulated pattern at 1.8 GHz, which causes a lower measured gain. At 2.7 and

3.5 GHz, the measured H-plane patterns are similar to the simulated ones. The cross-polarization level is about 7 dB, which will decrease significantly when the antenna is used in an array.

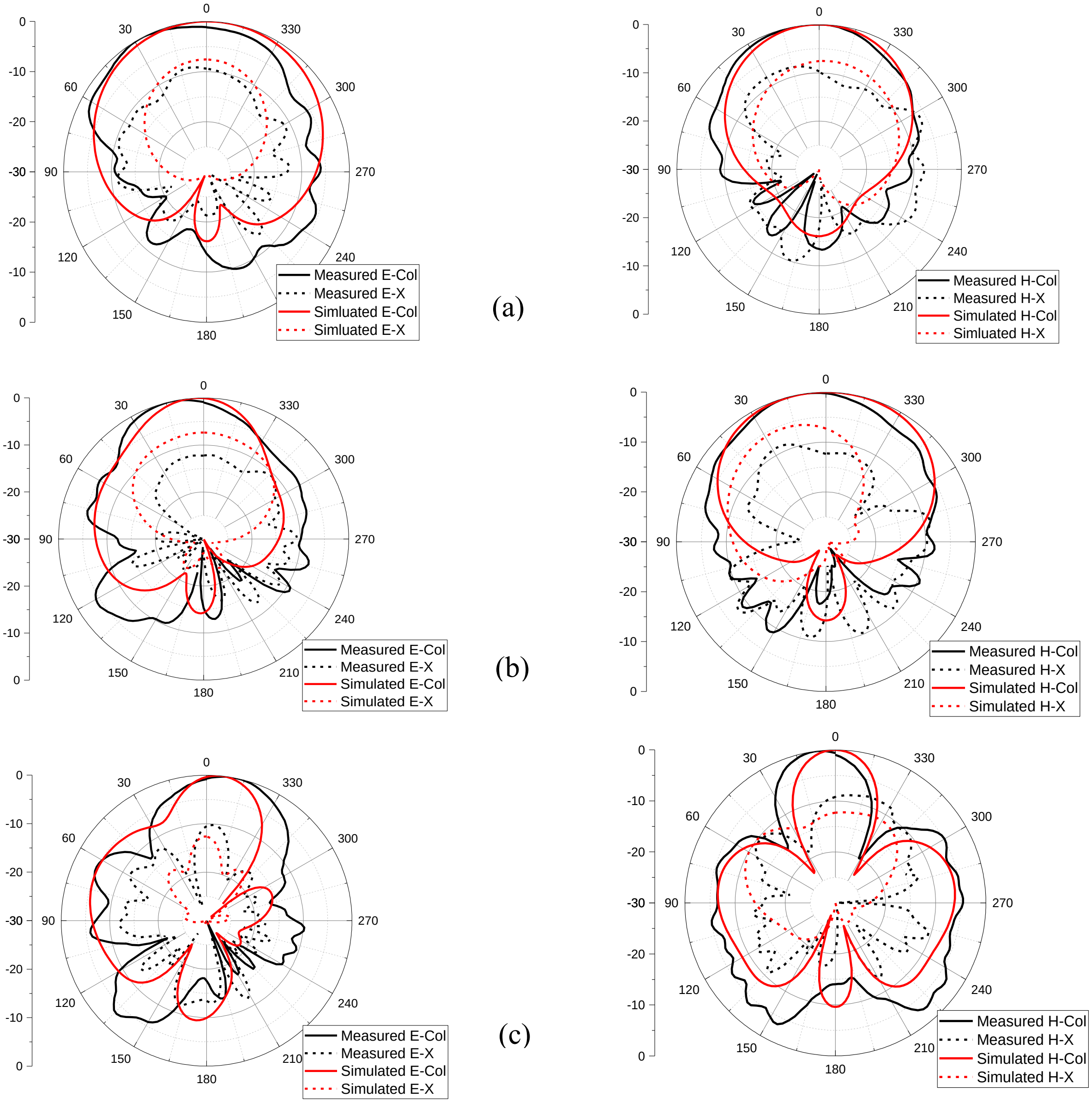

Figure 3.35: Radiation pattern at (a) 1.9 GHz; (b) 2.7 GHz; (c) 3.5 GHz.

3.3.3 C-band Measurement of the EBG-Backed Fractal-Shaped Reconfigurable Slot-Ring Antenna/Array

The measured return losses of both horizontal and vertical polarizations at *C* band are shown in Fig. 3.37(a)-(b). The measured return loss of the EBG-backed fractal antenna at *C* band is better than 8 dB from 4.9 to 8 GHz for both vertical and horizontal polarizations. The isolation between different ports is also measured as shown in Fig. 3.38(a)-(b). As shown in Fig. 24, the isolation between the H- and V-pol (ports 3 and 8) is only 3 dB because the two ports are very close to each other. The isolation between the adjacent *S*- and *C*- band feeding lines (port 1 and 3) when the switches are “ON” is better than 10 dB.

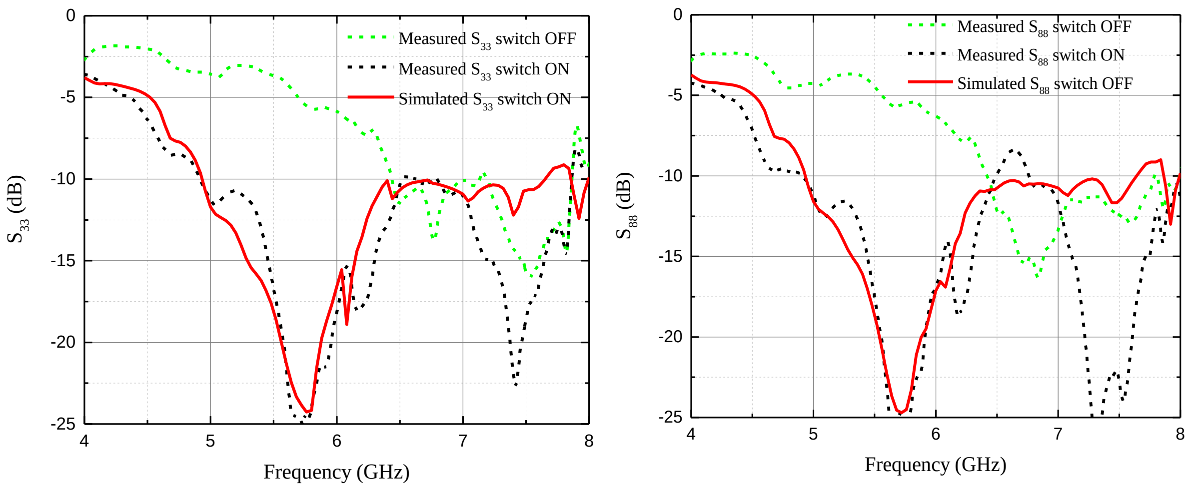

(a) (b)

Figure 3.36: Measured and simulated return loss of (a) vertical polarization; (b) horizontal.

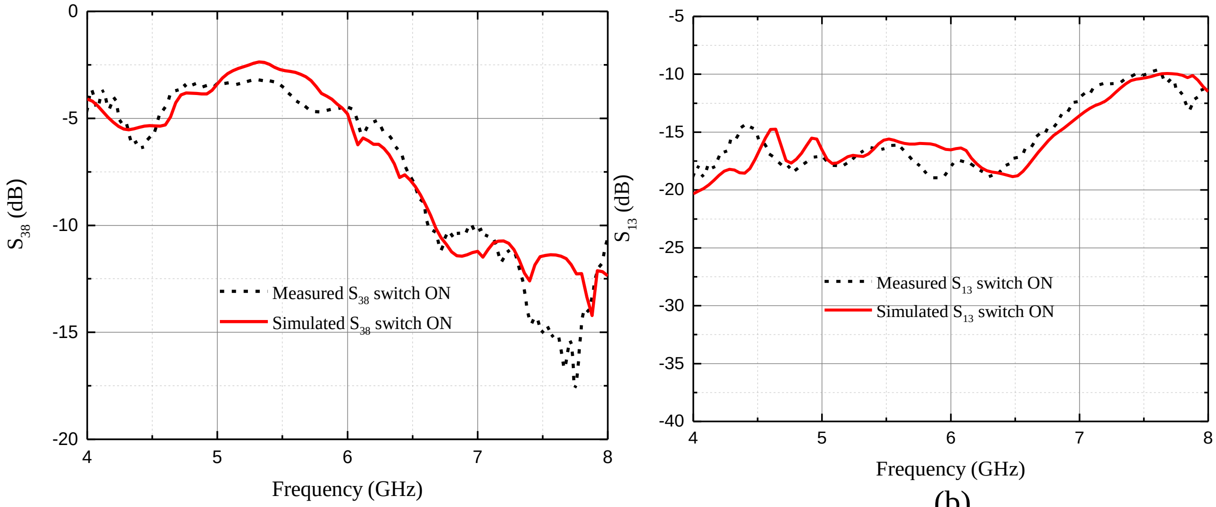

(a) (b)

Figure 3.37: Isolation between (c) Ports 3 and 8; (d) Ports 1 and 3.

The gain of the EBG-backed fractal-shaped antenna at *C* band is measured. The measurement setup is shown in Fig. 3.39(a). The measured realized gain vs. frequency is shown in Fig. 3.39(b). The measured gain vs. frequency has a similar trend to the simulated gain. However, there is a large difference between the simulated and measured gain at boresight due to the large discrepancies between simulated and measured radiation patterns as shown in Fig. 3.36. In both the simulations and measurements, the radiation patterns have dips/ peaks at the boresight which is caused by edge diffraction. Since edge diffraction of the antenna will be influenced by the cables and other objects in the surroundings in the measurements, the total effect on the measured radiation pattern are different from the simulations. Therefore, there a discrepancy between the measured and simulated radiation patterns which results in the difference between measured and simulated boresight gain. To take 4.5 GHz as an example, the radiation pattern at 4.5 GHz is shown in Fig. 26. The simulated radiation pattern at 4.5 GHz has a dip at boresight while the measured pattern has a peak at boresight. In this case, the measured gain at 4.5 GHz is much larger than the simulated gain. When pattern absorbers are put on the edge of the antenna, it will improve the radiation pattern a little bit, however, the boresight gain is also reduced by about 1 to 2 dB.

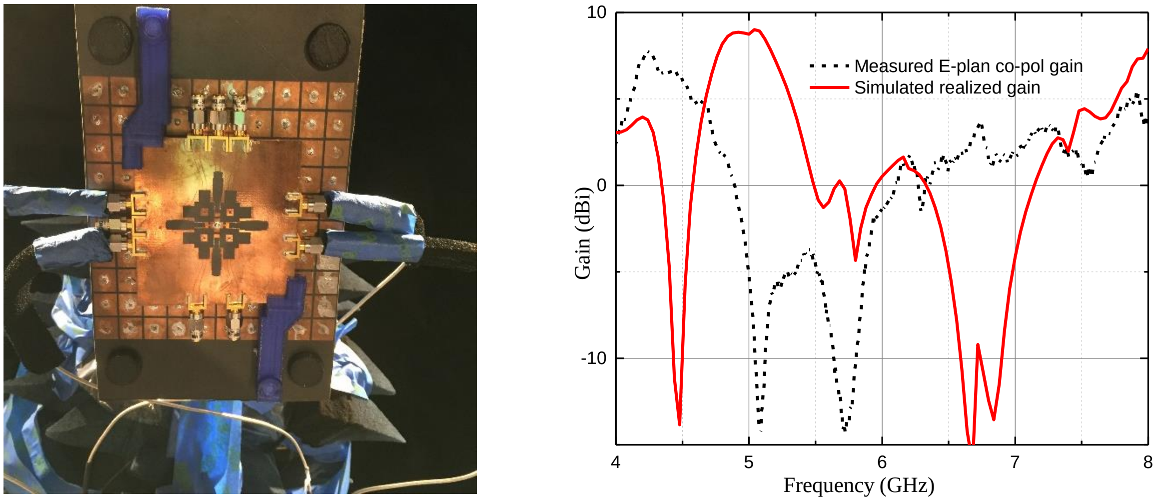

(a) (b)

Figure 3.38: (a) Measurement setup of the EBG-backed fractal antenna at C band; (b) Measured and simulated gain vs. frequency.

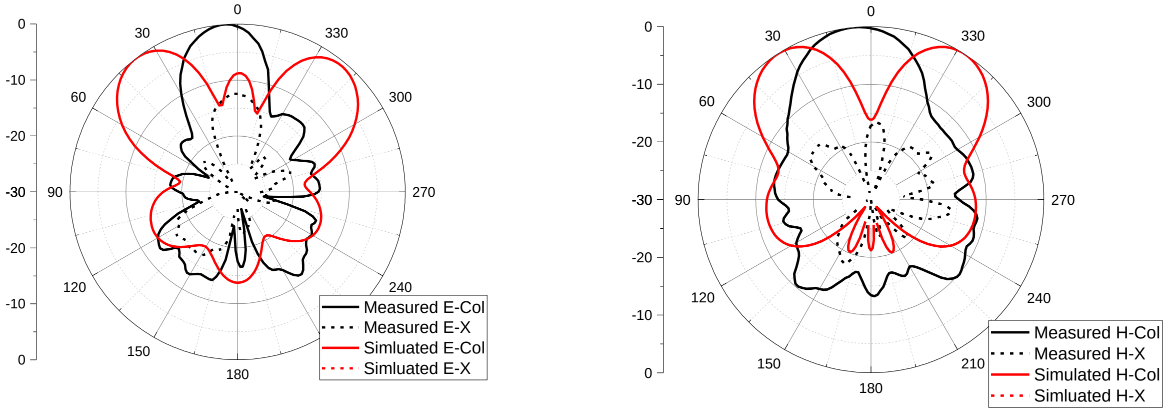

(a)

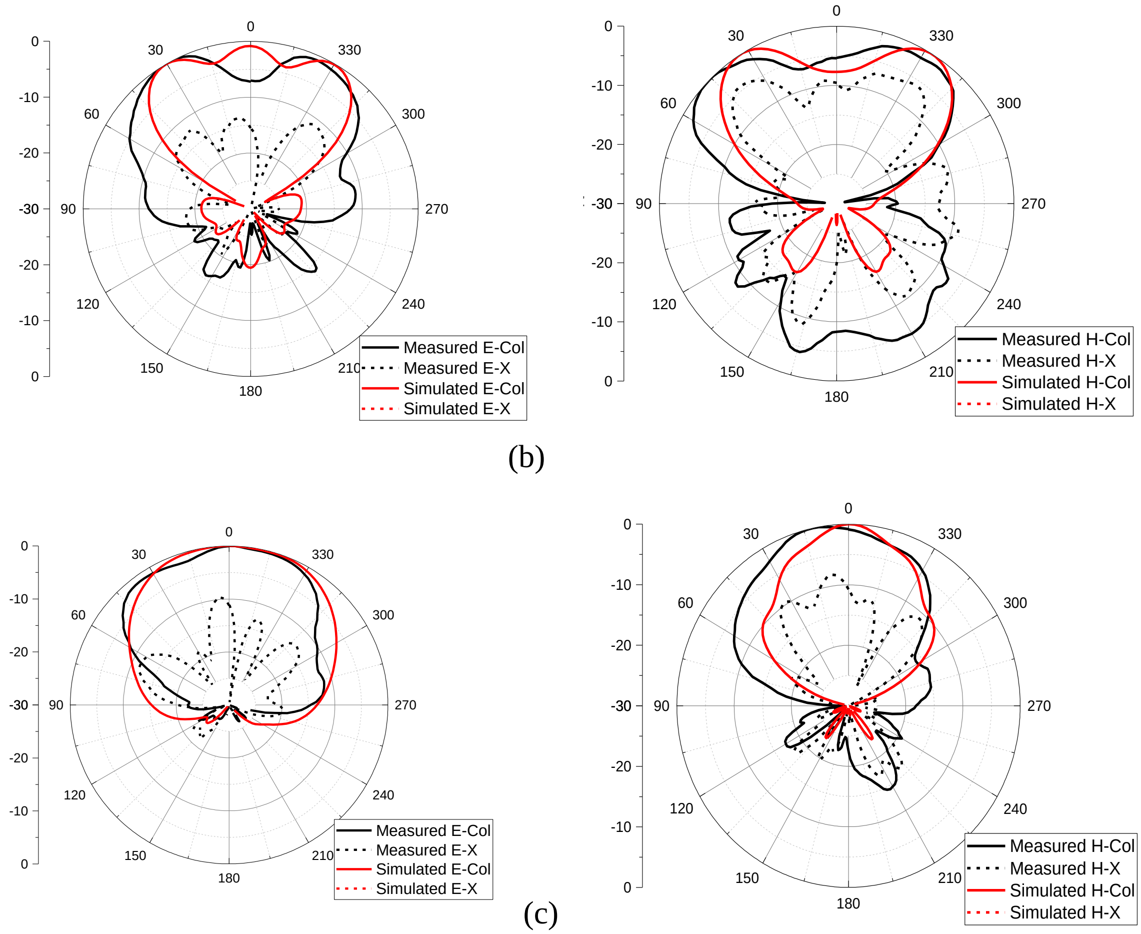

(b)

(c)

Figure 3.39: Radiation pattern at (a): 4.5 GHz; (b) 6.3 GHz; (c) 8 GHz;

The Co-pol and X-pol measured radiation patterns in he E-plane and H-plane are compared to the simulations at three different frequency points in Fig. 3.40. It is noted that at *C* band, the cross-polarization level is lower than 10 dB. However, larger discrepancies between simulated and measured radiation patterns at *C* band are observed.

3.4 Conclusion

By introducing fractal-shaped stubs and increasing the width of the slot-ring, an enhanced bandwidth of the reconfigurable slot-ring antenna is achieved. Moreover, since the fractal-shaped slot-ring antenna/array can cover almost the entire *S*-band (*C*-band) with switches 'OFF' ('ON'), no varactors are needed. The fractal-shaped slot-ring antenna/array is simulated, fabricated, and measured. When the switches are off, an octave bandwidth from 1.8 to 3.6 GHz with a return loss better than 7.5 dB is measured. When the switches are on, a 2×2 slot-ring antenna/array is formed. The return loss of the antenna/array element is better than 10 dB from 5.1 to 8 GHz.

Two ground plane solutions are presented in this chapter to reduce the backside radiation of the fractal-shaped reconfigurable dual-band slot-ring antenna/array. A metal plane that is placed 7.5mm away from the slot-ring antenna/array can cover a total in-phase frequency range from 2 to 8 GHz while a well-designed EBG surface has the potential of covering 2 to 12 GHz. Both the metal- and EBG-backed fractal-shaped reconfigurable slot-ring antenna/arrays are fabricated and measured. Both methods provide single-side radiation of the fractal-shaped slot-ring antenna/array operating in *S*- and *C*-band, respectively. It is observed that when the antenna is backed with the EBG surface/metal plane, there is a bandwidth reduction due to the near field interaction. In addition, due to edge diffraction effects, the radiation patterns of the EBG- and metal-backed antenna/array vary with frequency, especially at the *C*-band operation mode. Therefore, a co-design of the EBG surface/metal plane and the antenna is needed to get a better impedance match throughout both of the operation bands.

CHAPTER 4 USING INTEGRATED FILTER/PATCH ANTENNAS TO ACHIEVE WIDE-SCAN-ANGLE PHASED ARRAYS WITH ENHANCED BANDWIDTH

For microstrip patch phased arrays, a large fractional bandwidth (FBW) and a wide scan angle are challenging to achieve at the same time. Phased arrays on thin substrates can typically scan across large angles due to the reduction of mutual coupling caused by surface waves; however, thin substrates limit the achievable FBW of the phased array antenna.

In this chapter, an integrated filter/patch technology is proposed to realize phased arrays with large scan angle capabilities and enhanced bandwidth. In addition, this integrated filter/patch is able to provide filtering functionality, which is desirable for RF front ends.

4.1 Introduction of Patch Antenna Phased Arrays

Patch antenna phased arrays are widely used in radar and communication systems, owing to their beamsteering capability, low profile, light weight and ease of fabrication. For patch antenna phased arrays the spacing between the array elements needs to be close to half wavelength in order to avoid grating lobes at large scan angles. This close spacing will render strong mutual coupling between array elements, which causes significant impedance mismatch at large scan angles or even scan blindness which is defined as when the active reflection coefficient is unity [86]. On the other hand, many applications require a wide bandwidth, demanding the use of thick substrates and as a result leading to surface wave excitation and additional mutual coupling [87]. Therefore, phased arrays that can achieve a wide scan angle and possess a large bandwidth are intrinsically difficult to design.

Several techniques were proposed to suppress the surface wave propagation in thick substrates such as electromagnetic bandgap (EBG) structures [87], defected ground structures (DGS) [88], grooving the dielectric [89] and others. However, the aforementioned techniques usually require bulky sizes, complex designs, or expensive manufacturing processes.

Here, a new solution to reduce the mutual coupling within phased arrays, achieve wide scan angles, and provide enhanced bandwidth is proposed. The co-designed 2nd-order filter/antenna formed by a patch antenna and a cavity resonator is used as the array element. Since the FBW of the filter/patch system is much larger than a probe-fed patch antenna on a substrate of the same thickness [77], the filter/patch phased array is able to provide the same bandwidth as that of a coax-fed patch phased array but on a much thinner substrate. The surface wave excitation and the amount of mutual coupling between antenna elements will be mitigated due to the reduction of the substrate thickness. Therefore, the filter/patch phased array will have a wider bandwidth and better active impedance matching performance at large scan angles than the equivalent coax-fed patch phased array. In addition, the integration of the filter and radiating element provides the phased array with both filtering and radiating functions simultaneously without needing 50-ohm connections which will improve the efficiency of the whole system.

4.2 Bandwidth Comparison between Filter/Patch and Coax-Fed Patch Antennas on Different Substrates

First, the array element, a 2nd-order filter/patch is designed at a center frequency of 5.96 GHz as shown in Fig. 4.1. The cavity is formed by closely spaced metallic vias in the substrate and functions as the first resonator. The patch antenna operates simultaneously as both the second resonator of the 2nd-order filter/antenna and the radiating element. The short-ended SMA connector provides the external coupling to the first cavity, while the coupling via provides the internal coupling between the first cavity and the patch antenna. 50-mil-thick Rogers RT/Duroid 6006 ($\varepsilon_r = 6.15; \tan\delta = 0.0027$) is used as the substrate for both the first cavity and patch antenna.

The filter/patch is synthesized to emulate a two-pole Chebyshev filter following the procedure in [77]. The dimensions of the filter/patch are listed in Fig. 4.2. A FBW of 5.6% is achieved and the gain of the filter/patch is 5.27 dBi at a center frequency of 5.96 GHz.

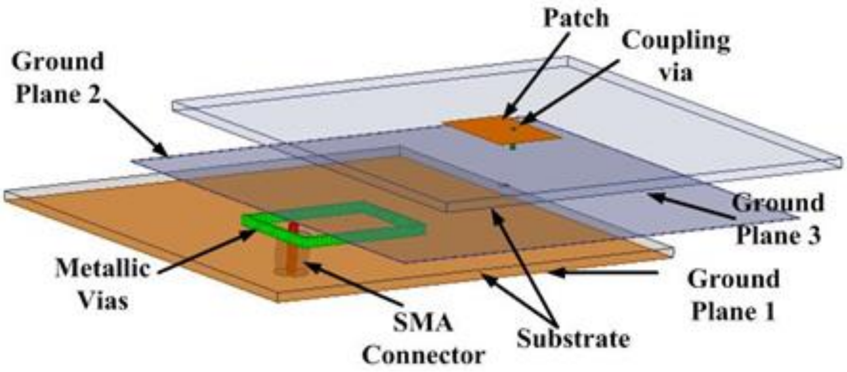

Figure 4.1: Exploded view of a 2nd-order filter/antenna comprised of one cavity resonator and one patch antenna.

Coax-fed patch antennas are fabricated on substrates of different commercially available substrate thicknesses for FBW comparison. The thicknesses used are 50 mil (1.27 mm), 75 mil (1.905 mm), and 100 mil (2.54 mm) on RT/Duroid 6006 . From the High Frequency Structure Simulator (HFSS) simulations, the FBW of the filter/patch on a 50- mil-thick substrate and of the coax-fed patch antennas on 50-, 75-, and 100-mil-thick substrates is 5.6%, 2.5%, 4.2%, and 6.8%, respectively. It is noted that the filter/patch antenna exhibits a much wider FBW compared with a coax-fed patch antenna on a substrate with the same thickness (50 mil) or even slightly thicker (75 mil). Though the coax-fed patch antenna on the 100-mil-thick substrate achieves a wider FBW, as will be shown in Section IV, a phased array using this antenna has very bad active impedance performance at large scan angles due to the excitation of strong surface waves inside the thick substrate.

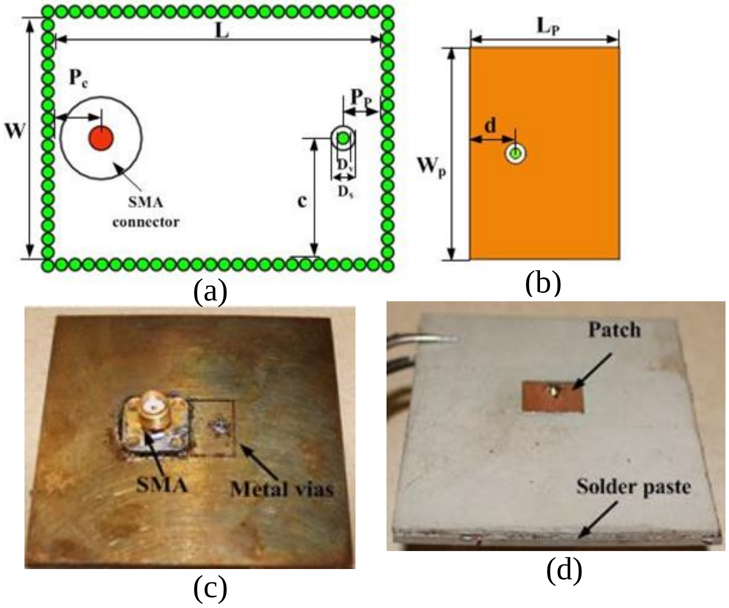

(a) (b)

(c) (d)

Figure 4.2: Schematics of (a) cavity resonator with coaxial feeding and coupling via; (b) patch antenna and coupling via; (c) backside of the fabricated filter/antenna; (d) front side of the fabricated filter/antenna. (W=12.60, L=17.40, Pc=2.50, Pp=2.05, Dv=0.635, Ds=1.27, c=6.3, Wp=13, Lp=9.3, d=2.85) Dimensions are in mm.

4.3 Fabrication and Measurement Results

The 2nd-order filter/patch, and the coax-fed patch antennas on 75- and 100-mil-thick substrates are fabricated by standard PCB fabrication processes and measured using a Vector Network Analyzer (VNA) and an anechoic chamber. As shown in Fig. 4.2(c)-(d), the first cavity of the filter/patch and the patch antenna are separately fabricated and then bonded together using solder paste inside a reflow oven. The reflection coefficients and gain versus frequency for filter/antenna and patch antennas on 75- and 100-mil-thick substrates are presented in Fig. 4.3. It is observed that the FBW of three cases is 5.5%, 4.3%, and 6.4%, respectively. The measured FBW is very close to the design values described in Section II. In addition, a 2nd-order filtering response is apparent for the filter/patch case as shown in Fig. 4.3(a). As a comparison, the gain for coax-fed patch antennas is quite flat versus frequency, without any filtering behavior. By taking the ratio of measured gain and simulated directivity in HFSS, it is found that the overall efficiency of the filter/patch system is 84%, which is equivalent to a 0.78-dB loss. Similar to the study in [77], we found that this loss is completely due to the 2nd-order filter insertion loss and not from the patch antenna radiation efficiency. The measured center frequency, FBW, and gain of all three cases are listed in Table 4.1. It is observed that the filter/patch has the highest gain among all three cases. Finally, the radiation patterns in both the E- and H-planes for all three cases are measured and compared in Fig. 4.4. As expected, the radiation patterns of all three cases are very similar because the radiating element is same. In addition, the measured and simulated radiation patterns for the filter/patch are in close agreement.

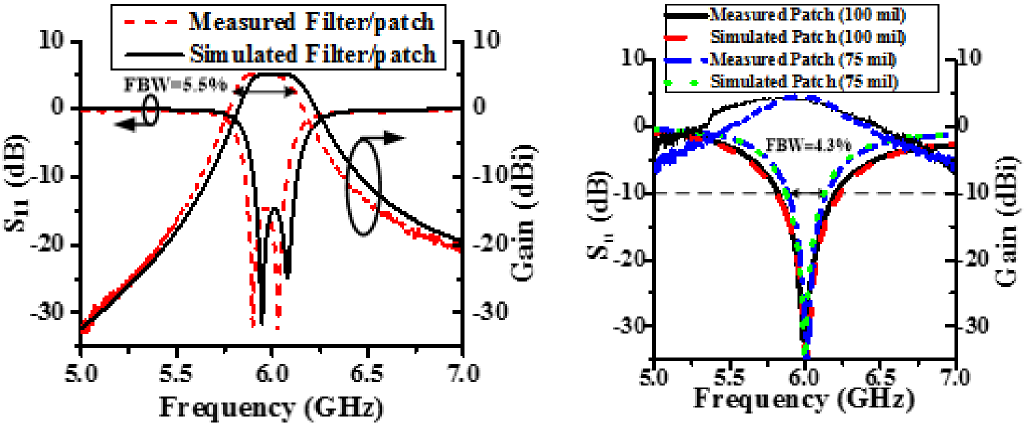

(a)

(b)

Figure 4.3: Simulated and measured results of (a) 2nd-order filter/antenna; (b) patch antennas on 75- and 100-mil-thick substrates, respectively.

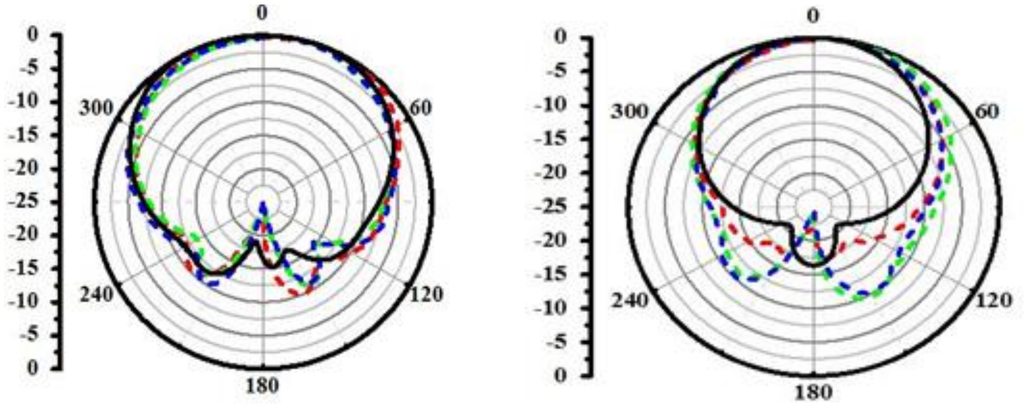

(a)

(b)

Figure 4.4: Simulated and measured radiation patterns of the 2^{nd}-order filter/antenna and standalone patch antennas in (a) E plane and (b) H plane at the center frequency.

Table 4.1: Comparison of FBW and Gain for Filter/Antenna and Patch Antennas

Antenna type	Substrate thickness (mil)	Center frequency (GHz)	Fractional bandwidth (FBW)	Gain (dBi)
Filter/patch	50	5.89	5.5%	5.28
Coax-fed patch	75	6.00	4.3%	4.63
	100	6.01	6.4%	4.43

4.4 Floquet Analysis

Four infinite phased arrays using 2nd-order filter/patch, coax-fed patch antennas on 50-, 75- and 100-mil-thick substrates as array elements are investigated using full-wave Floquet analysis in HFSS. By assigning the Floquet port and master/slave boundaries, Floquet TE and TM modes are excited and the active reflection coefficient can be found from the S Matrix interrelating the wave modes and Floquet modes [90].

The spacing between array elements for all cases is set to $0.5\lambda_0$ at 6 GHz, which guarantees no grating lobes at large scan angles. Fig. 4.5 compares the active reflection coefficients versus different scan angles in the E plane for all cases. If we use -10 dB as the cutoff level for the active reflection coefficient, the maximum acceptable scan angles for phased arrays using filter/patch, coax-fed patch antennas on 50-, 75-, and 100-mil-thick substrates are 50°, 49°, 44°, and 37°, respectively. As mentioned earlier, the patch and filter/patch phased arrays on 50-mil-thick substrate have similar maximum acceptable scan angles (49° vs. 50°) but the FBW is very different

(2.5% vs. 5.5%). It is also noted that when the scan angle is larger than 40⁰, the active reflection coefficient is the lowest for the filter/patch phased array.

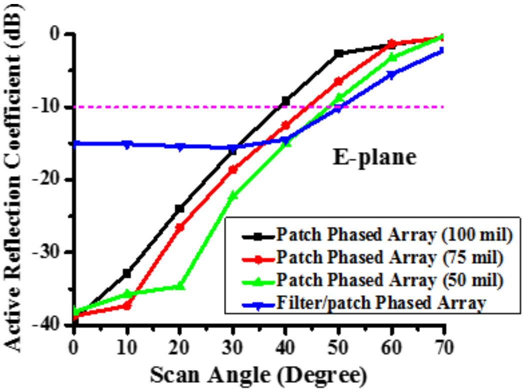

Figure 4.5: Active reflection coefficients vs. scan angles in E plane for four types of phased arrays.

It is also illustrative to present the 2nd-order filter/antenna phased array active reflection coefficient and transmission coefficient of Floquet TM_{00} versus frequency for different scan angles. Floquet TM_{00} mode is the major mode in the E plane. The transmission coefficient of the Floquet TM_{00} mode in the E plane is defined as the ratio between the power transmitted to the Floquet port and the power incident into the coax feed. The 2nd-order filtering function is apparent in Fig. 4.6. The transmission coefficient is -0.88 dB at boresight due to the filter loss. When the scan angle increases from 0 to 50°, the active reflection efficient becomes progressively worse. However, the return loss is better than 10 dB across the scan angle range, which closely matches the prediction in Fig. 4.6.

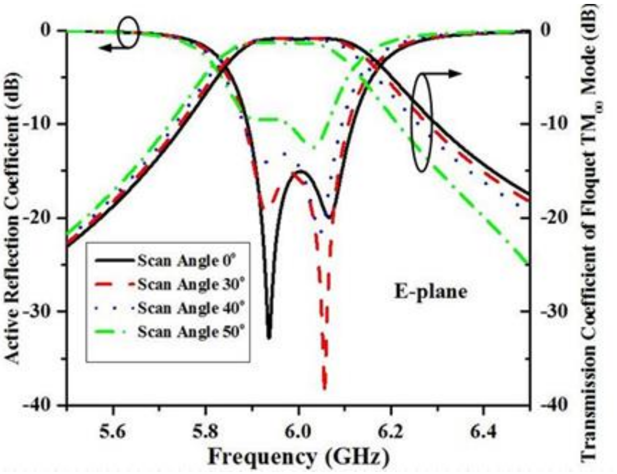

Figure 4.6: Active reflection coefficients and transmission coefficients of the Floquet TM$_{00}$ mode in E plane for the filter/patch phased array at different scan angles.

4.5 Conclusion

A filter/patch phased array with wide scan angle performance (50°) and enhanced FBW (5.5%) is proved using Floquet-mode analysis. A 2nd-order filter/patch unit cell consisting of one cavity resonator and one resonant patch is designed, fabricated and measured to demonstrate the concept. Coax-fed patch antennas on substrates with different thicknesses are also measured for comparison. The filter/patch is able to achieve the same FBW but on a thinner substrate, which helps reduce mutual coupling and enable a wide scanning range in phased array applications.

CHAPTER 5 INTEGRATED CIRCULARLY POLARIZED FILTER/PATCH ANTENNA ARRAYS

In chapter 4, a linearly polarized (LP) integrated filter/patch antenna was designed, fabricated, and measured for the purpose of bandwidth enhancement of the phased patch antenna array. It was shown that when integrating a LP patch antenna with cavity resonators, a larger bandwidth compared with that of the standalone LP patch antenna is achieved. The cavity resonators coupled to the LP patch antenna can be intuited as a multi-section impedance transformer which works as a broadband feeding network for the LP patch antenna.

On the other hand, singly-fed circularly polarized (CP) patch antennas are very popular in many applications due to their compact size and ease of design but are limited by an inherently narrow bandwidth. The typical operational bandwidth of a probe-fed CP patch antenna is 1~2% since the antenna requires both impedance matching and an acceptable axial ratio over the frequency band. Generally, thick substrates along with other techniques are used to achieve a broadband CP patch antenna with a single feed; however, thick substrates may cause issues such as surface wave excitation, mutual coupling, and low efficiency.

In this chapter, A technique to enhance the impedance-AR bandwidth of the probe-fed corner-truncated patch antenna using filter/patch antenna integration without using thick substrates is presented. By integrating the CP patch antenna with cavity filters and sequentially rotating the CP filter/patch antenna element to form a 2×2 array, an impedance-AR bandwidth of 8.3% is achieved with a 0.0292-λ_0-thick antenna layer. In addition, a 3rd-order Chebyshev filtering function is preserved over the operational band.

5.1 Introduction of the Integrated CP Filter/Patch Antenna/Array

In many applications such as global navigation satellite communication systems, radio frequency identification, mobile communications, and wireless local personal networks, CP antennas that can reduce multipath interference are preferred over LP antennas. The dual-feed CP patch antenna usually has a decent bandwidth but the feeding networks are bulky. Singly-fed CP patch antennas, such as corner-truncated patches, are widely used because of the ease of fabrication and simplicity of design; however, one of the challenges in designing the single-feed CP patch antenna is the narrow bandwidth. Increasing the substrate thickness is the most common bandwidth-enhancement technique for LP antennas but is not as effective for CP antennas. The working band of a well-designed CP antenna is the overlap of the acceptable S_{11} ($\leq$-10 dB) and axial-ratio ($\leq$ 3 dB) bands and it was reported in [91] that the overlap of the S_{11} and axial-ratio bands is inversely proportional to increasing substrate thickness. The authors in [92] introduced a capacitive element in series with the probe inductance to further increase the S_{11} and axial ratio band overlap. A single probe-fed truncated corner CP patch on a thick foam (0.16 λ_0) with an AR-S_{11} bandwidth of 12.6% was achieved in [92]. In this case, the S_{11}-AR bandwidth of the CP patch was enhanced at the expense of surface wave excitation, increased cross polarization and decreased antenna efficiency.

In this chapter, we demonstrate a new methodology to increase the AR-S_{11} bandwidth of a corner-truncated CP patch antenna without increasing substrate thickness. First, by integrating the CP patch antenna with a cavity filter, the impedance bandwidth can be enhanced. A sequentially rotated array configuration is then employed to enlarge the AR bandwidth. In this way, a sequentially rotated 2×2 CP filter/patch array with an enhanced AR-S_{11} bandwidth is achieved on a thin substrate.

In the literature, there are only several works concerning integrating filters with CP patch antenna. A dual-feed CP filtering antenna was reported in [68]; the authors used two planar bandpass filters (BPF) to orthogonally feed two LP patch antennas and provide a 90º phase difference between them in order to achieve the CP performance. However, the two LP antenna antennas were not well-designed as additional resonators of the BPFs according to the filtering responses and the substrate thickness of the antenna layer is relatively thick (0.049 λ_0). Moreover, the quality factor Q is limited due to the planar structure and as a result, radiation efficiency of the design in [68] is only 80%. A singly-fed CP patch integrated with a high-Q filter was presented in [66], but the reported AR-S_{11} bandwidth is only about 1.5% which is mainly limited by the AR bandwidth. This paper extends the work in [93] and increases the AR-S_{11} bandwidth to 8.3% with an antenna layer substrate thickness the same as that reported in [93]. Moreover, the simulated Q-factor of the cavity filter is about 680, the simulated overall efficiency of the CP filter/patch array is 91%, and the efficiency of the antenna is even higher.

5.2 Integration of High-Q Filters with Singly-Fed Circularly Polarized Patch Antennas

First, a 3rd-order CP filter/patch is designed as an array element. Fig. 5.1 shows an exploded view of the high-Q filter integrated with a singly-fed circularly polarized patch antenna. The structure consists of three stacked layers consisting of two cavity layers and one antenna layer. Fig. 5.1 shows the device with the dielectric material omitted for a better view. It can be seen that the cavity resonators are formed by closely-spaced metallic vias with a diameter of 0.41mm. The spacing between each via, 0.71 mm, is much smaller than the wavelength at the operating frequency to prevent energy leaking from the sidewall [94]. The external coupling from the input to the first resonator is realized through a short-ended 50-Ω SMA connector while the internal coupling between the first and second cavity is realized by a slot in the ground plane between the two cavities. A coupling via with a diameter of 25 mil is used to provide the internal coupling between the second cavity resonator and the CP patch antenna. The CP patch antenna behaves as a third resonator and as a result, a third-order Chebyshev filtering response can be obtained from the two resonators and the CP patch antenna if a rigorous synthesis procedure is followed to achieve the correct external couplings, internal couplings, and resonant frequencies. Moreover, the coupling via between the second resonator and the corner truncated patch antenna excites two degenerate resonant modes of the corner-truncated patch with the same magnitude and a 90°phase difference at the center frequency. In this design, a right-hand (RH) CP radiated wave is generated. Thus, the device shown in Fig. 5.1 performs both a third-order filtering function and radiates an RHCP wave.

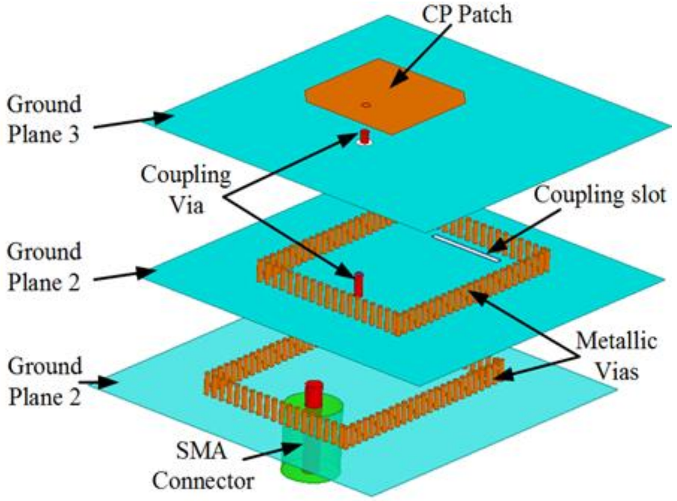

Figure 5.1: Exploded view of a third-order filter/antenna comprised of two cavities and a single-fed circularly polarized patch antenna.

The top view of each layer of the 3^{rd}-order CP filter/patch is illustrated in Fig. 5.2(a)-(c) while the side view of the vertically stacked CP filter/patch is shown in Fig. 5.2(d). The dielectric substrates used for all the three layers is a Rogers RT/Duroid 5880 ($\varepsilon_r = 2.2$; $\tan\delta = 0.0009$) material with different thicknesses. A 12-µm thick soldering tin film is applied between each layer to bond the different layers together.   All the dimensions of the 3^{rd}-order CP filter/patch are listed in Fig. 5.2.

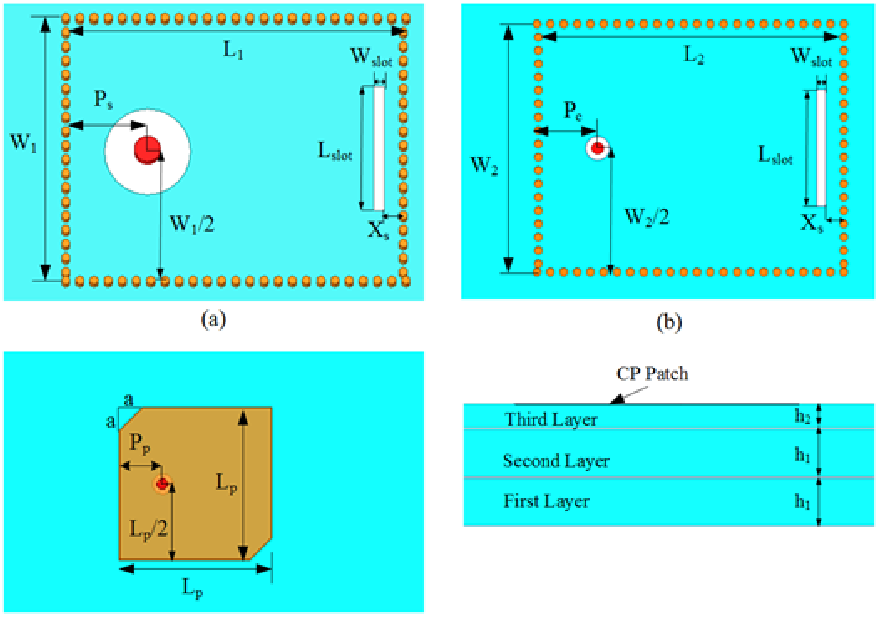

(a)

(b)

(c)

(d)

Figure 5.2: Schematics of the CP filter/patch. Top view of (a) First cavity resonator of the CP filter/patch including a SMA connector and a coupling slot; (b) Second cavity resonator of the CP filter/patch with a coupling via and slot and (c) corner-truncated CP patch with coupling vias. (d) Side view of the stacked CP filter/patch antenna. ($W_1 = 12.80$, $L_1 = 16.50$, $P_s = 3.90$, $W_{slot} = 0.50$, $L_{slot} = 6.20$, $X_s = 0.75$, $W_2 = 12.80$, $L_2 = 15.85$, $P_c = 2.95$, $L_p = 9.50$, a = 1.40, $\mathrm{P_p} = 2.65$, $\mathrm{h_1} = 1.58$, $\mathrm{h_2} = 0.79$, all in millimeters.

In order to synthesize the integrated CP filter/patch antenna, a 3-pole Chebyshev filter is designed at X-band ($f_0 = 10.22$ GHz) with the following parameters as a reference:

$$k_{12} = k_{23} = 0.068 \tag{5.1}$$

$$Q_{ext1} = Q_{ext2} = 13.0 \tag{5.2}$$

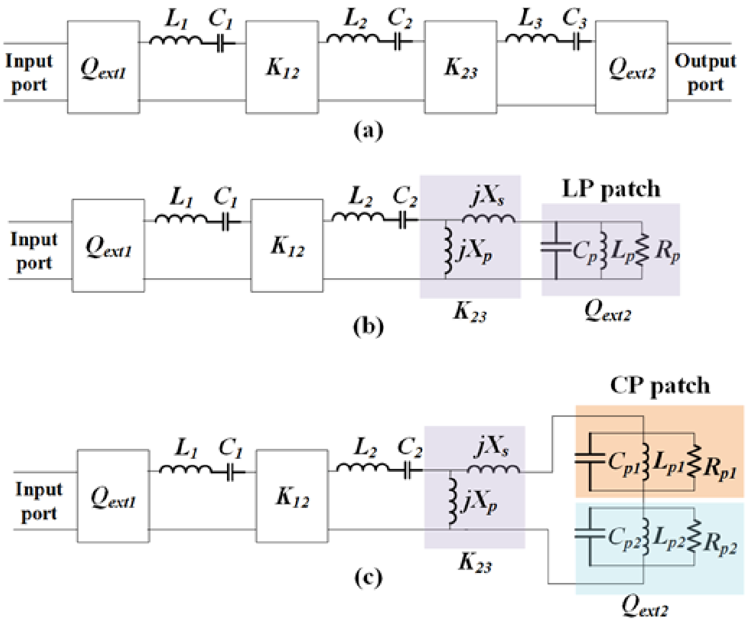

Figure 5.3: Equivalent circuit model of (a) reference filter, (b) integrated filter with LP patch antenna, (c) integrated filter with CP patch antenna

Fig. 5.3(a) shows the equivalent circuit model of the reference filter. The structure of the reference filter is symmetric about the middle of the second cavity. The last resonator of the reference filter is identical to the first cavity resonator to ensure $Q_{ext1} = Q_{ext2}$. Unlike the reference filter, the structure of the integrated filter with the antenna is asymmetric since the last resonator is replaced by the antenna and the internal coupling is provided by the coupling via instead of the coupling slot as shown in Fig. 5.3(b)-(c). Therefore, in order to get the same filtering response as the reference filter, the internal coupling k_{23} and the external coupling Q_{ext2} have to be carefully designed. In the integration of the filters with LP patch antennas, the external coupling Q_{ext2} is achieved by the radiation Q of the patch antenna [77]. Probe-fed LP patch antennas can be modeled as an inductor representing the probe in series with a parallel RLC circuit [4], as shown in Fig. 5.3 (b). The radiation Q of the LP patch antenna is calculated by:

$$Q_{rad} = 2\pi f_0 R_p C_p = \frac{R_p}{2\pi f_0 L_p} \tag{5.3}$$

if the dielectric, metallic, and surface wave losses are neglected [4]. However, since the probe-fed corner truncated patch antenna radiates two orthogonal modes with different resonant frequencies simultaneously, extracting the radiation Q of the antenna is a challenge. In addition, the coupling via between the second resonator and the patch antenna must not only match the internal coupling k_{23} with the same value as k_{12} but also needs to maintain the two orthogonal modes with an equal magnitude and a quadrature phase to ensure CP radiation of the antenna. Therefore, in the following discussion, we will demonstrate how to calculate the radiation Q of the CP patch antenna and provide the step-by-step design procedure of how to achieve the same filtering response of the reference filter with two cavity resonators and a corner truncated patch antenna.

5.2.1 Modeling of the Probe-Fed Corner Truncated CP Patch Antenna

One of the most popular ways to produce CP waves with a singly-fed patch antenna is to use a perturbation configuration. By slightly perturbing a square patch and feeding at the appropriate locations, two orthogonal modes can be excited. Fig. 5.4 shows a corner truncated square patch with a feeding probe. When the feeding probe is placed along either the x- or y- axis, two orthogonal modes (#1 & #2) along the direction of the two diagonals are excited. The size of the square patch Lp and the truncated corner need to meet the condition of:

$$\frac{a}{L_P}=\sqrt{\frac{1}{2Q_0}} \tag{5.4}$$

in which Q_0 is the unloaded Q of the square patch [69]. The distance of the feeding point to the edge of the patch P_p must be optimized in order to get good CP performance.

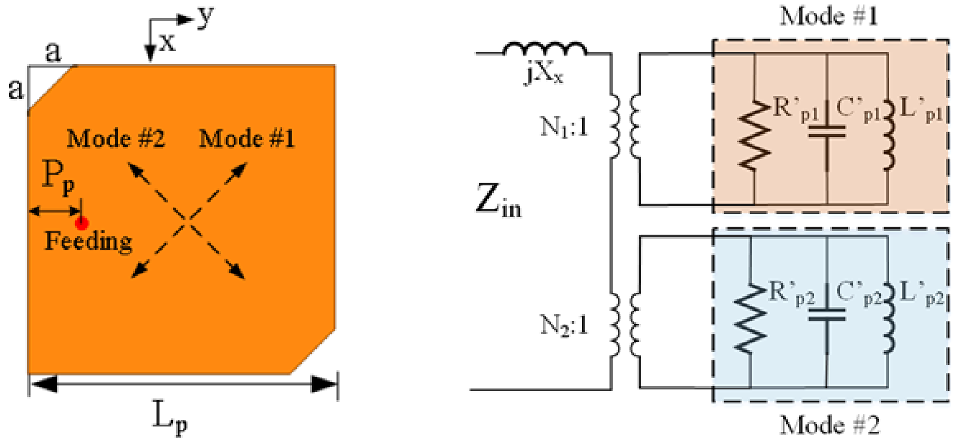

(a) (c)

Figure 5.4: Corner truncated square patch with a probe feed. (b) Circuit model of the corner truncated CP patch.

The equivalent circuit model of the probe-fed corner truncated CP patch antenna has been well developed [95]. Two parallel RLC circuits can be used to represent the two orthogonal modes with an inductor to model the probe as shown in Fig. 5.3(b). The turn ratios for the two orthogonal modes can be calculated by:

$$N_1=\sin\left(\frac{\pi x}{L_p}\right)\pm\sin\left(\frac{\pi y}{L_p}\right) \tag{5.4}$$

$$N_2=\sin\left(\frac{\pi x}{L_p}\right)-\sin\left(\frac{\pi y}{L_p}\right) \tag{5.5}$$

where (x,y) is the location of the feeding point if the center of the corner-truncated patch antenna is defined to be the origin of the coordinate system [95]-[96]. However, extracting the equivalent circuit element values (X_x, R'_{p1}, L'_{p1}, C'_{p1}, R'_{p2}, L'_{p2}, C'_{p2}) and calculating the radiation Q of a well-designed CP patch antenna have not been described in any existing papers to the best of the authors' knowledge. In addition, since the two parallel RLC circuits are coupled together producing two resonances at the same frequency, directly obtaining those equivalent circuit element values from the input impedance of the antenna is impossible.

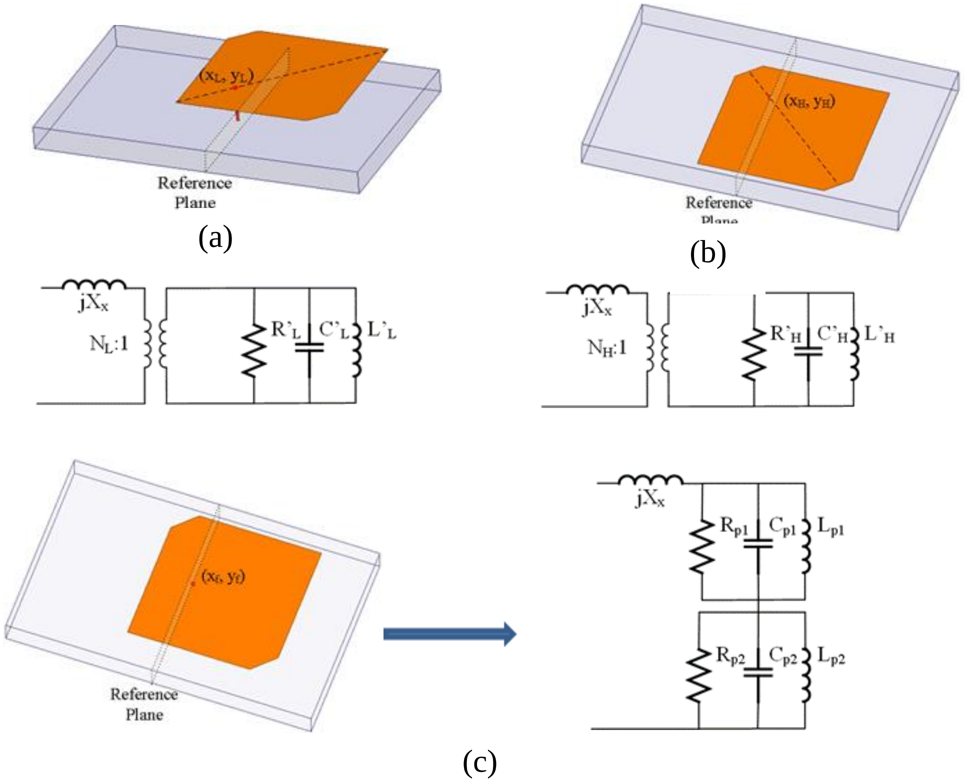

Figure 5.5: Waveguide coupled corner truncated square patch with coupling via located along (a) one of the diagonal direction to excite only mode #1; (b) the other one of the diagonal direction to excite only mode #2; (c) y-axis to excite both orthogonal modes.

Therefore, the first step to acquire the equivalent circuit element values of the probe-fed CP patch antenna is to excite the two orthogonal modes separately. Fig. 5.5(a) shows the CP patch coupled to a waveguide by a small coupling via located along one of the diagonal directions. Only mode #1 with a lower resonant frequency is excited in this case. When both waveguide ports are de-embedded to the reference plane as shown in Fig. 5.5 (a), the impedance of mode #1 reflected into the waveguide is extracted by the simulated impedance parameter Z_{12}. The center frequency f_L is located at the peak of Re{Z_{12}}, where Re{$Z_{12}(f_L)$} represents the resistance R_L. The series reactance jX_x is defined at Im{$Z_{12}(f_L)$}. As a result, the admittance of the parallel RLC can be extracted by:

$$Y_{mL} = \frac{1}{Z_{12} - jX_x} \tag{5.6}$$

The capacitance is obtained by the slope of the admittance versus frequency [97]:

$$C_L = \frac{1}{2}\frac{dY_{mL}}{d\omega}\Big|_{\omega=\omega_L} \tag{7}$$

Similarly, when the coupling via is fed along the other diagonal direction of the CP patch antenna as shown in Fig. 5.5 (b), the equivalent circuit element values (R_H, C_H, L_H) for the higher frequency mode #2 are obtained. When the coupling via is placed along the y-axis as shown in Fig. 5.6 and excites the two modes simultaneously, the equivalent circuit element values for the dual-parallel RLC circuit are given by:

$$R_{p1} = \left(\frac{N_1}{N_L}\right)^2, L_{p1} = \left(\frac{N_1}{N_L}\right)^2 \tag{5.8}$$

$$C_{p1} = \left(\frac{N_L}{N_1}\right)^2, R_{p2} = \left(\frac{N_2}{N_H}\right)^2 \tag{5.9}$$

$$L_{p1} = \left(\frac{N_2}{N_H}\right)^2, C_{p1} = \left(\frac{N_H}{N_2}\right)^2 \tag{5.10}$$

Where N_1, N_2, N_L, N_H can be calculated using equation (4)-(5). After tuning the resistances, the input impedance from the equivalent circuit model of the CP patch antenna matches well with the simulated Z_{12} as shown in Fig. 5.6. The radiation Q of the two modes are then calculated as:

$$Q_{rad\_L} = 2\pi f_L R_{p1} C_{p1} \tag{5.11}$$

$$Q_{rad\_H} = 2\pi f_H R_{p2} C_{p2} \tag{5.12}$$

It should be noted that when the CP patch antenna is radiating, the operational frequency of the antenna is between f_L and f_H. In addition, since the two orthogonal modes are excited simultaneously to cause the antenna to radiate, the radiation Q of the CP patch antenna is somewhere between half of Q_{rad_L} and Q_{rad_H}. In this design, Q_{ext2} is selected to be half of Q_{rad_L}.

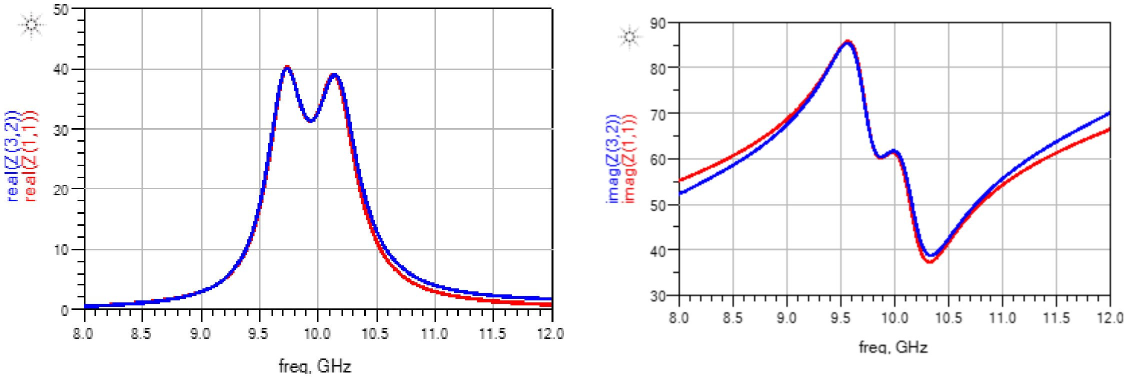

Figure 5.6: Input impedance extracted from the equivalent circuit mode compared with the simulated input impedance.

5.2.2 External Coupling Q_{ext1}

Once Q_{ext2} is chosen, the next step is to design the external coupling to the first resonator, $Q_{ext1,}$ to match the output coupling, Q_{ext2}. As shown in Fig. 5.1(a), the external coupling to the first resonator is provided by a short-ended SMA connector; the position of the SMA connector controls the value of Q_{ext1}. Since the SMA connector is placed along the center of the cavity's width W to maintain symmetry in the x-direction, the only parameter that effects Q_{ext1} is the distance between the SMA connector and the short edge of the cavity, P_s. On the other hand, when moving the SMA connector towards the center of the cavity, the resonant frequency of the cavity will increase. Therefore, in order to obtain the external coupling at the operational frequency f_0 = 10.22 GHz, the dimensions of the cavity (W_1, L_1) need to be optimized in order to maintain the resonant frequency. Fig. 5.7 shows Q_{ext1} changing as a function of P_s at the center frequency f_0. It can be seen that as the distance between the SMA connector and the short edge of the cavity increases, the external coupling of the first cavity resonator decreases. Interpolating from the above design chart, P_s =3.6 mm is chosen as the initial distance from the SMA connector to the short edge of the cavity.

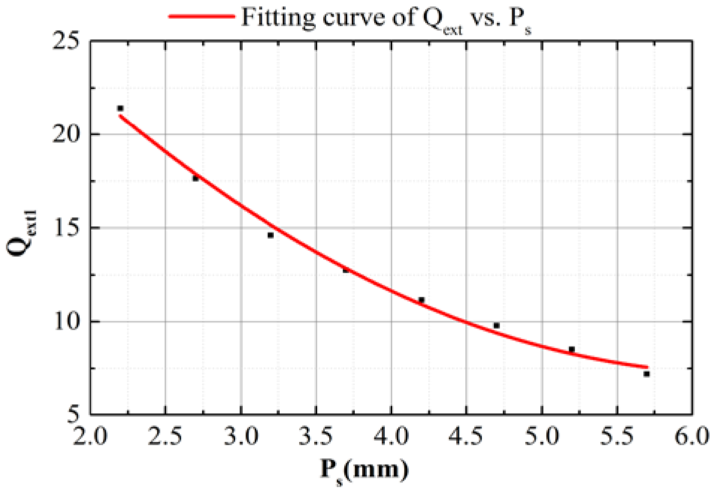

Figure 5.7: External coupling to the first resonator changing with P_s.

5.2.3 Internal Coupling between the First and Second Cavity Resonator k_{12}

The first cavity resonator is coupled to the second cavity resonator through a coupling slot on the second ground plane as shown in Fig. 1. The internal coupling between the first and second resonators, k_{12}, is affected by the slot position X_s, length L_{slot}, and width W_{slot}. As the dimensions of the slot (W_{slot} and L_{slot}) increase, the coupling between the first and second cavity resonators becomes stronger. Also, since the resonators are predominantly magnetically coupled, the coupling will be stronger as the slot moves towards the edge of the cavity resonator. Therefore, there are various combinations of the three parameters that can achieve the desired k_{12}. In this design, the width of the slot is fixed at 0.5mm in order to simplify the optimization. The relationships between k_{12} and the slot position X_s for different slot lengths L_{slot} are plotted in Fig. 5.8. The length of the slot L_{slot} is chosen to be 6.0 mm while X_s is set to 0.75 mm as the initial parameters. It is noted that the slot-loading effect will decrease the resonate frequencies of the two cavities; the dimensions of both cavities need to be reduced in order to compensate for the detuned frequencies.

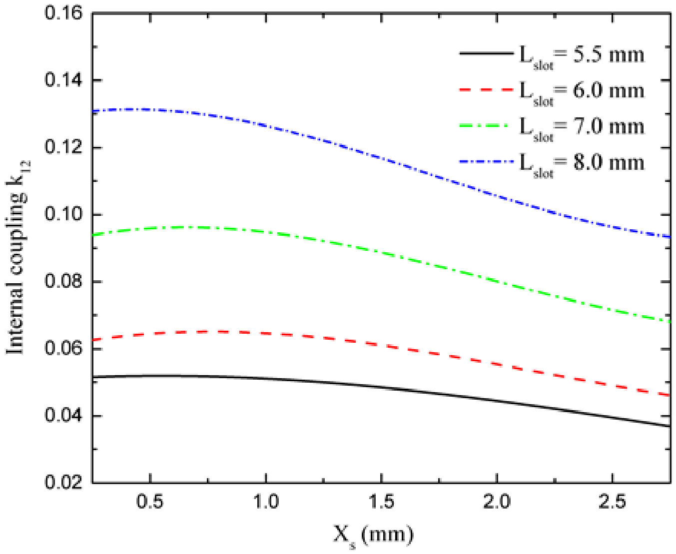

Figure 5.8: Internal coupling between the first and second cavity resonator versus coupling slot position X_s and slot length L_{slot} .

5.2.4 Internal Coupling between the Second Cavity and CP Corner Truncated Patch Antenna k_{23}

In order to preserve the CP performance of the corner-truncated patch antenna, a coupling via is inserted between the second cavity and corner-truncated patch to provide the internal coupling k_{23} as illustrated in Fig. 5.1. The equivalent circuit of the coupling via coupling the second cavity to the patch antenna can be modeled as a shunt inductor to the cavity resonator in series with another inductor to the patch antenna as shown in Fig. 5.3(c). The reactance of the shunt inductor X_p is mainly related to the distance between the coupling via and the short edge of the cavity; the reactance can be calculated as:

$$X_p = Z_0 \tan\left(\beta P_p\right) \tag{13}$$

where β is the propagation constant of the dielectrically loaded waveguide and Z_0 is the characteristic impedance of the waveport. The calculation of the series inductance X_s is more complicated since it is a function of several design parameters including the external coupling location P_c, the length of the second cavity L_2, the distance between the coupling via to the edge of the patch, and the diameter of the coupling via [21]. Though the internal coupling k_{23} is controlled by both X_s and X_p. to reduce the number of parameters and maintain the CP performance, only P_c is changed to achieve the desired k_{23} during the optimization.

5.2.5 CP Filter/Patch Design

After the initial parameters of the integrated CP filter/patch antenna are selected from the aforementioned design charts and equations, the integrated CP filter/patch antenna is simulated using High-Frequency Structure Simulator (HFSS). In order to reduce the optimization time, a time domain tuning technique is used. The simulated S_{11} response in the frequency domain is transformed to the time domain by an inverse Chirp-Z transform; the transformed S_{11} has peaks representing the internal and external couplings and dips representing the resonant frequencies. The peaks and dips can be modified one by one from left to right without effecting subsequent couplings or resonances. By matching the peaks and dips with the time-domain transformed reference filter, a perfect filtering response in the frequency domain is observed as shown in Fig.

5.9. The total realized gain of the CP filter/patch antenna at boresight is also shown in Fig. 5.9. It can be seen that the total realized gain of the integrated CP filter/patch antenna has the same S_{21} roll-off as that of the reference. The final dimensions of CP filter/patch are listed in Fig. 5.1.

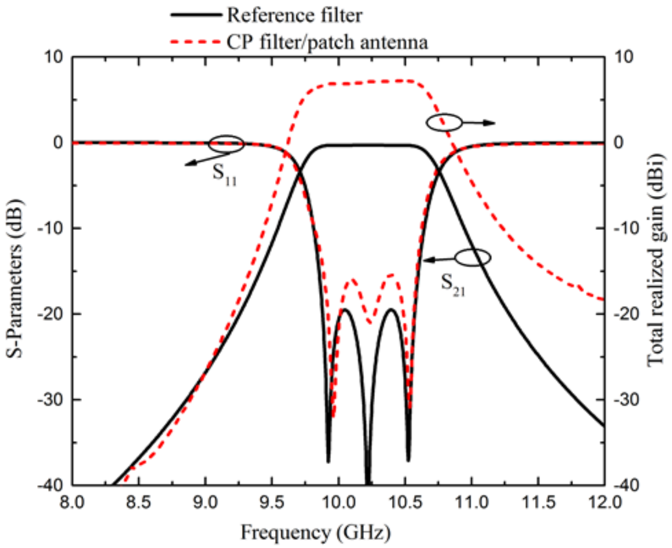

Figure 5.9: Simulated S_{11} and S_{21} of the reference filter using equivalent circuit model compared to simulated S_{11} and total realized gain of the CP filter/patch antenna shown in Fig. 1.

5.2.6 Fabrication and Measurement Results

The integrated CP filter/patch antenna is fabricated on a Rogers RT/Duroid 5880 dielectric in three layers. Each layer is individually fabricated using standard PCB fabrication techniques and then bonded together with solder paste. A copper pin is soldered between the patch antenna and the second cavity to provide the internal coupling k_{23} while an SMA connector is soldered to penetrate the first cavity resonator as the input port. The fabricated CP filter/patch antenna is shown in Fig. 5.10 (a).

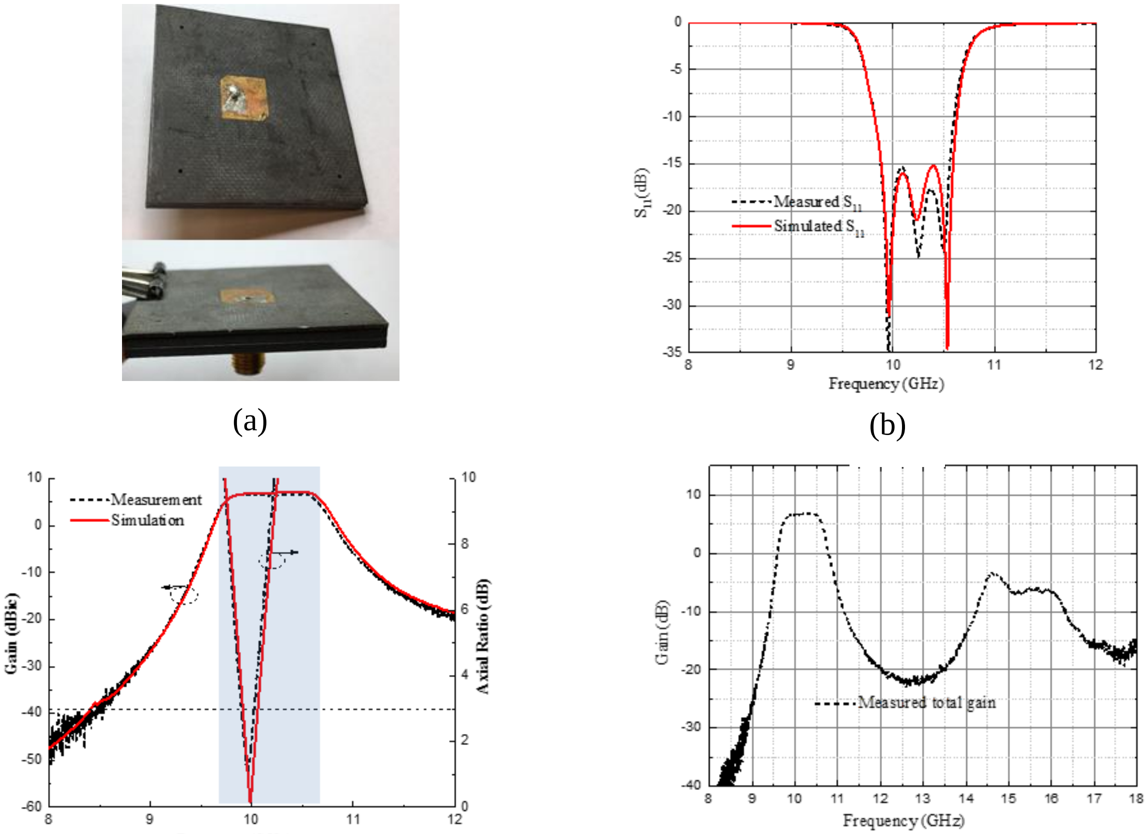

(a) (b) (c) (d)

Figure 5.10: (a) Fabricated CP filter/patch antenna. (b) Simulated and measured S_{11} responses. (c) Simulated and measured gain and axial ratio (d) Wide band response of the filter/antenna.

The S_{11} response of the integrated CP filter/patch is measured with a vector network analyzer, demonstrating an excellent agreement with the simulated result as shown in Fig. 5.10 (b). The measured center frequency is 10.2 GHz and the return loss is better than 10 dB from 9.82 to 10.60 GHz. Within the passband, the return loss is better than 15 dB. It can be seen from Fig. 10 (b) that with two cavity resonators and one CP patch antenna, three transmission poles are achieved in the S_{11} response. The total realized gain of the CP filter/patch antenna is measured in an anechoic chamber with an LP double ridge horn to further verify the filtering function. By vertically and horizontally aligning the LP double ridge horn with the CP filter/patch antenna respectively, two partial realized gains of the CP filter/patch antenna are measured. The total realized gain is the sum of the two measured partial realized gains in linear scale. The measured total realized gain is flat within the passband and has a high out-of-band rejection as shown in Fig. 5.10(c). The simulated and measured total realized gain agree very well with each other and the roll-off slope of the realized gain matches a third order filtering response. The maximum realized gain in the passband is 6.77 dBi, the measured overall efficiency is 88%, and the 3-dB gain bandwidth is from 9.68 to 10.70 GHz. The AR of the CP filter/patch antenna is also measured in the anechoic chamber as presented in Fig. 5.10(c). The measured AR is below 3 dB from 9.92 to 10.02 GHz which is much narrower than the passband; the 3rd order CP filter/patch antenna has a limited S_{11}- AR bandwidth. Fig. 5.10(d) shows the measured wideband response of the CP filter/patch antenna from 8 to 18 GHz. As shown in Fig. 5.10(d), at 14.7 GHz, a spurious mode occurs but the radiating level is 10 dB below that of the fundamental mode. The radiation patterns of LHCP and RHCP radiation in both x-z and y-z planes are measured as shown in Fig. 5.11. It can be clearly seen that the antenna is an RHCP antenna with a cross-polarization level below 10 dB. Note that the orientation of the polarization can be easily changed by placing the truncated corners along the direction of the other diagonal without disturbing the filtering response. To prove this, the CP filter/patch antenna array in the section below is designed to be LHCP instead of RHCP.

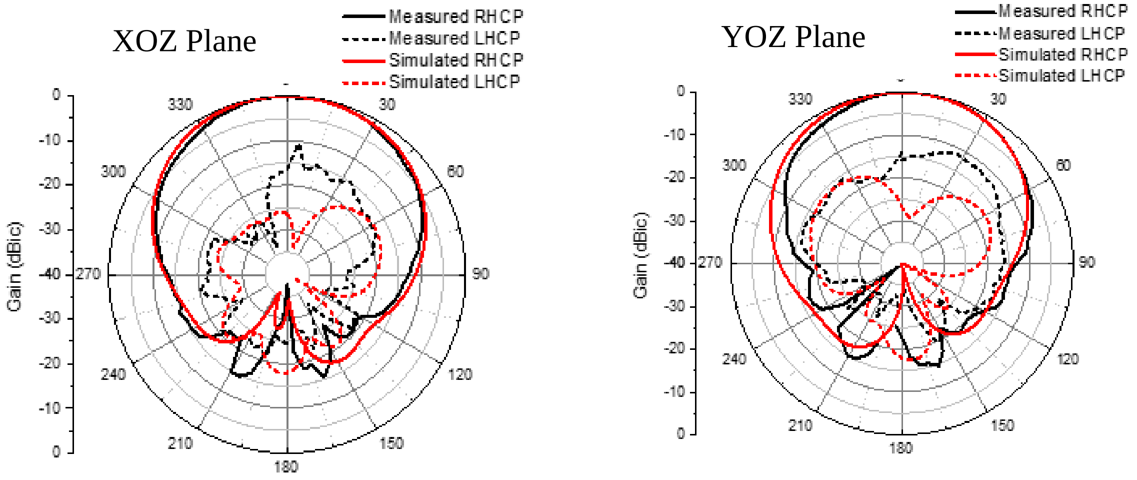

Figure 5.11: Simulated and measured ration patterns.

5.3 Sequentially Rotated 2×2 Circularly Polarized Filter/Patch Array

Though the 3rd–order CP filter/patch antenna has a 10-dB impedance bandwidth of 7.6% and a 3-dB realized gain bandwidth of 9.9%, the operational bandwidth of the CP filter/patch antenna is limited by the 1% 3-dB AR bandwidth as addressed in Section 5.2. One way to efficiently increase the AR bandwidth is by using a sequentially rotated array configuration. By physically rotating each antenna element by 90º and feeding each array element with equal magnitude but with a quadrature phase differential between each adjacent element, the AR bandwidth can be significantly increased due to the cancellation of the radiation impurity [98]. In this section, a sequentially rotated 2×2 CP filter/patch antenna array is presented.

5.3.1 CP Filter/Patch Array Configuration

The exploded view of the 2×2 CP filter/patch antenna array with sequential rotation is displayed in Fig. 5.12. The antenna elements have the same dimensions as the 3^{rd}-order CP filter/patch antenna shown in section 5.2 except that the truncated corners are located along the opposite diagonal. As a result, the 2×2 CP filter/patch antenna is left hand circularly polarized. Each CP filter/patch antenna is rotated by 90° with respect to the previous element. The distance between two adjacent elements is about $0.65\ \lambda_0$ which is limited by the lengths and widths of the cavity resonators. Smaller distances can be achieved by using substrates with a larger dielectric constant for the first and second layer. The overall size of the CP filter/patch antenna array package is $80\times80\times2.37\text{mm}^3$, of which the size of the antenna layer is $80\times80\times0.79\ \text{mm}^3$. The CP filter/patch antenna element is excited with equal amplitude and phases of 0°, 90°, 180°, and 270° to offer the required phase delays for left-hand circular polarization as indicated in Fig. 5.12.

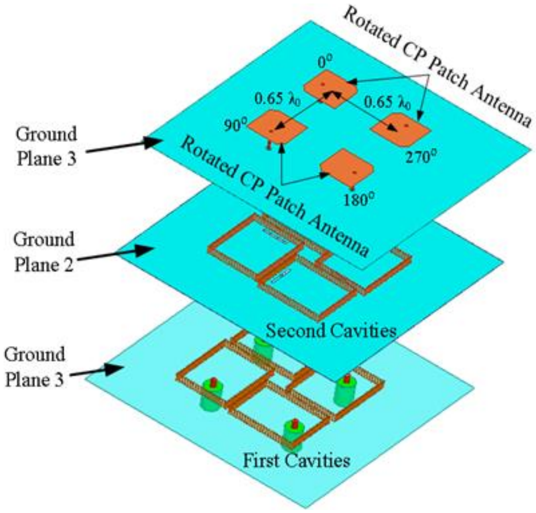

Figure 5.12: Exploded view of the 2×2 sequentially rotated CP filter/patch antenna array.

5.3.2 Feeding Network for the CP Filter/Patch Array

In order to maintain the filtering function of each CP filter/patch antenna element, an external feeding network is used to generate the 0º, 90º, 180º, and 270º phases as shown in Fig. 5.13. The external feeding network uses one 180º hybrid coupler operating from 4 - 18 GHz (RFHB04G18GPI) and two 90º hybrid couplers (RFHB06G18GGVT) with a frequency range of 6 - 18 GHz. When the signal is incident upon the "Δ" port of the 180º hybrid, it divides into port 1 and port 2 with the same magnitude and a 180º phase difference. The two divided signals then pass through the two 90º hybrids, separately generating four equal amplitude signals with 0º, 90º, 180º, and 270º phases. The "∑" port of the 180º hybrid and isolation ports of the 90º hybrids are all terminated with 50-ohm loads. The isolation ports are terminated with 50-ohm loads. With the setup shown in Fig. 5.13, the amplitude imbalance of the four output ports is within ±0.6 dB and the phase imbalance is between ±8º.

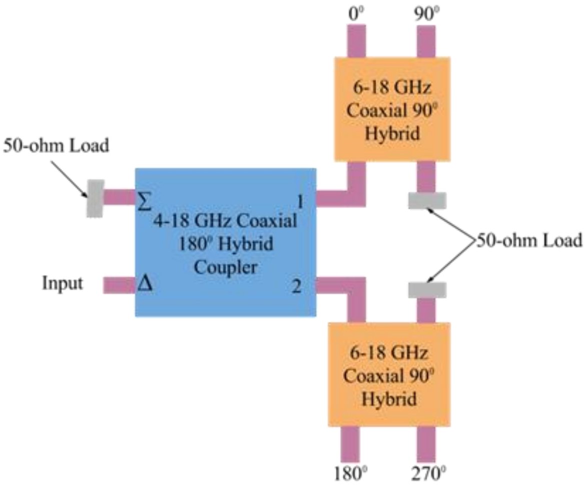

Figure 5.13: Feeding network of the 2×2 sequentially rotated CP filter/patch antenna array.

5.3.3 *Fabrication and Measurement Results*

The 2×2 CP filter/patch antenna array is fabricated with the same PCB fabrication technique as the 3^{rd}-order CP filter patch antenna discussed in section 5.2. A photo of the CP filter/patch antenna array is shown in Fig. 5.14(a). The top layer consists of four rotated corner-truncated patch antennas and the bottom layers are the SIW resonators. Each CP filter/patch antenna element is excited separately through a 50-ohm female SMA connector.

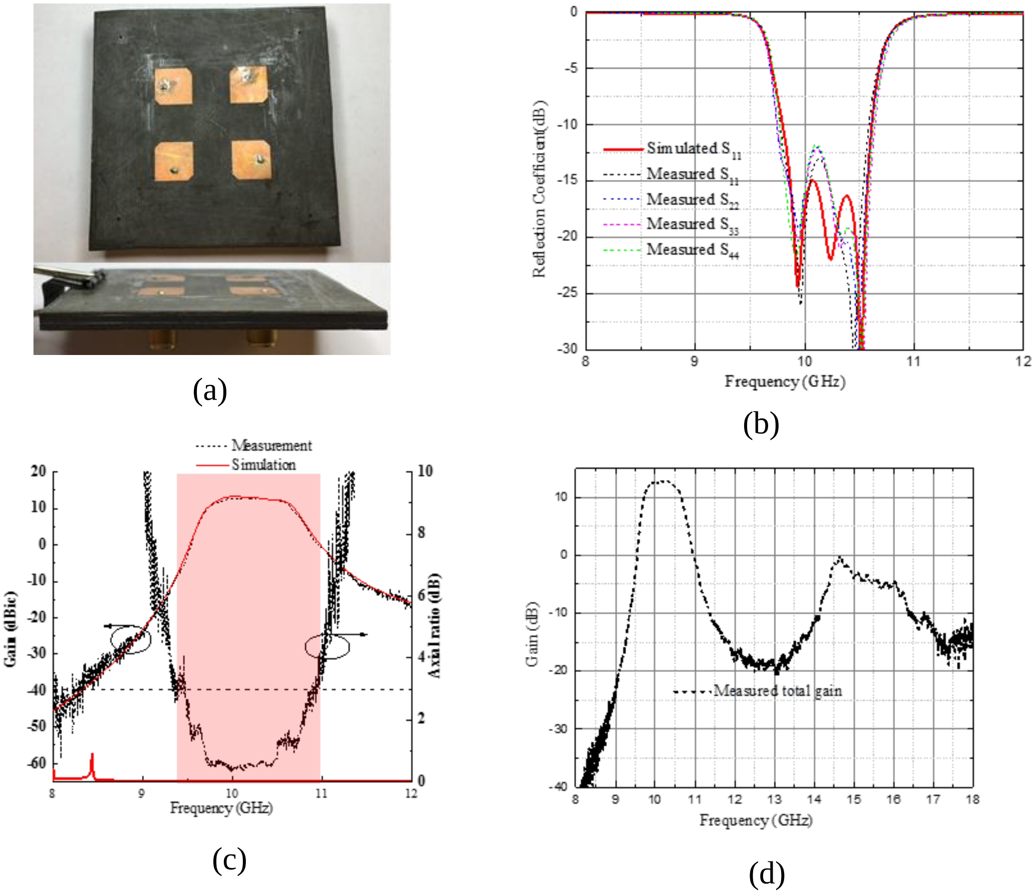

(a)

(b)

(c)

(d)

Figure 5.14: (a) Fabricated 2×2 CP filter/patch antenna array. (b) Simulated and measured S_{11} responses of each CP filter/patch antenna element. (c) Simulated and measured gain and axial ratio of the CP filter/patch antenna array (d) Wide band response of the CP filter/antenna array.

The reflection coefficient of each CP filter/patch antenna element is measured with the other ports terminated by 50-ohm loads as shown in Fig. 5.14(b). It can be seen that the four CP filter/patch antenna elements have similar S_{11} performance with a 10-dB impedance bandwidth of 8.5%. All four elements work as 3^{rd}-order filters. Both the total realized gain and the axial ratio of the 2×2 CP filter/patch antenna array are measured in an anechoic chamber and plotted in Fig. 5.14(c). The maximum realized gain in the passband is 12.89 dBi while the simulated maximum realized gain is 13.1 dBi. The measured overall efficiency is calculated using the measured total realized gain and the simulated directivity at the center frequency which is calculated to be 86%. In the simulation, the overall efficiency can be as high as 91% without considering the feeding network. The 3-dB gain bandwidth is about 9.3% from 9.72 to 10.67 GHz. It also can be seen from Fig. 5.14 (c) that by sequentially rotating the CP filter/patch antenna array elements and feeding them with the required phases, the 3-dB AR bandwidth is significantly enhanced compared with the single CP filter/patch antenna in Section 5.2. The lowest AR is about 0.38 dB at 10 GHz while the 3-dB AR bandwidth is 14.1% from 9.48 to 10.89 GHz, which can cover the whole passband as shown in Fig. 5.14 (c). Therefore, the S_{11}-AR bandwidth of the 2×2 CP filter/patch antenna array is increased to 8.3% without increasing the thickness of the substrate. To compare the S_{11}-AR bandwidth achieved by the CP filter/patch antenna array with the previously reported techniques, the antenna properties including antenna type, center frequency, S_{11}-AR bandwidth, and the thickness of the antenna layer are compared in Table 5.1.

Table 5.1: S_{11}-AR Bandwidth Comparison Among Different Techniques

Antenna Type	f_0 (GHz)	S_{11}-AR FBW (%)	Thickness for antenna layer
CP stacked patch	5.50	14	0.144 λ_0
CP aperture coupled patch	5.84	15	0.128 λ_0
Rotated E-shaped patch	2.45	20	0.0920 λ_0
Rotated corner truncated patch	9.79	3.3	0.0262 λ_0
Rotated CP filter/patch	10.00	8.3	0.0262 λ_0

Moreover, a wideband response of the 2×2 CP filter/patch antenna array is also measured as shown in Fig. 12 (d). From 8-18 GHz, the 2×2 CP filter/patch antenna array also excites a spurious mode at 14.7 GHz but the radiating level of the spurious mode is about 13 dB below that of the fundamental mode. The radiation patterns of CP filter/patch antenna array in both x-z and y-z planes are measured as shown in Fig. 12(e). It can be clearly seen that the antenna is an LHCP antenna with a cross-polarization level below 25 dB.

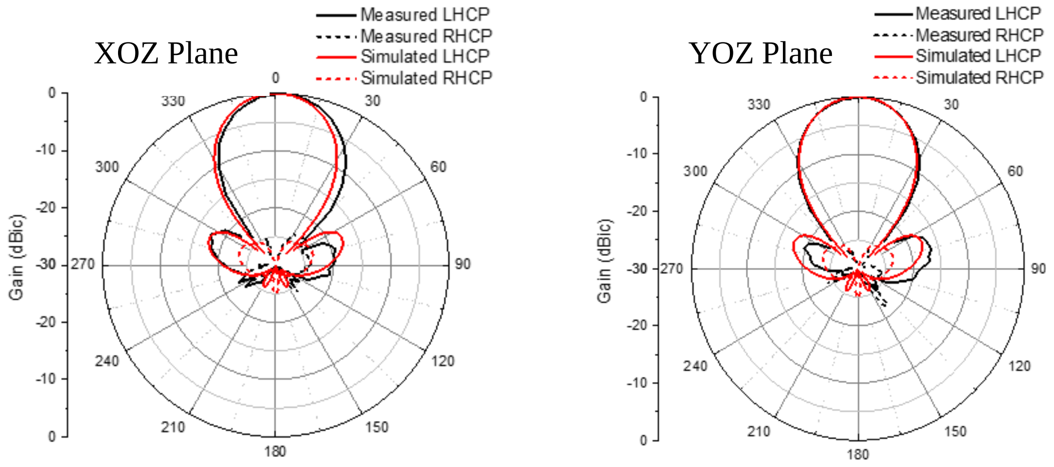

Figure 5.15: Simulated and measured radiation patterns in both XOZ and YOZ plane.

5.4 Conclusion

A synthesis for vertically integrating high-Q SIW filters with probe-fed CP patch antennas was presented in this chapter. A 3rd-order filtering response was achieved by two cavity resonators and one CP patch antenna and again with a 2×2 sequentially rotated CP filter/patch antenna array that were designed, fabricated, and measured. The measurement results of the return loss, gain, and radiation patterns matched very well with the simulated responses. It has been shown that the 2×2 CP filter/patch antenna array has an enhanced S_{11}-AR bandwidth of 8.3% without increasing the thickness of the antenna layer as compared with the single CP filter/patch element. The simulated overall efficiency of the CP filter/patch antenna array is 91%.

CHAPTER 6 TUNABLE INTEGRATED FILTER/ANTENNAS

Chapters 2 and 3 show the advantages of reconfigurable slot-ring antenna/arrays while chapters 4 and 5 present the applications of filter/antenna integration techniques. Is there a way to combine these two techniques together in order to achieve a highly integrated and reconfigurable filter/antenna array? This chapter gives the answer. An evanescent-mode cavity filter integrated with a frequency tunability slot antenna is designed in this chapter.

6.1 Introduction of the Tunable Filter Integrated with Slot Antenna

Reconfigurable filters provide the advantages of multiband and wideband filtering which are crucial for modern microwave systems [99]. High-Q-factor tunable filters have been studied in great detail in the last decades; they are essential for minimizing the attenuation of in-band signals and improving the noise figure of receivers. High-Q tunable filters are commonly achieved by using evanescent-mode cavities for their small volume and high tunability. The center frequency of an evanescent-mode cavity can be easily and profoundly changed by altering the gap between the post top and the cavity ceiling [100]-[102]. Tunable evanescent-mode filters with high Q factors based on RF-MEMS [101] or piezoelectric actuators [102] have been successfully made. On the other hand, reconfigurable antennas are also hot topics in recent years which has been discussed in the previous chapters. In addition, when connecting filters with antennas in communication systems, standard 50-ohm connectors are needed which not only cause extra losses but also enlarge the volume of RF front-ends.

Therefore, in order to remove the additional transition loss and maintain the reconfigurability of both filters and antennas, a tunable two-pole evanescent-mode filter with an integrated slot antenna is designed in this chapter. As shown in Fig. 6.1(b), the capacitive posts loaded at the center of these evanescent-mode cavities are tuned so that the center frequency of the filter/antenna as a unit is changed. The slot antenna is integrated with the second evanescent-mode cavity and acts as the filter output port, maintaining the necessary external Q factor. Therefore, the integration reduces the volume of the connections between filter and antenna but preserves the performance of both.

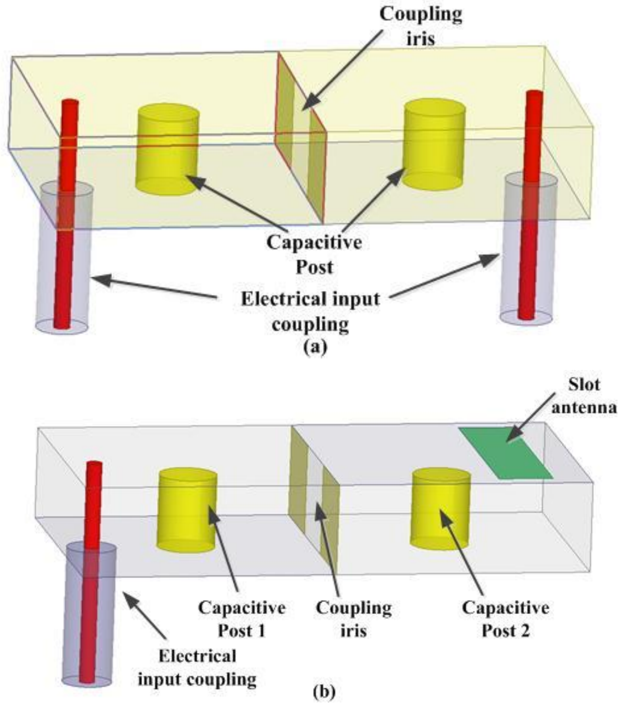

Figure 6.1: (a) Two-pole reference evanescent-mode filter (b) evanescent-mode filter integrated with a slot antenna.

6.2 Design of Integrated Evanescent-Mode Filter/Antenna

As the first step, a reference two-pole evanescent-mode filter is designed at 8.56 GHz as shown in Fig. 6.1(a). Open-ended 50-ohm coaxial connectors are used to provide external coupling through the electric field. The internal coupling is determined by the irises in the common wall between the two resonators with a width of 4.8 mm. The design parameters are shown below:

$$Q_{ext} = 51.37 \quad k_{12} = 0.023 \tag{6.1}$$

The length and width of the cavities are 14 mm and the height is 5 mm. The posts with a diameter of 3.18 mm located at the center of each cavity produce an extra capacitive load which lowers the resonant frequency. The designed filter has a fractional bandwidth of 2.86%, with a relatively low insertion loss of 0.18 dB.

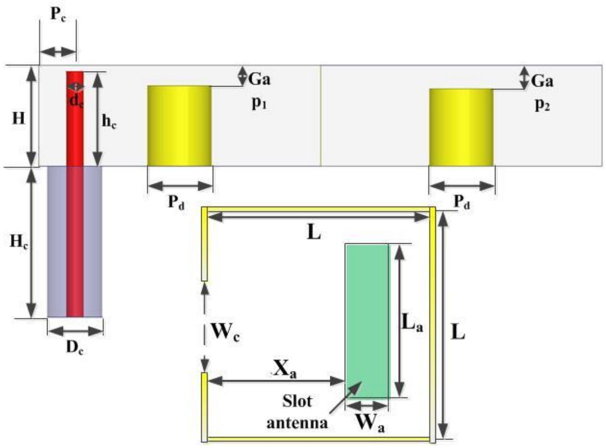

Figure 6.2: Dimensions of the evanescent-mode filter/antenna H= 5, H_c = 7.5, h_c = 4.7, d_c = 0.87, D_c = 2.73, P_c = 1.8, P_d = 3.18, Gap_1 = 1, Gap_2 = 1.15, L = 14, W_c= 4.6, L_a =11.92, X_a = 9, and W_a = 3 (all dimensions are in mm).

To integrate the slot antenna with the filter, the second port is replaced by the slot antenna. The second cavity and its slot must have the same external coupling coefficient $Q_{ext,2}$ and center frequency f_0 as the first cavity. The position and dimension of the slot control the coupling between the antenna and cavity. For evanescent-mode resonators, the distribution of electric and magnetic fields is concentrated in proximity of the post. As a result, the distance between the post and edge of the slot antenna plays a critical role in changing $Q_{ext,2}$. In order to simplify the procedure of finding the right position and dimensions, x_a = 9 mm and w_a = 3 mm are fixed as shown in Fig. 6.2. A sweep of L_a is done to achieve $Q_{ext,2}$ = 51.37 and a time-domain filter analysis method [102] is used for the fine tuning. Finally, L_a = 1.04 mm and Gap_1 = 1.15 mm are chosen for the filter/antenna external coupling as the reference filter while also providing the same radiation performance as the slot antenna. Frequency- and time-domain responses of the reference filter and filter/antenna are shown in Fig. 3, demonstrating good agreement between the two.

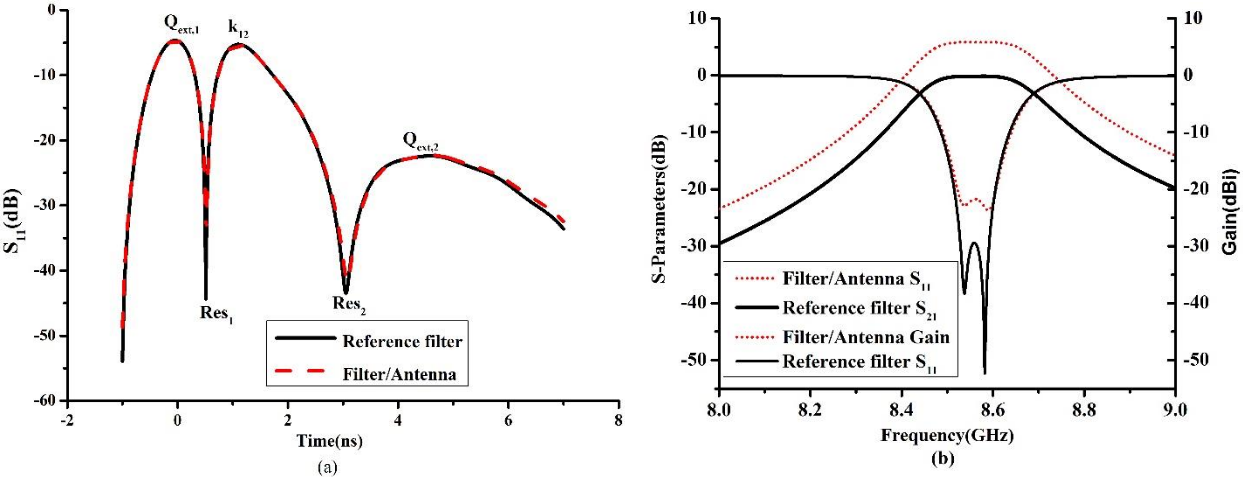

(a)
(b)

Figure 6.3: Simulated results of the evanescent-mode filter and filter/antenna in (a) time domain and (b) frequency domain.

6.3 Simulation Results of the Tunable Filter/Antenna

Tuning the gap between the top of the post and the cavity ceiling causes the center frequency of the evanescent-mode filter/antenna to change as shown in Fig. 4. The filter/antenna is tunable from

8.18 to 8.80 GHz and the peak gain of the filter/antenna is very flat with a minimum gain of 5.6 dBi and a maximum of 5.8 dBi. This change in gain is primarily due to the change in the matching of the filter/antenna, not from the loss of the filter or the transition between the filter and antenna.

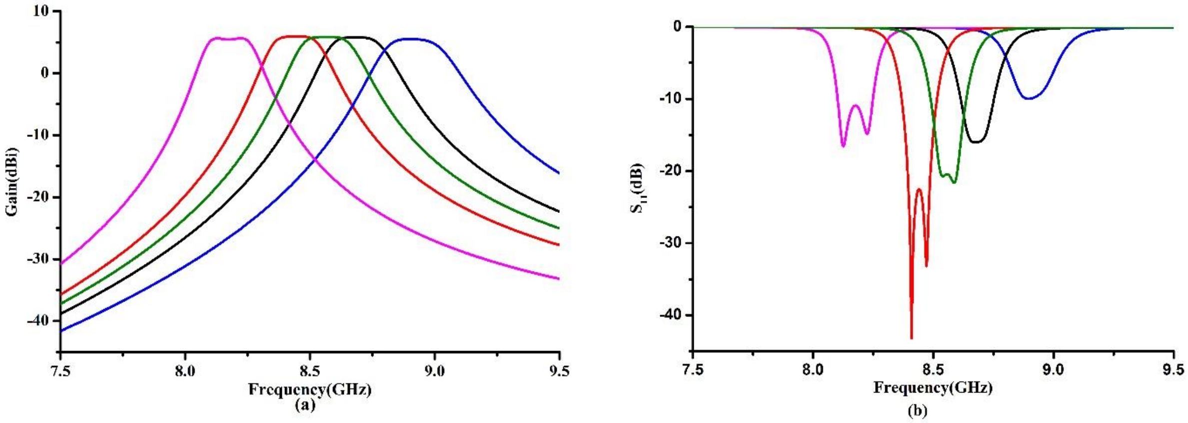

Figure 6.4: Simulated results of the tunable filter/antenna.

6.4 Fabrication and Measurement Results of the Tunable Filter/Antenna

The center frequency of the evanescent-mode filter/antenna is re-designed at 6.8 GHz in order to leave enough margin for fabrication tolerance. An updated 3-D model of the integrated filter/antenna is simulated in HFSS as shown in Fig. 6.5. The evanescent-mode cavities are realized by air boxes loaded with M3 screws inside a larger aluminum box. By cutting a slot on the top of the aluminum box, the power can be radiated from the second cavity to the free space. An SSMA connector is used to provide the external coupling of the evanescent-mode filter/slot antenna. Both the reference filter and the integrated filter/antenna are fabricated as shown in Fig. 6.6.

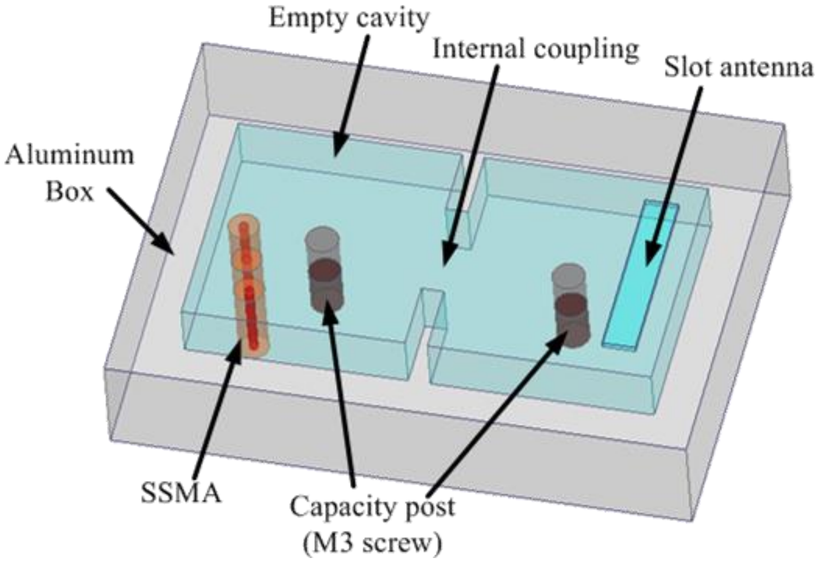

Figure 6.5: Updated 3-D model of the integrated filter/antenna.

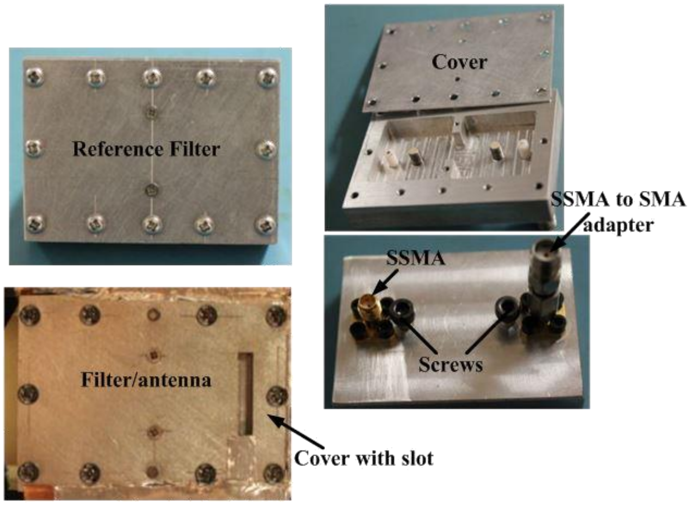

Figure 6.6: Fabricated reference filter and filter/antenna.

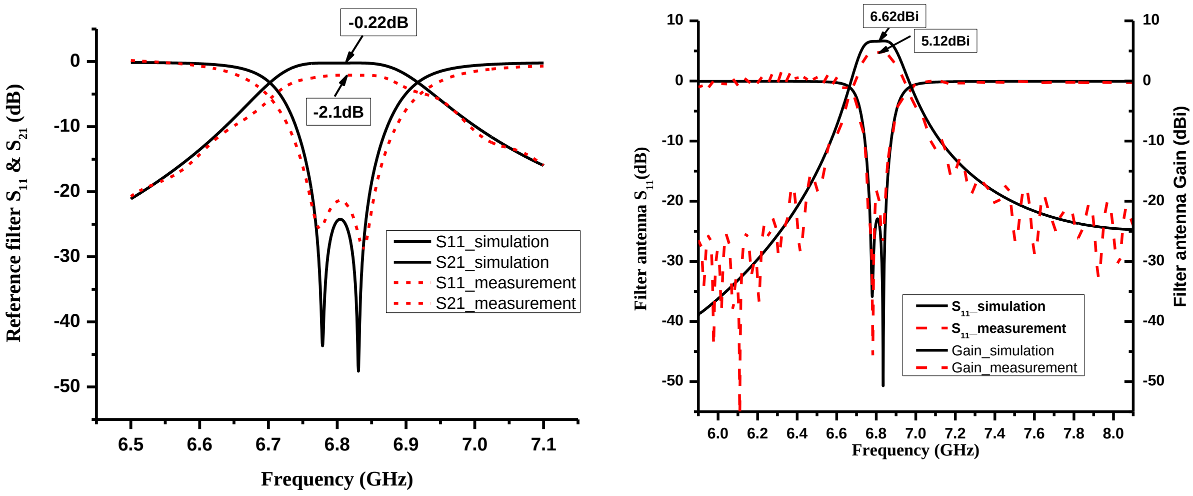

(a) (b)

Figure 6.7: Frequency-domain measurement of (a) reference filter and (b) integrated filter/antenna.

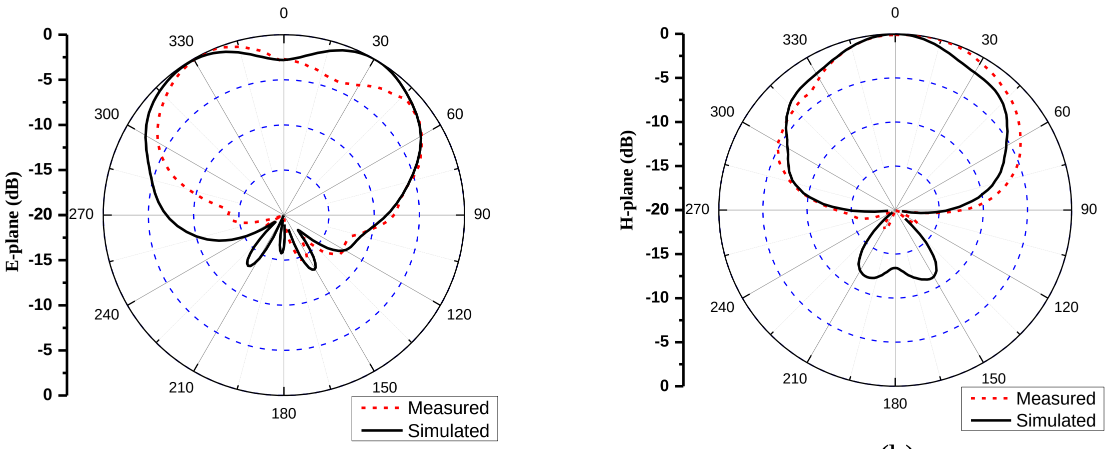

(a) (b)

Figure 6.8: Radiation pattern of the integrated filter/antenna at 6.8 GHz.

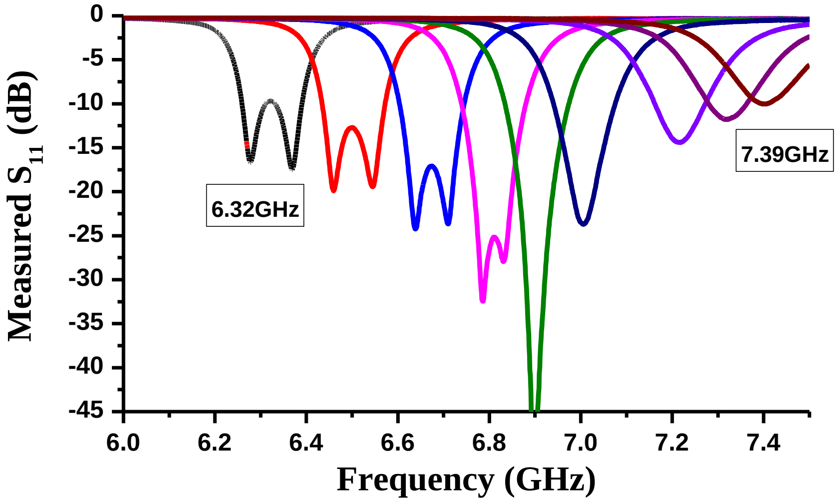

Figure 6.9: Measured tuning range of the evanescent-mode filter/antenna.

The S-parameters of both the reference filter and the integrated evanescent-mode filter/antenna are measured by a Vector Network Analyzer (VNA) and are shown in Fig. 6.7. As shown in Fig. 6.7 (a), the measured S_{11} is below 20 dB across the filter passband, which matches with the simulated results. However, the measured insertion loss is 1.9 dB higher than the simulation. This is due to the roughness of the fabricated cavity surface as shown in Fig. 6.6, which highly degrades the Q-factor. Similar performance is also observed in Fig. 6.7 (b), showing the filter/antenna. The measured S11 of the integrated filter/antenna agrees well with the simulated return loss while the measured gain is about 1.5 dB lower than the simulated gain. Both E- and H- plane radiation patterns of the integrated evanescent-mode filter/antenna are measured at 6.8 GHz. By turning the screws in and out, the center frequency of the integrated filter/antenna can be changed from 6.32 to 7.39 GHz, covering a 20% tuning range.

6.5 Conclusion

A two-pole evanescent-mode filter/antenna with a tunable center frequency is presented. The simulated results of the filter/antenna match well with the reference filter. A 20% tuning range is achieved by turning the screws, changing the gap between the post and the top of the cavity. In addition, the filter/antenna maintains a high gain throughout the tuning range. Furthermore, this integration of the evanescent-mode filter and slot antenna has reduced the volume of the device and removed loss from 50-ohm connections. Therefore, this integration technique will be very useful for the realization of future reconfigurable RF front-ends.

CHAPTER 7 SUMMARY AND FUTURE WORK

7.1 Summary

This dissertation focuses on the enhancement of antenna array performance. In order to obtain antenna arrays with a reduced size, higher efficiency, lower cost, and more functionality, reconfigurable slot-ring antenna arrays and integrated CP filter/antenna arrays are studied. A number of contributions are listed as follows.

First, a continuously tunable S-band slot-ring antenna with tuning provided by varactors was simulated, fabricated, and measured. The measured results showed that the tunable slot-ring antenna has an octave bandwidth of 2:1. An L/S-band reconfigurable slot-ring antenna/array formed by four continuously tunable S-band slot-ring antennas was designed. It can be seen from the HFSS simulation results that the reconfigurable slot-ring antenna array is able to operate as an L-band slot-ring antenna or a 2×2 S-band slot-ring antenna array, controlled by discrete switching states.

To reduce the number of switches and varactors in the reconfigurable slot-ring antenna/array, a fractal-shaped reconfigurable slot-ring antenna/array was demonstrated. The fractal reconfigurable slot-ring antenna can cover either S- or C-band without varactors. In addition, by adding two orthogonal feeding lines to each band, dual-polarization was achieved. Furthermore, since the antenna operates as a 2×2 antenna array at C-band, the main beam can be steered to different positions if a phase difference is applied to each element. Ground plane solutions were explored including adding a metal plane and EBG structures underneath the reconfigurable antenna/array to achieve single-sided radiation.

Comparison between integrated filter/patch antennas and stand-alone patch antennas were presented. It was shown that the integrated filter/patch antenna has a wider FBW than a probe-fed patch antenna on a substrate with the same thickness. A linearly polarized 2nd–order integrated filter/patch phased array was simulated and compared with a probe-fed patch phased array on substrates with different thicknesses. It is seen that the integrated filter/patch phased array achieves a wider scan angle with enhanced FBW as compared to the standalone phased array.

In addition, a 3rd-order SIW filter integrated with a single-fed corner-truncated patch antenna was demonstrated. The integrated CP filter/patch has a wide impedance bandwidth but narrow axial-ratio bandwidth. In order to obtain an enhanced impedance-axial-ratio bandwidth, a 2×2 sequentially rotated CP filter/patch antenna array was designed. Fabrication and measurement results were presented and shown that the 2×2 CP filter/patch antenna array achieves an S_{11}-AR bandwidth of 8.3% without increasing the thickness of the antenna layer.

Finally, a tunable evanescent-mode filter integrated with a slot antenna was shown to validate the concept of combining reconfigurable antennas and integrated filter/antennas. By changing the distance between the metallic post top and cavity ceiling, the center frequency of the integrated filter/antenna is able to be tuned from 8.18 to 8.80 GHz. The shape of the filtering response remains constant over the tuning range.

7.2 Future Work

7.2.1 Large Fractal-Shaped Reconfigurable Slot-Ring Antenna Array

The S/C-band fractal-shaped reconfigurable slot-ring antenna/array shown in Chapter 3 can be extended to a larger antenna array. By increasing the number of antenna elements, the directivity of the antenna array in both S- and C-band can be increased. In addition, by applying a phase difference to each antenna element, the beam of the reconfigurable antenna array can be steered in both S- and C-band. As a result, an antenna array with versatility in frequency bands, polarization, and radiation pattern will be achieved.

7.2.2 Tri-band Fractal-Shaped Reconfigurable Slot-Ring Antenna Array

A tri-band fractal-shaped reconfigurable slot-ring antenna array that can cover X-, C- and S-band can be developed. Since the fractal-shaped slot-ring antenna has a self-similar structure, by scaling the physical size of the slot-shape, an X-band fractal-shaped slot-ring antenna can be easily designed. By strategically placed the switches and the fractal-shaped slot-rings, a reconfigurable slot-ring antenna array with the ability to switch frequency between X-, C-, and S-bands is able to be obtained.

7.2.3 Electrically Tunable Integrated Filter/Antenna

A tunable filter integrated with slot antenna is presented in this dissertation. The center frequency of the filter/antenna is changed by mechanically changing the length of the loaded metallic posts. An electrically tunable integrated filter/antenna can be achieved by employing MEMS varactors. In addition, patch antennas integrated with microstrip line filters can also be tuned by adding varactors on the radiating edge of the patch and the E-field maximum on the microstrip line.

7.2.4 Reconfigurable Integrated Filter/Antenna Array

This research is also a prelude to the future work in reconfigurable integrated filter/antenna arrays. By combing the benefits from both integrated filter/antennas and reconfigurable antennas, tunable integrated filter/antenna arrays will meet the requirements of the most advanced wireless communication systems.

LIST OF REFERENCES

[1] Hodgkinson, T. G., "Wireless Communications --- The Fundamentals," *BT Technology Journal Springer*, 11-26, 2007

[2] B. Sklar, Digital Communications: Fundamentals and Applications, 2nd ed. New Jersey: Prentice Hall, 2001

[3] D.J. Wikin. I. Hankan, M.S. Woolfson, "Target Vacking Algorithms for Phased Array Radar": *IEE Proceedings - F*, vol. 138, pp 255- 262, no. 3, Jan. 1991.

[4] C. Balanis, *Antenna Theory, Analysis, and Design*, 2nd ed. New York: Wiley, 1997.

[5] H. Singh, H. L. Sneha, and R. M. Jha, "Mutual Coupling in Phased Arrays: A review," Int. J. Antennas Propag., vol. 2013, no. Article ID 348123, p. 23.

[6] N. Atkinson. (2015, Dec. 23). "ALMA NOW A FULL-FLEDGED OBSERVATORY" [Online]. Available: http://www.universetoday.com/100713/alma-now-a-full-fledged-observatory/

[7] GEORGIA INSTITUTE OF TECHNOLOGY RESEARCH NEWS (2005, May 25). "Adaptive Antenna Array Could Improve Access to NASA's Earth Observing Satellites". [Online]. Available: https://www.eurekalert.org/pub_releases/2005-05/giot-aaa052405.php

[8] S. Rhee, D. Seetharam and S. Liu, 'Techniques for Minimizing Power Consumption in hw Dah-Rate Wireless Sensor Networks." Proc. of *IEEE Wireless Communications und Networking Conference (WCNC '03)*, Atlanta, G.4 March, 2004.

[9] T. Pering, Y. Agarwal, R. Gupta, and R. Want. CoolSpots: Reducing the Power Consumption of Wireless Mobile Devices with Multiple Radio Interfaces. *In Proc. ACM MobiSys*, pages 220–232, June 2006.

[10] H. A. Majid, M. K. A. Rahim, M. R. Hamid, and M. F. Ismail, "A Compact Frequency Reconfigurable Narrowband Microstrip Slot Antenna," *IEEE Antennas Wireless Propag. Lett.*, vol. 11, pp. 616–619, 2012.

[11] J.C. Cheng, and Y. Hsieh. "Reconfigurable Multi-Polarization and Multi-Band Circular Patch Antennas Implemented by Large Amount of Diode Switches." *Electromagnetics: Applications and Student Innovation Competition (iWEM), 2016 IEEE International Workshop on*. IEEE, 2016.

[12] Rama Krishna, D., Muthukumar, M., & Pandharipande, V. M. “Design and Development of Reconfigurable Rectangular Patch Antenna Array for Tri-band Applications”,AEU International Journal of Electronics and Communications, Vol. 69, No.1, pp. 56–61.

[13] I. Nazir, , I. E. Rana, E., N.U. A. Mir, & K. Afreen, “Design and Analysis of a Frequency Reconfigurable Microstrip Patch Antenna Switching Between Four Frequency Bands.” *Progress In Electromagnetics Research C*, *68*, 179-191.

[14] M. C. L. Purisima,, M. Salvador, S. G. P. Agustin, & M. T. Cunanan, “Frequency and Pattern Reconfigurable Antennas for Community Cellular Applications.” In *Region 10 Conference (TENCON), 2016 IEEE* (pp. 3767-3770).

[15] G. M. Rebeiz, RF MEMS Theory, Design, and Technology. John Wiely and Sons, 2003.

[16] K. Topalli, E. Erdil, O. A. Civi, S. Demir, S. Koc, and T. Akin, “Tunable Dual-Frequency RF MEMS Rectangular Slot Ring Antenna,” Sensors and Actuators A, vol. 156, no. 2, pp. 373–380, 2009.

[17] K. R. Boyle and P. G. Steeneken,“A Five-Band Reconfigurable PIFA for Mobile Phones,” *IEEE Transactions on Antennas and Propagation*, vol. 55, no. 11, pp. 3300–3309, 2007.

[18] C.-Y. Chiu, J. Li, S. Song, and R. D. Murch, “Frequency Reconfigurable Pixel Slot Antenna,” *IEEE Transactions on Antennas and Propagation*, vol. 60, no. 10, pp. 4921–4924, 2012.

[19] S. Yang, H. K. Pan, A. E. Fathy, S. El-Ghazaly, and V. K. Nair, “A Novel Reconfigurable Mini-maze Antenna for Multi-service Wireless Universal Receiver using RF MEMS,” in Proceedings of the IEEE MTT-S InternationalMicrowave Symposium Digest, pp.182–185, June 2006.

[20] D. E. Anagnostou, G. Zheng, L. Feldner et al., “Silicon-etched Re-configurable Self-similar Antenna with RF-MEMS Switches,” in *IEEE Antennas and Propagation Society Symposium*, vol. 2, pp. 1804–1807, June 2004.

[21] X. Yang, B. Wang, Y. Zhang, “A Reconfigurable Hilbert Curve Patch Antenna, ” *IEEE Antennas and Propagation Society International Symposium*, Vol. 2B, 3-8 July 2005, pp. 613 – 616.

[22] G. Huff, J. Feng. D Zhang, J.T. Bernard, A Novel Radiation Pattern and Frequency Reconfigurable Single Turn Square Spiral Microstrip Antenna, IEEE Microwave and Wireless Components Letters, Vol. 13, No. 2, February 2003, pp. 57- 59.

[23] C. Jung; M. Lee; G.P. Li, F. De Flaviis, Reconfigurable Scan-Beam Single-Arm Spiral Antenna Integrated with RFMEMS Switches, *IEEE Transactions on Antennas and Propagation*, Vol. 54, Issue 2, Part 1, Feb. 2006, pp. 455 – 463.

[24] A. Grau, J. Romeu, M. J. Lee, S. Blanch, L. Jofre, and F. De Flaviis, “A Dual-Linearly-Polarized MEMS-Reconfigurable Antenna for Narrowband MIMO Communication Systems,” *IEEE Transactions on Antennas and Propagation*, vol. 58, no. 1, pp. 4–17, 2010.

[25] J. Balcells, Y. Damgaci, B. A. Cetiner, J. Romeu, and L. Jofre. “Polarization Reconfigurable MEMS-CPW Antenna for mmwave Applications,” in Proceedings of the *4th European Conference on Antennas and Propagation* (EuCAP ’10), April 2010.

[26] R. White and G. M. Rebeiz, “Single- and Dual-Polarized Tunable Slot-Ring Antenna,” *IEEE Trans. Antennas Propag.,* vol. 57, no. 1, pp. 439–448, Jan. 2009.

[27] N. Behdad and K. Sarabandi, “A Varactor Tuned Dual-Band Slot Antenna,” *IEEE Trans. Antennas Propag*., Special Issue on Multifunction Antennas and Antenna Systems, pt. II, vol. 54, no. 1, pp. 401–408, Jan. 2006.

[28] S. V. Hum and H. Y. Xiong, “Analysis and Design of a Differentially-Fed Frequency Agile Microstrip Patch Antenna,” IEEE Transactions on Antennas and Propagation, vol. 58, no. 10, pp. 3122–3130, 2010.

[29] Erdil, E.,Topalli, K., Unlu, M., Civi, O., and Akin, T. “Frequency Tunable Microstrip Patch Antenna using RF MEMS Technology”. *IEEE Transaction on Antennas and Propagation*, Vol. 55(4). pp 1193–1196, 2007.

[30] S. L.-S. Yang, A. A. Kishk, and K.-F. Lee, ‘‘Frequency Reconfigurable U-slot Microstrip Patch antenna,’’ IEEE Antennas Wireless Propag. Lett., vol. 7, pp. 127–129, Jan. 2008.

[31] T. Koroˇsec, P. Ritoˇsa, and M. Vidmar, “Varactor-tuned Microstrip-Patch Antenna with Frequency and Polarization Agility,” *Electronics Letters*, vol. 42, no. 18, pp. 1015–1016, 2006.

[32] Y. Bai, S. Xiao, C. Liu, X. Shuai, and B. Wang, ‘‘Design of Pattern Reconfigurable Antennas Based on a Two-Element Dipole Array Model,’’ IEEE Trans. Antennas Propag., vol. 61, no. 9, pp. 4867–4871, 2013.

[33] J. J. Luther and X. Gong, “A Microstrip Patch Phased Array Antenna with Parasitic Elements and Reactance-Tuned Coupling,” in *IEEE AP-S Int. Symp*., 2011, pp. 3291–3294.

[34] S. Zhang, G. H. Huff, J. Feng, and J. T. Bernhard, “A Pattern Reconfigurable Microstrip Parasitic Array,” *IEEE Trans. Antennas Propag.,* vol. 52, pp. 2773–2776, Oct. 2004.

[35] W. Ouyang and X. Gong, "Frequency-Reconfigurable Single-layer Design of Microstrip Patch Electrically-steerable Parasitic Array Radiator(ESPAR)," 2016 *International Workshop on Antenna Technology (iWAT),* Cocoa Beach, FL, 2016, pp. 154-156.

[36] L. R. Tan, R. X. Wu, C. Y. Wang and Y. Poo, "Magnetically Tunable Ferrite Loaded SIW Antenna," in *IEEE Antennas and Wireless Propagation Letters*, vol. 12, no. , pp. 273-275, 2013.

[37] H. Jiang, M. Patterson, C. Zhang, and G. Subramanyan, ‘‘Frequency Tunable Microstrip Patch Antenna Using Ferroelectric Thin Film Varactor,’’ in *Proc. IEEE Nat. Aerospace Electron. Conf.*, Jul. 2009, pp. 248–250.

[38] D. Rodrigo, L. Jofre, and B. Cetiner, ‘‘Circular Beam-Steering Reconfigurable Antenna with Liquid Metal Parasitics,’’ *IEEE Trans. Antennas Propag.*, vol. 60, no. 4, pp. 1796–1802, 2012.

[39] J. Modelski and Y. Yashchyshyn, “Semiconductor and Ferroelectric Antennas,” in *Proceedings of the Asia-Pacific Microwave Conference (APMC ’06)*, pp. 1052–1059, December 2006.

[40] L. Liu and R. J. Langley, "Liquid Crystal Tunable Microstrip Patch Antenna," in *Electronics Letters*, vol. 44, no. 20, pp. 1179-1180, September 25 2008.

[41] F. N. Ayoub et al., ‘‘Frequency-Tunable Patch Array using Highly Anisotropic Liquid Crystal,’’ in *Proc. IEEE Int. Symp. Antennas Propag*., 2014.

[42] W. Su, B. Cook, M. Tentzeris, C. Mariotti and L. Roselli, "A Novel Inkjet-Printed Microfluidic Tunable Coplanar Patch Antenna," *2014 IEEE Antennas and Propagation Society International Symposium (APSURSI)*, Memphis, TN, 2014, pp. 858-859.

[43] S. J. Mazlouman, A. Mahanfar, C. Menon, and R. G. Vaughan, “Square Ring Antenna with Reconfigurable Patch Using Shape Memory Alloy Actuation,” *IEEE Transactions on Antennas and Propagation*, vol. 60, no. 12, pp. 5627 – 5634, 2012.

[44] Y. Tawk, J. Costantine, K. Avery, and C. G. Christodoulou, “Implementation of a Cognitive Radio Front-End Using Rotatable Controlled Reconfigurable Antennas,” *IEEE Transactions on Antennas and Propagation*, vol. 59, no. 5, pp. 1773 – 1778, 2011.

[45] J. T. Bernhard, E. Kiely and G. Washington, "A Smart Mechanically Actuated Two-Layer Electromagnetically Coupled Microstrip Antenna withVariable Frequency, Bandwidth, and Antenna Gain," in *IEEE Transactions on Antennas and Propagation*, vol. 49, no. 4, pp. 597-601, Apr 2001.

[46] N. Haider, D. Caratelli, and A. G. Yarovoy, “Recent Developments in Reconfigurable and Multiband Antenna Technology,” *Int. J. Antennas Propag.*, 2013, 14 pages, Article ID 869170.

[47] B. A. Cetiner, H. Jafarkhani, Jiang-Yuan Qian, Hui Jae Yoo, A. Grau and F. De Flaviis, "Multifunctional Reconfigurable MEMS Integrated Antennas for Adaptive MIMO Systems," in *IEEE Communications Magazine*, vol. 42, no. 12, pp. 62-70, Dec. 2004.

[48] J. Kovitz and Y. Rahmat-Samii, "Micro-Actuated Pixel Patch Antenna Design Using Particle Swarm Optimization," in *Antennas and Propagation (APSURSI), 2011 IEEE International Symposium on*, 2011, pp. 2415-2418.

[49] A. Grau and F. De Flaviis, “A Distributed Antenna Tuningunit Using a Frequency Reconfigurable PIXEL-Antenna,” in *Proceedings of the 4th European Conference on Antennas and Propagation (EuCAP ’10)*, pp. 1 – 5,April 2010.

[50] Y. Li, W. Li, and Q. Ye, “A Reconfigurable Triple-Notch-Band Antenna Integrated with Defected Microstrip Structure Bandstop Filter for Ultra-Wideband Cognitive Radio Applications,” *International Journal of Antennas and Propagation*, vol. 2013, Article ID 472645, 13 pages, 2013.

[51] N. J. Smith, D. K. Papantonis and J. L. Volakis, "Bandwidth Reconfigurable Utra-Wideband Arrays," 2014 *IEEE Antennas and Propagation Society International Symposium (APSURSI),* Memphis, TN, 2014, pp. 555-556.

[52] D. K. Papantonis, N. Ghalichechian and J. L. Volakis, "Reconfigurable Ultra-Wideband Array with Tunable Band Rejection Across a 7:1 Bandwidth," *2015 IEEE MTT-S International Microwave Symposium*, Phoenix, AZ, 2015, pp. 1-3.

[53] M. Novak, and J. L. Volakis, "Dual Polarized Tightly Coupled Array (TCDA) for UHF to Millimeter Wave Applications," 2014 *IEEE AP-S/URSI, Memphis*, Tennessee, July 6-11,2014.

[54] R. S. Chu, K. M. Lee, and A. T. S. Wang, “Multiband Phased Array Antenna with Interleaved Tapered-Elements and Waveguide Radiators,” in *Proceedings of the AP-S International Symposium & URSI Radio Science Meeting*, vol. 3, pp. 1616 – 1619, July 1996.

[55] N. Haider, D. P. Tran, A. G. Roederer, and A. G. Yarovoy,“Reconfigurable L/S Band Phased Array,” *Electronics Letters*, vol.47, no. 23, pp. 1265–1266, 2011.

[56] C. I. Coman, I. E. Lager, and L. P. Ligthart, “The Design of Shared Aperture Antennas Consisting of Differently Sized Elements,” *IEEE Transactions on Antennas and Propagation*, vol. 54, no. 2, pp. 376–383, 2006.

[57] K. Naishadham, R. Li, L. Yang, T. Wu, W. Hunsicker and M. Tentzeris, "A Shared-Aperture Dual-Band Planar Array With Self-Similar Printed Folded Dipoles," in *IEEE Transactions on Antennas and Propagation*, vol. 61, no. 2, pp. 606-613, Feb. 2013.

[58] C. I. Coman, I. E. Lager, and L. P. Ligthart, “Multifunction Antennas—The Interleaved Sparse Sub-Arrays Approach,” in *Proc. 36th Eur. Microw. Conf. EuMC*, Manchester, UK, Sep. 2006., pp. 1794–1797

[59] K. Naishadham, R. Li, L. Yang, T. Wu, W. Hunsicker and M. Tentzeris, "A Shared-Aperture Dual-Band Planar Array With Self-Similar Printed Folded Dipoles," in *IEEE Transactions on Antennas and Propagation*, vol. 61, no. 2, pp. 606-613, Feb. 2013.

[60] J. Zhang, G. Goussetis, L. Richard, G. Huang, V. Fusco and F. Dielacher, "Low Noise Amplifier With Integrated Balanced Antenna for 60 GHz Wireless Communications," in *IEEE Transactions on Antennas and Propagation*, vol. 62, no. 6, pp. 3407-3411, June 2014.

[61] V. Radisic, Siou Teck Chew, Yongxi Qian and T. Itoh, "High-Efficiency Power Amplifier Integrated with Antenna," in *IEEE Microwave and Guided Wave Letters*, vol. 7, no. 2, pp. 39-41, Feb 1997.

[62] T. Le Nadan, J. P. Coupez and C. Person, "Optimization and Miniaturization of a Filter/antenna Multi-function Module Using a Composite Ceramic-Foam Substrate," in *Microwave Symposium Digest, 1999 IEEE MTT-S International*, 1999, pp. 219-222 vol.1.

[63] A. Abbaspour-Tamijani, J. Rizk and G. Rebeiz, "Integration of Filters and Microstrip Antennas," in *Antennas and Propagation Society International Symposium, 2002. IEEE*, 2002, pp. 874-877 vol.2.

[64] Wei-jun W., Ying-Zeng Y., Shao-li Z., Zhi-ya Z. and Jiao-Jiao X. “A New Compact FilterAntenna for modern Wireless Communication Systems”. *IEEE Antennas and Wireless Propagation Letters* vol.10, (2011). 1131-1134.

[65] Ghaith M., Michael J.L., Peter S.H., Peter G. and Ekaist N. “Design of Filtering Microstrip Antenna Using Filter Synthesis Approach.” *Prog Electromag Res Lett* 145, 59-67, (2014).

[66] C. X. Mao et al., “Integrated Filtering-Antenna with Controllable Frequency Bandwidth,” in *Proc. 9th Eur. Conf. Antennas Propag.*, 2015, pp. 1–4.

[67] Chao-Tang Chuang and Shyh-Jong Chung, "Synthesis and Design of a New Printed Filtering Antenna," *Antennas and Propagation, IEEE Transactions on*, vol. 59, pp. 1036-1042, 2011.

[68] Z. H. Jiang and D. H. Werner, "A Compact, Wideband Circularly Polarized Co-designed Filtering Antenna and Its Application for Wearable Devices With Low SAR," in *IEEE Transactions on Antennas and Propagation*, vol. 63, no. 9, pp. 3808-3818, Sept. 2015.

[69] Z. H. Jiang, M. D. Gregory, and D. H. Werner, “Design and Experimental Investigation of a Compact Circularly Polarized Integrated Filtering Antenna for Wearable Biotelemetric Devices,” *IEEE Trans. Biomed. Circuits Syst*., vol. 10, no. 2, pp. 328–338, Apr. 2016.

[70] J. H. Lee, N. Kidera, G. Dejean, S. Pinel, J. Laskar, and M. M. Tentzeris, “A V-band Front-End with 3-D Integrated Cavity Filters/Duplexers and Antenna in LTCC Technologies,” *IEEE Trans. Microw. Theory Tech*., vol. 54, no. 7, pp. 2925–2936, Jul. 2006.

[71] Zakaria, Z.; Sam, W.Y.; Aziz, M.Z.A.A.; Isa, A.A.M.; Johar, F.M., "Design of Integrated Rectangular SIW Filter and Microstrip Patch Antenna," *Applied Electromagnetics (APACE), 2012 IEEE Asia-Pacific Conference* on , vol., no., pp.137,141, 11-13 Dec. 2012.

[72] H. M. Hizan, I. C. Hunter, and A. I. Abunjaileh, “Integrated SIW Filter and Microstrip Antenna,” in Proc. *40th Eur. Microw. Conf.*, 2010, pp. 184–187.

[73] Nova O. A., Bohorquez J. C., Pena N. M., Bridges G. E., Shafai L., Shafai C., "Filter-Antenna Module Using Substrate Integrated Waveguide Cavities," Antennas and Wireless Propagation Letters, IEEE, vol.10, pp.59-62, 2011.

[74] Yusuf, Yazid, and Xun Gong. "Compact Low-Loss Integration of High-3-D Filters with Highly Efficient Antennas." *IEEE Transactions on Microwave Theory and Techniques* 59.4 (2011): 857-865.

[75] Y. Yusuf, H. T. Cheng, and X. Gong, “A Seamless Integration of 3-D Vertical Filters with Highly Efficient Slot Antennas,” IEEE Trans. Antennas Propag, vol. 59, no. 11, pp. 4016–4022, Nov. 2011.

[76] H. Cheng, Y. Yusuf, and Xun Gong. "Vertically Integrated Three-Pole Filter/Antennas for Array Applications." *IEEE Antennas and Wireless Propagation Letters* 10 (2011): 278-281.

[77] Yusuf, Yazid, Haitao Cheng, and Xun Gong. "Co-Designed Substrate-Integrated Waveguide Filters with Patch Antennas." *IET Microwaves, Antennas & Propagation* 7.7 (2013): 493-501.

[78] P. Y. Qin, Y. J. Guo, Y. Cai, E. Dutkiewicz, and C. H. Liang, “A Reconfigurable Antenna with Frequency and Polarization Agility,” *IEEE Antennas Wireless Propag. Lett*., vol. 10, pp. 1373–1376, 2011.

[79] MA46580 M/A-Com. Lowell, MA: M/A-COM/Tyco.

[80] M. Shirazi, T. Li and X. Gong, "Reconfigurable Double Slot-Ring Antenna for Bandwidth Enhancement," *2016 International Workshop on Antenna Technology (iWAT)*, Cocoa Beach, FL, 2016, pp. 15-17.

[81] DSM8100-000 Skyworks.Inc.

[82] A. Dorne and D. Lazazus, Very High Frequency Techiniques, New York: McGraw-Hill, pp. 171-180, 1947.

[83] An Introduction to HFSS: Fundamental Principles, Concepts, ANSYS, Inc, Canonsburg, PA, 2009

[84] N. Appannagarri, I. Bardi, R. Edlinger, J. Manges, M. Vogel, Z. Cendes, and J. Hadden. "Modeling Phased Array Antennas in Ansoft HFSS." *IEEE International Conference* on, pp. 323-326. IEEE, 2000.

[85] F. Yang and Y. Rahmat-Samii, "Reflection phase characterizations of the EBG Ground Plane for Low Profile Wire Antenna Applications," *IEEE Trans. Antennas Propag.*, vol. 51, no. 10, pp. 2691–2703, Oct. 2003.

[86] D. M. Pozar and D H. Schaubert, "Scan Blindness in Infinite Phase Arrays of Printed Dipoles," *IEEE Trans. Antenna and Propagat.*, vol. 32, no. 6, pp. 602-610, 1984.

[87] F. Yang and Y. Rahmat-Samii, "Step-Like Structure and EBG Structure to Improve the Performance of Patch Antennas on High Dielectric Substrate," in *Proc. IEEE AP-S Dig.*, vol. 2, July 2001, pp. 482–485.

[88] D. B. Hou, S. Xiao, B. Z. Wang, L. Jiang, J. Wang, and W. Hong, "Elimination of Scan Blindness with Compact Defected Ground Structures in Microstrip Phased Array," *IET Microw. Antenna Propagat.*, vol. 3, pp. 269-275, Mar. 2009.

[89] J. G. Yook and L. Katehi, "Micromachined Microstrip Patch Antenna with Controlled Mutual Coupling and Surface Waves" *IEEE Trans. Antenna and Propagat.*, vol. 49. pp. 1282-1289, 2001.

[90] Getting Started with HFSS: Floquet Ports, ANSYS, Inc, Canonsburg, PA, 2010.

[91] M. Manteghi, "Analytical Calculation of Impedance Matching for Probe-fed Microstrip Patch Antennas," *IEEE Trans. Antennas Propag.*, vol. 57, no. 12, pp. 3972–3975, Dec. 2009.

[92] J. Kovitz and Y. Rahmat-Samii, "Using Thick Substrates and Capacitive Compensation to Enhance the Bandwidth of Traditional CP Patch Antennas," *IEEE Trans. Antennas Propag.*, vol. 62, no. 10, pp. 4970–79, Oct 2014.

[93] T. Li, H. Cheng and X. Gong, "Integrated Single-fed Circularly-Polarized Patch Antennas with High-Q Cavity Filters," 2014 *IEEE Antennas and Propagation Society International Symposium (APSURSI),* Memphis, TN, 2014, pp. 1873-1874..

[94] Deslandes, D., Wu, K.: ‘Single-Substrate Integration Technique of Planar Circuits and Waveguide Filters’, *IEEE Trans. Microw. Theory Tech*., 2003, 51, (2), pp. 593–596.

[95] Haneishi, M., and S. Yoshida, "A Design Method of Circularly Polarized Rectangular Microstrip Antenna by One-Point Feed," in *Microstrip Amenua Design,* K. C. Gupta and A. Benalla (Eds.), Arrech House, Norwood, MA, 1988, pp. 313- 321..

[96] R. Garg, P. Bhartia, I. Bahl, and A. Ittipiboon, *Microstrip Antenna Design Handbook*. Norwood, MA: Artech House, 2001.

[97] G. L. Matthaei, L. Young and E. M. T. Jones, *Microwave Filters, Impedance-Matching Networks, and Coupling Structures.* Dedham, MA: Artech House Books, 1980.

[98] J. Huang, “A Technique for an Array to Generate Circular Polarization with Linearly Polarized Elements,” *IEEE Trans. Antennas Propag*., vol. AP-34, no. 9, pp. 1113–1124, Sep. 1986.

[99] H. Arslan, “Cognitive Radio, Software Defined Radio, and Adaptive Wireless Systems”. Berlin, Germany: Springer-Verlag, 2007..

[100] X. Gong, A. Margomenos, B. Liu, S. Hajela, L. P. B. Katehi and W. J. Chappell, “Precision Fabrication Techniques and Analysis on High-Q Evanescent-Mode Resonators and Filters of Different Geometries,” *IEEE Trans. Microwave Theory & Tech.*, vol. 52, no. 11, pp. 2557-2566, Nov. 2004.

[101] S. J. Park, I. Reines and G. Rebeiz, "High-Q RF-MEMS Tunable Evanescent-Mode Cavity Filter," *2009 IEEE MTT-S International Microwave Symposium Digest*, Boston, MA, 2009, pp. 1145-114.

[102] Application Note 1287-8: “Simplified Filter Tuning Using Time Domain,” Agilent Technologies Corp., 2001, Palo Alto,CA.